Quantal calculations on the rovibrational excitation of H(_2) and HD induced by H

Wrathmall, Steven .

Wrathmall, Steven . (2007) *Quantal calculations on the rovibrational excitation of H(_2) and HD induced by H*, Durham theses, Durham University. Available at Durham E-Theses Online: http://etheses.dur.ac.uk/2313/

Quantal calculations on the rovibrational excitation of H_2 and HD induced by H

Steven A. Wrathmall

A thesis submitted in partial fulfilment
of the requirements for the degree of
Doctor of Philosophy

Department of Physics
Durham University

November 11, 2007

Quantal calculations on the rovibrational excitation of H_2 and HD induced by H

Steven A. Wrathmall

Abstract

Cross sections have been computed for non-reactive rovibrational transitions of H_2 and HD, induced by collisions with H atoms, using the $H+H_2$ interaction potential calculated recently by Mielke *et al.* [39] and an earlier potential of Boothroyd *et al.* [38]. The calculations relate explicitly to non-reactive scattering, excluding the proton-exchange channels. Cross sections derived using a simple harmonic oscillator approximation to the vibrational motion are compared with results obtained using numerically 'exact' solutions of the rovibrational eigenvalue equation. The convergence of the cross sections with respect to the size of the rovibrational basis set is investigated. Convergence is found to be slow, owing to the strength of the collisional coupling between vibrational manifolds.

The cross sections are used to derive the rate coefficients for the rovibrational excitation of H_2 and HD by H. For vibrationally inelastic transitions, the new rate coefficients at $T \sim 1000$ K are larger than the results of earlier calculations in which the vibrational motion was treated approximately, by means of a simple harmonic oscillator model. As a result, much better agreement is obtained with the empirical estimates by Allers *et al.* [59] of the rate coefficients for vibrational relaxation of the levels $(\nu,\ j) = (1,\ 3)$ and $(2,\ 3)$ of H_2. However, the effects of the new data on the results of illustrative astrophysical models are less pronounced than the changes to the rate coefficients for vibrationally inelastic transitions might suggest.

Declaration

I confirm that no part of the material offered has previously been submitted by myself for a degree in this or any other University. Where material has been generated through joint work, the work of others has been indicated.

Steven A. Wrathmall
Durham, November 11, 2007

Dedicated to Dad, Katie, Gran and Granda,
for all their love, friendship, and support.

Acknowledgements

Firstly, I would like to thank Prof. David Flower for providing me the opportunity to work under his supervision. His support and understanding of problems in, and out of, the office has been crucial in the completion of my studies.
I would particularly like to thank Dr. Ifan Hughes for all his support, infectious enthusiasm, motivational chats, and trips to watch Swansea City AFC that have made my time at Durham so enjoyable.
I would also like to thank Dr. Simon Gardiner, Prof. Charles Adams, Dr. Robert Potvliege, Dr. Matt Jones, and Dr. Simon Cornish. I have taken advantage of their 'open door' policy many times and they have fuelled my interest and enthusiasm in many other areas of atomic and molecular physics.
I am indebted to those people who have helped prepare this thesis, especially Dr. Ifan Hughes, Dr. Paul Griffin, Dr. Kevin Weatherill, and Prof. David Flower.
I have enjoyed the company of many friends whilst being a member of the Atomic and Molecular Group in Durham. I'd especially like to thank Dr. Nick Parker and Dr. David Smith for making my first year in Durham so entertaining. I'd also like to thank Andrew Martin and Antoine Gusdorf for their friendship and support throughout my studies. Thanks also goes to the rest of the Durham Atomic and Molecular Physics Group and Durham University Physics Department for making my time here so enjoyable.
Special thanks goes to Prof. Jeremy Hutson, Prof. Jacques Le Bourlot, and Prof. Rob Leroy for assistance with computational programs used during my studies. I am most grateful for the data provided by Antoine Gusdorf, which was used in Figure 7.1, and for the data provided by Prof. David Flower, which was used in Figure 7.2.
I wish to thank the Particle Physics and Astronomy Research Council for their financial support throughout the course of my studies.
Finally, I would like to thank Dad, Katie, Gran and Granda, and all my family and friends for their never ending encouragement and support.

> *'There is nothing more practical than a good theory.'*
> James C. Maxwell

Contents

List of Figures

List of Tables

Part I

Introduction

Chapter 1

Introduction and Motivation

In this chapter the basic concepts of collision theory are introduced. The motivation for investigating collisions in the $H+H_2$ and H+HD atom–diatom systems is discussed, and the general research aims of this thesis are presented.

1.1 Atom–molecule collision theory

When investigating the properties of an atomic or molecular system some quantities of interest (e.g. the interaction potential of the system) cannot be measured directly. Rather, other quantities, such as cross sections or rate coefficients, are measured which can be used to derive indirectly the quantity of interest. Atom–molecule collision theory provides a framework relating these measured quantities (e.g. rate coefficients, cross sections, etc.) to various properties of the atomic and molecular system (e.g. interaction potential, bound energy levels, etc.).

The theoretical framework for atom–molecule collisions has been developed extensively over the past five decades. The growth in the field is closely linked to growth of computing technology. With the advent of larger and more powerful machines there exists more powerful techniques and routines for solving the Schrödinger equation. The complexity of the problem, and the accuracy of its solution, is often limited by the available computing power.

The calculations presented in this thesis consider atom–diatom collisions in which the interaction potential is already given. In this case the cross sections and rate coefficients are calculated, for the given interaction potential, with the goal of achieving the highest accuracy that is computationally practical.

1.1.1 Cross sections

The cross section, $\sigma_{j\rightarrow j'}$, for a process resulting in a system in state j undergoing a transition to state j' is defined as the transition probability per unit time, per unit target scatterer and per unit flux of the incident particles with respect to the target. Classically, the cross section is interpreted as an area centred on the target scatterer through which an incident particle must pass for the transition, $j \rightarrow j'$, to occur and is defined [1] by

$$\sigma_{j\rightarrow j'} = 2\pi \int_0^\infty P_{j\rightarrow j'}(b)\ b\ \mathrm{d}b\ , \tag{1.1}$$

where $P_{j\rightarrow j'}(b)$ is the transition probability for impact parameter b. Using atomic units the impact parameter is related to the angular momentum, l, through the relation

$$\begin{aligned} 2\mu E b^2 &= l(l+1) \\ &= k^2 b^2\ , \end{aligned} \tag{1.2}$$

where k is the wave number at collision energy E and μ is the reduced mass. Through differentiation of equation (1.2) and setting $\mathrm{d}l = 1$ in the quantal limit one obtains

$$b\ \mathrm{d}b = \frac{2l+1}{2k^2}\ , \tag{1.3}$$

which enables the quantum mechanical equivalent of equation (1.1) to be obtained as

$$\sigma_{j\rightarrow j'} = \frac{\pi}{k_j^2} \sum_l (2l+1) P_{j\rightarrow j'}(l)\ , \tag{1.4}$$

where k_j is the wave number in the initial channel. Assuming the state j is degenerate with ω_j degenerate sub–levels labelled by Ω then the transition probabilities are given by the relation

$$P_{j\rightarrow j'}(l) = \frac{1}{\omega_j} \sum_{\Omega,\Omega'} |T_{j'\Omega',j\Omega}(l)|^2\ , \tag{1.5}$$

where $T(l)$ is an element of the transition matrix $\mathbf{T}$. The transition matrix contains all the information on the scattering process [2]. It is related to the scattering matrix, $\mathbf{S}$, through

$$\mathbf{S} = \mathbf{1} - \mathbf{T}\,, \tag{1.6}$$

where $\mathbf{1}$ is the unit matrix. The scattering matrix is related to the reactance matrix $\mathbf{K}$ by

$$\mathbf{S} = (\mathbf{1} + \mathrm{i}\mathbf{K})(\mathbf{1} - \mathrm{i}\mathbf{K})^{-1}, \tag{1.7}$$

where i is $\sqrt{-1}$, and the elements of the reactance matrix are real. Often, the reactance matrix, $\mathbf{K}$, is calculated first, and the transition, $\mathbf{T}$, and scattering, $\mathbf{S}$, matrices are determined from it using the above relations [2]. The incident flux of the particles is conserved, therefore

$$\sum_{j'\Omega'} |S_{j'\Omega',j\Omega}|^2 = 1 \tag{1.8}$$

The $\mathbf{S}$ matrix is symmetric, due to time-reversal symmetry (micro reversibility), thus its elements are related by

$$S_{j'\Omega',j\Omega} = S_{j\Omega,j'\Omega'}, \tag{1.9}$$

which gives the relationship between cross sections for the scattering process, and its reverse process, as

$$\sigma_{j\rightarrow j'} k_j^2 \omega_j = \sigma_{j'\rightarrow j} k_{j'}^2 \omega_{j'}. \tag{1.10}$$

Note: The symmetry of $\mathbf{S}$ implies the symmetry of $\mathbf{T}$ and hence equation (1.1) is obtained through use of equations (1.4) and (1.5). However this is for the subset of problems where l is conserved.

Cross sections, in atomic and molecular physics, are typically given in units of 10^{-16} cm^2.

1.1.2 Rate coefficients

Rate coefficients are usually required to interpret experimental data or astronomical observations. The calculations presented in this thesis involved determining the thermally averaged (Maxwellian) rate coefficients, which are related to the cross sections through

$$\langle \sigma v \rangle_{j \to j'} = \left(\frac{8 k_{\mathrm{B}} T}{\pi \mu} \right)^{\frac{1}{2}} \int_{0}^{\infty} x_j \sigma(x_j) \mathrm{e}^{-x_j} \mathrm{d}x_j, \tag{1.11}$$

where $x_j = \mu v_j^2 / 2 k_{\mathrm{B}} T$, v_j is the relative collision speed, k_{B} is Boltzmann's constant, and $(8 k_{\mathrm{B}} T / \pi \mu)^{1/2}$ is the mean thermal speed at kinetic temperature T.

Rate coefficients are typically given in units of $\mathrm{cm}^3\ \mathrm{s}^{-1}$.

1.2 Molecules in space

Over the past 70 years it has been determined that the interstellar gas contains a variety of molecules [3]. Although originally thought to contain a gas predominantly made only of hydrogen atoms and ions, a variety of molecular species from simple diatomics to complex organic species have now been observed. The molecules tend to be found in dense extended regions and also in highly dense star forming regions [4]. Understanding molecular processes not only provides information about the the evolution of these regions, but also provides a way of determining the composition and various physical properties of the gas (e.g. kinetic temperature, atomic and molecular abundances, densities, etc.).

1.2.1 The importance of Hydrogen

Molecular hydrogen, H_2 , is the most abundant molecule in the universe and is the most abundant molecule present in interstellar molecular gas clouds [3]. Electronic, rotational, and rovibrational transitions have been observed for H_2 in the interstellar medium [5–8] through use of a wide range of observing techniques (as these transitions occur over a wide range of wavelengths). As a consequence of its high elemental abundance atomic hydrogen can also be the most abundant atomic species in interstellar molecular gas clouds.

In some regions, atomic and molecular hydrogen have comparable number densities. In these regions there are several astronomical contexts in which inelastic collisions involving H_2 molecules and H atoms are crucial to the thermal balance of the medium:

- In the primordial gas, subsequent to the recombination of H^+ with electrons at redshift $z \sim 1000$, the most abundant species was H, followed by He; but there were trace amounts (fractional abundance $\sim 10^{-6}$) of H_2 [9]. Rovibrationally inelastic scattering of H on H_2 and on its singly–deuterated form, HD, provided the cooling essential to the gravitational collapse of inhomogeneities in the primordial gas and the formation of the first stars.
- In the Galactic interstellar medium, shock heating of molecular gas can lead to partial dissociation of H_2, in which case $H+H_2$ collisions determine the thermal profile and chemical evolution of the post-shock gas as it cools to its equilibrium state.
- In photon–dominated regions of the interstellar medium, which are exposed to sources of ultraviolet radiation, there exists a region of overlap of atomic and molecular hydrogen, where the optical depth in the ultraviolet electronic absorption bands of H_2 becomes sufficient to shield the H_2 deeper in the cloud from the dissociating radiation ('self–shielding'). The kinetic temperature in this region is controlled by inelastic $H+H_2$ collisions.

For observations, and computational simulations, of these regions to be interpreted accurately there must be accurate rate coefficients available for the $H+H_2$ and H+HD systems.

$H+H_2$ and H+HD are ostensibly the simplest atom–molecule systems, involving only three singly charged nuclei and three electrons. Accordingly, it might be anticipated that the cross-sections for rotational and rovibrational excitation of H_2 and HD by H would be well established. However, this is not the case: the $H+H_2$ interaction comprises a very shallow van der Waals potential well ($\sim$ 20 K), where the atom–molecule interaction is only weakly anisotropic. Because the region of the van der Waals minimum is crucial in calculations of rotational excitation cross-sections at low collision energies, such calculations impose stringent requirements on the accuracy to which the absolute H+H_2 interaction energy must be calculated. Furthermore, as the collision energy increases, approaching values comparable to the barrier to proton exchange ($\sim$ 5000 K), reactive scattering can occur. At such energies, the H+H_2 interaction gives rise to strong collisional coupling between the vibrational manifolds of the molecule. As a consequence:

1. The rovibrational cross-sections converge slowly with the size of the set of rovibrational states.
2. More care than usual must be taken with the representation of the rovibrational wave functions of the molecule.

In spite of the difficulties outlined above, the H+H_2 system offers a unique opportunity to perform essentially exact calculations of rovibrational cross-sections. Owing to the low mass of H_2 , and hence its large rotational constant, there are only 318 bound rovibrational levels, with the largest value of the rotational quantum number, j, being $j = 29$. Consequently, quantum mechanical calculations using the exact coupled–channels method, with a complete or near–complete basis of bound rovibrational states, might be envisaged. The H+HD system contains 399 rovibrational energy levels with the largest value of the rotational quantum number, j, being $j = 35$.

Unlike H_2 , HD has a small but finite permanent dipole moment. It follows that radiative transitions with $\Delta j = 1$ are permitted in HD, whereas the (electric quadrupole) selection rule in H_2 is $\Delta j = 2$. Similarly, in collisions with H, transitions of HD involving odd values of j can occur, even in the case of non–reactive scattering, when there is no exchange of protons. On the other hand, during non-reactive scattering of H on H_2 , only those transitions with even values of j are permitted, thus preserving ortho–H_2 (j odd) and para–H_2 (j even) as distinct species.

1.3 Previous studies of collisions in H+H_2 and H+HD

The rotational and rovibrational excitation of H_2 resulting from collisions with H has been the subject of many previous quantum mechanical studies

[10–18].

The rotational and rovibrational excitation of HD resulting from collisions by H has been the subject of the following previous quantum mechanical studies [19, 20].

1.4 Research aims

The aims for the work presented in this thesis were as follows:

1. To calculate cross sections, as a function of collision energy, and thermally–averaged rate coefficients, as a function of kinetic temperature, for the H+H_2 and H+HD atom–diatom systems, using the most accurate input data and methods available, and compare with those obtained from previous calculations.
2. To apply the newly calculated rate coefficients to astrophysical problems, relevant to the H+H_2 and H+HD systems, and compare the output to that obtained from using rate coefficients calculated previously.

1.5 Thesis outline

This rest of this thesis is structured as follows:

- **Part 2: Theory** – The background theory and calculation methods are discussed. Chapter 2 presents the coupled–channel theory of atom–diatom scattering and the theoretical concepts used to determine the cross sections and thermally averaged rate coefficients. In Chapter 3 the interaction potentials available for H+H_2 are analysed, and the potentials most appropriate for our calculations are discussed. In Chapter 4 the computational methods used in the scattering calculation are presented. The methods used to test their validity are also discussed.

- **Part 3: Results** – The cross sections and rate coefficients calculated for the H+H_2 and H+HD systems are presented in Chapter 5 and Chapter 6, respectively. Several applications of the results, including those of an astrophysical context, and their implications are discussed in Chapter 7.
- **Part 4: Conclusions and Future Work** – The conclusions drawn from performing the scattering calculations, and their application, are discussed in Chapter 8. Possible improvements and further work on the scattering calculations and their applications is presented in Chapter 9.
- **Part 5: Appendices** – contains the appendices and other supporting material.

1.6 Published work

The work in this thesis has been partially covered in the following publications:

- *A quantum-mechanical study of rotational transitions in H_2 induced by H*
  Wrathmall S A and Flower D R 2006 *J. Phys. B: At. Mol. Opt. Phys.* **39** L249
- *The rovibrational excitation of H_2 induced by H*
  Wrathmall S A and Flower D R 2007 *J. Phys. B: At. Mol. Opt. Phys.* **40** 3221
- *The excitation of molecular hydrogen by atomic hydrogen in astrophysical media*
  Wrathmall SA, Gusdorf A and Flower DR 2007 Accepted for publication in *MNRAS*.

Part II

Theory

Chapter 2

Scattering Theory for Atom–Diatom Collisions

This chapter presents an overview of the theory of non-reactive atom-diatom scattering. The theoretical framework, for atom–diatom collisions, has been developed extensively over the past five decades. The theoretical methods have been presented many times and comprehensive sources include [1], [21] and [22]. The overview given here follows the presentation of Flower [21] in which the Born–Oppenheimer approximation is introduced first followed by the theory of rotational excitation in atom–diatom collisions, the theory of rovibrational excitation in atom–diatom collisions, the solution of the resulting coupled–channel equations, and the determination of the thermally–averaged rate coefficients.

2.1 The Born–Oppenheimer Approximation

Consider the collision between a one electron atom, A, and a fully stripped ion, B. We consider this system for illustrative purposes; the conclusions drawn can be generalised for collisions between atoms and molecules. Atomic units are adopted, in which $e = m_\mathrm{e} = \hbar = 1$, throughout this and the following discussions.

When studying the collisions we are interested in the relative motion of the particles and not in the motion of the centre of mass (*barycentre*) of the system. The velocity of the centre of the mass remains constant and is, therefore, irrelevant to the scattering processes.

We denote the position of the centre of mass relative to a space–fixed or laboratory reference frame as $\mathbf{R}_\mathrm{C}$, the coordinates of atom A and ion B as $\mathbf{R}_\mathrm{A}$ and $\mathbf{R}_\mathrm{B}$, respectively, and $\mathbf{R}$ is a vector connecting the centre of mass of A to B in the direction of A to B (see figure 2.1). We have defined the position of the centre of mass such that

$$\begin{aligned} \mathbf{R} &= \mathbf{R}_\mathrm{AC} + \mathbf{R}_\mathrm{CB} \\ &= \frac{m_\mathrm{B}}{m_\mathrm{A}+m_\mathrm{B}}\mathbf{R} + \frac{m_\mathrm{A}}{m_\mathrm{A}+m_\mathrm{B}}\mathbf{R} \,, \end{aligned} \tag{2.1}$$

where the momentum of the system given by

$$\begin{aligned} m_\mathrm{A}\dot{\mathbf{R}}_\mathrm{A} + m_\mathrm{B}\dot{\mathbf{R}}_\mathrm{B} &= m_\mathrm{A}(\dot{\mathbf{R}}_\mathrm{C} - \dot{\mathbf{R}}_\mathrm{AC}) + m_\mathrm{B}(\dot{\mathbf{R}}_\mathrm{C} + \dot{\mathbf{R}}_\mathrm{CB}) \\ &= (m_\mathrm{A} + m_\mathrm{B})\dot{\mathbf{R}}_\mathrm{C} \,, \end{aligned} \tag{2.2}$$

with use of equation (2.1). Therefore the momentum of the system is due to the total mass, located at the centre of mass $\mathbf{R}_\mathrm{C}$.

The kinetic energy of the system is given by

$$\begin{aligned} \frac{1}{2}m_\mathrm{A}\dot{\mathbf{R}}_\mathrm{A}^2 + \frac{1}{2}m_\mathrm{B}\dot{\mathbf{R}}_\mathrm{B}^2 &= \frac{1}{2}m_\mathrm{A}(\dot{\mathbf{R}}_\mathrm{C} - \dot{\mathbf{R}}_\mathrm{AC})^2 + \frac{1}{2}m_\mathrm{B}(\dot{\mathbf{R}}_\mathrm{C} + \dot{\mathbf{R}}_\mathrm{CB})^2 \\ &= \frac{1}{2}(m_\mathrm{A} + m_\mathrm{B})\dot{\mathbf{R}}_\mathrm{C}^2 + \frac{1}{2}\mu\dot{\mathbf{R}}^2 \,, \end{aligned} \tag{2.3}$$

where $\mu = m_\mathrm{A}m_\mathrm{B}/(m_\mathrm{A}+m_\mathrm{B})$ is the *reduced mass* of the system. Therefore the kinetic energy consists of two components:

1. The first component is due to the kinetic energy of the total mass moving with the velocity of the centre of mass.

2. The second component is due to the reduced mass moving with the relative velocity, $\dot{\mathbf{R}}$, of A and B.

Assuming the system is isolated, the velocity of the centre of mass is constant and therefore may be removed by an appropriate change of inertial frame. We are left with the kinetic energy due to the relative motion of A and B, which may be used to excite internal degrees of freedom system. Thus we may consider the atom, A, to move with with mass, μ, relative to a fixed centre of force, B.

The Hamiltonian of system AB may be written as

$$H(\mathbf{x},\mathbf{R}) = H_{\mathrm{A}}(\mathbf{x},\mathbf{R}) - \frac{\nabla_R^2}{2\mu} + V(\mathbf{x},\mathbf{R}) \ , \tag{2.4}$$

where $\mathbf{x}$ is the position vector, with respect to the centre of mass of A and B, of the electron, $H_{\mathrm{A}}(\mathbf{x},\mathbf{R})$ represents the electronic Hamiltonian of the atom A, $V(\mathbf{x},\mathbf{R})$ represents the interaction potential between A and B, and $-\nabla_R^2/(2\mu)$ is the relative kinetic energy operator. In collision problems we aim to solve the eigenvalue equation

$$H\Psi = E\Psi \ , \tag{2.5}$$

where E is the total barycentric energy of the colliding system, which is the relative kinetic energy of A and B at infinite separation.

The wave function is of the form $\Psi = \Psi(\mathbf{x},\mathbf{R})$. We now write the wave function in the following form, which retains generality but hints at the separation of the relative coordinates, $\mathbf{R}$, and the electronic coordinates, $\mathbf{x}$:

$$\Psi(\mathbf{x},\mathbf{R}) = \sum_i F_i(\mathbf{R})\phi_i(\mathbf{x},\mathbf{R}) \ . \tag{2.6}$$

At fixed R (where $R = |\mathbf{R}|$), equation (2.6) is an expansion of the wave function in terms of the solutions of the wave equation

$$[H_{\mathrm{A}}(\mathbf{x},\mathbf{R}) + V(\mathbf{x},\mathbf{R})]\phi_i(\mathbf{x},\mathbf{R}) = E_i(\mathbf{R})\phi_i(\mathbf{x},\mathbf{R}) \ , \tag{2.7}$$

which form an orthonormal set of functions, such that

$$\langle\phi_j|\phi_i\rangle = \int \phi_j^*(\mathbf{x},\mathbf{R})\phi_i(\mathbf{x},\mathbf{R})\mathrm{d}\mathbf{x} = \delta_{ij} \ . \tag{2.8}$$

Substituting equation (2.6) in the eigenvalue equation (2.5) and projecting out ϕ_j by operating with $\int \mathrm{d}\mathbf{x} \ \phi_j^*(\mathbf{x},\mathbf{R})$ on both sides of the equation, we obtain

$$\begin{aligned}&\left[-\frac{\nabla_R^2}{2\mu} + E_j(\mathbf{R}) - E\right] F_j(\mathbf{R}) \\ &= \sum_i \left[\frac{\langle\phi_j|\nabla_{\mathbf{R}}|\phi_i\rangle\cdot\nabla_{\mathbf{R}}F_i(\mathbf{R})}{\mu} + \frac{\langle\phi_j|\ \nabla_R^2\ |\phi_i\rangle F_i(\mathbf{R})}{2\mu}\right] \ .\end{aligned} \tag{2.9}$$

The terms on the right hand side of equation (2.9) are due to coupling between the electronic and relative motions. Were it not for their presence we would have succeeded in separating the eigenvalue equation into:

- Equation (2.7) for the electronic motion at a given value for $\mathbf{R}$, and
- Equation (2.9) for the relative motion on a given *electronic potential energy surface*, $E_j(\mathbf{R})$.

The Born–Oppenheimer approximation, also know as the 'adiabatic' approximation, consists of neglecting the terms on the right hand side of equation (2.9). These terms give rise to transitions between potential energy surfaces. For the purpose of this discussion, the rovibrational excitation in atom–diatom collisions, the collisions are assumed to take place along a single adiabatic potential energy surface.

2.2 The scattering of an atom by a rigid rotor

Following the analysis of Flower [21] we first consider the scattering of an atom by a rigid rotor. We consider both space–fixed and body-fixed reference frames analyses for the collisions and develop the scattering formalism for both cases.

The theory for atom–diatom scattering is presented for the space–fixed frame (SF) and body–fixed (BF) frame for several reasons:

- The framework for either representation is equivalent. Identical cross sections are obtained using either coordinate system.
- Some problems are more suited to one representation. This is often due to the behaviour of the interaction potential under consideration.
- The computational programs used to calculate the cross sections use one, or both, of the coordinate systems.

Figure 2.2 illustrates the relationship between the coordinate systems. In the space–fixed coordinate system the polar coordinates of the atom are defined by a coordinate system whose origin is at the centre of the mass M of the rotor BC and is fixed in space. Two further angles define the orientation of BC in the same coordinate frame.

In the body–fixed coordinate system the polar angles of BC are defined relative to a coordinate system whose Z–axis coincides with MA and rotates in space through the course of the collision. This reference frame offers a more natural way of expressing the interaction potential, which depends on R and θ' only. However, as BC is rotating in a coordinate system which is also rotating, we have to consider the effects of Coriolis forces and centrifugal forces when using the body–fixed system.

The orientation of the body–fixed (BF) Z-axis relative to the space–fixed frame (SF), xyz, is denoted by (Θ, Φ). More comprehensive details of each system are given in the discussion below.

2.2.1 The space-fixed frame method

The scattering of a structureless particle by a rigid rotor was first considered in a quantum mechanical context by Arthurs and Dalgarno [23]. They considered a collision between a particle without internal structure (or whose internal structure may be neglected) and a two-particle system possessing internal angular momentum. The system is treated in the 'space–fixed' (SF) sense; in that the degrees of freedom of such a system are defined by the three polar coordinates of the atom, A, in a coordinate system whose origin is at the centre of mass, M, of the rotor, BC, and which is fixed in space along with two further angles defining the orientation of BC in this same coordinate frame. In this system the atom moves with reduced mass $\mu = m_{\mathrm{A}}(m_{\mathrm{B}} + m_{\mathrm{C}})/(m_{\mathrm{A}} + m_{\mathrm{B}} + m_{\mathrm{C}})$ relative to the centre of mass of BC.

We denote the polar coordinates of the atom A in the SF frame as (R, Θ, Φ).The polar angles of the rotor, BC, relative to the SF frame are given by (θ, ϕ).

We begin calculations by expressing the wave function of the rotor in terms of a complete orthonormal set of functions of the polar angles (θ, ϕ). The normalized spherical harmonics, Y, form such a set. We denote the angular

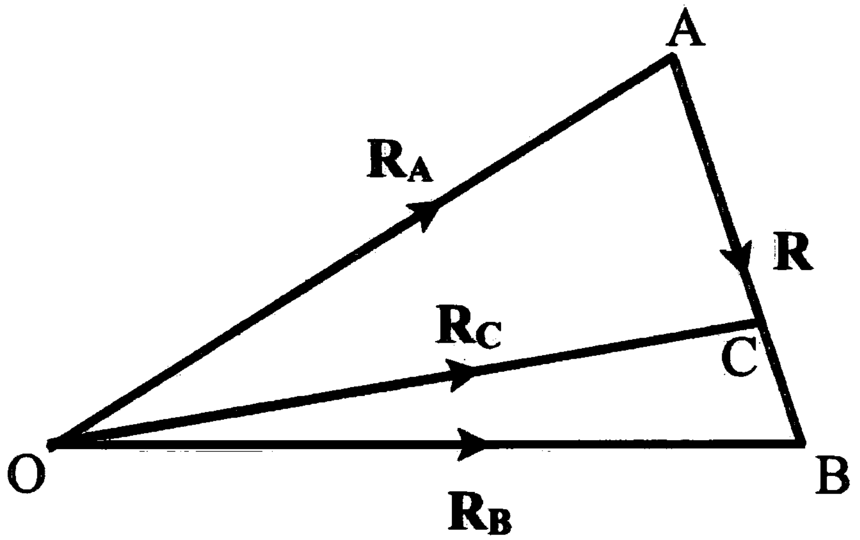

Figure 2.1: In this figure the space-fixed coordinate system of atom, A, the fully stripped atom, B, and their centre of mass, C, are defined.

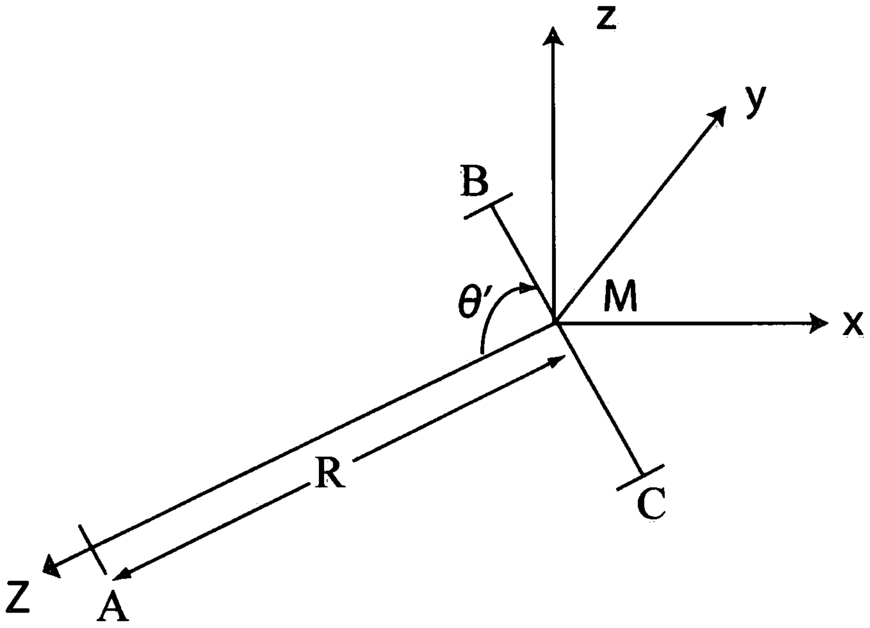

Figure 2.2: The space–fixed coordinate system *xyz* and the body–fixed *Z*-axis for the collision between an atom A and a rigid rotor BC, whose centre of mass is M. The coordinates R and θ' are known as 'Jacobi coordinates'. [21]

momentum quantum number of the rotor by j and its projection on the SF z-axis by m, therefore

$$Y_{jm}(\theta,\phi) = (-1)^m \left[\frac{(2j+1)(l-m)!}{4\pi(l+m)!}\right]^{\frac{1}{2}} P_j^m(\cos\theta)\mathrm{e}^{\mathrm{i}m\phi}, \quad (m \geq 0) \ , \tag{2.10}$$

with

$$Y_{j,-m}(\theta,\phi) = (-1)^m Y_{jm}^*(\theta,\phi) \ , \tag{2.11}$$

where $P_j^m(\cos\theta)$ is an associated Legendre polynomial [26].

The functions in equation (2.10) are eigenfunctions of $\mathbf{j}^2$ and j_z, with eigenvalues $j(j+1)$ and m respectively, with $\hat{j}$ as the angular momentum operator.

The total angular momentum of the system is composed of the angular momentum of the rotor, $\mathbf{j}$, and the angular momentum of the atom relative to the rotor, $\mathbf{l}$:

$$\begin{aligned} \mathbf{J} &= \mathbf{j} + \mathbf{l} \ , \\ J_z &= j_z + l_z \ . \end{aligned}$$

The total angular momentum is conserved during the collision.

The eigenfunctions of $\mathbf{j}^2$ and j_z are given by $Y_{jm}(\theta,\phi)$. The corresponding eigenfunctions for $\mathbf{l}^2$ and l_z are given by $Y_{lm_l}(\Theta,\Phi)$, with eigenvalues of $l(l+1)$ and m_l, respectively. The product of $Y_{jm}(\theta,\phi)$ and $Y_{lm_l}(\Theta,\Phi)$ is an eigenfunction of $\mathbf{j}^2$, j_z, $\mathbf{l}^2$ and l_z, but it is *not* an eigenfunction of the total angular momentum operators $\mathbf{J}^2$ or J_z. Eigenfunctions for $\mathbf{J}^2$ and J_z are formed by

$$\mathcal{Y}_{jlJM}(\theta,\phi;\Theta,\Phi) = \sum_{mm_l} C^{jlJ}_{mm_lM} Y_{jm}(\theta,\phi) Y_{lm_l}(\Theta,\Phi) \ , \tag{2.12}$$

where $M = m + m_l$ and $C^{jlJ}_{mm_lM}$ is a *Clebsch–Gordan coefficient* [27–29].

The Clebsch–Gordan coefficients are related to the Wigner $3j$–symbols through the following relation [27],

$$C^{jlJ}_{mm_lM} = (-1)^{j-l+M}(2J+1)^{\frac{1}{2}} \begin{pmatrix} j & l & J \\ m & m_l & -M \end{pmatrix} . \tag{2.13}$$

The parity of the eigenfunctions of the system A+BC is conserved during the collision. The symmetry operation associated with this conservation property is the inversion of the coordinates of all particles (A, B and C) about the origin of the SF coordinate frame:

$$\begin{aligned} &\theta \rightarrow \pi - \theta, \phi \rightarrow \pi + \phi, \\ &\Theta \rightarrow \pi - \Theta, \Phi \rightarrow \pi + \Phi \,. \end{aligned} \tag{2.14}$$

The operator that corresponds to this transformation of angles is P. Operating on the eigenfunctions (2.12) of $\mathbf{J}^2$ and J_z with P we find

$$\begin{aligned} P\mathcal{Y}_{jlJM}(\theta,\phi;\Theta,\Phi) &= \mathcal{Y}_{jlJM}(\pi-\theta,\pi+\phi;\pi-\Theta,\pi+\Phi) \\ &= (-1)^{j+l}\mathcal{Y}_{jlJM}(\theta,\phi;\Theta,\Phi) \,, \end{aligned} \tag{2.15}$$

where we have made use of the properties of the spherical harmonics in equation (2.10). Therefore $\mathcal{Y}_{jlJM}$ is an eigenfunction of $\mathbf{J}^2$ and J_z, with eigenvalues $J(J+1)$ and M, respectively, and also for the inversion operator, P, with eigenvalue $(-1)^{j+l}$. The eigenvalues of P are equivalent to the *parity*, p, of the wave function with values $p = \pm 1$. From now on the space-fixed eigenfunctions $\mathcal{Y}_{jlJM}(\theta,\phi;\Theta,\Phi)$ are denoted by $\mathcal{Y}_{jlpJM}(\theta,\phi;\Theta,\Phi)$.

The functions $\mathcal{Y}_{jlpJM}(\theta,\phi;\Theta,\Phi)$ are used as a basis in which to expand the total wave function, Ψ, as

$$\Psi(\hat{\mathbf{r}},\mathbf{R}) = \sum_{jlpJM} \frac{F^{j'l'}(jlpJM|R)}{R}\mathcal{Y}_{jlpJM}(\hat{\mathbf{r}};\hat{\mathbf{R}}) \,, \tag{2.16}$$

where $\hat{\mathbf{r}} = (\theta,\phi)$, $\hat{\mathbf{R}} = (\Theta,\Phi)$ and $\mathbf{R} = (R,\Theta,\Phi)$ are polar coordinates, and $F^{j'l'}(jlpJM|R)$ are the radial channel wave functions. The primed quantum numbers are those corresponding to the final scattering state. For example, a pure rotational transition is denoted by $j \rightarrow j'$.

We may write the eigenvalue equation (2.5) as

$$(H - E)\Psi = 0 \,, \tag{2.17}$$

where the Hamiltonian, H, (after separation of center of mass motion) is given by

$$H = \frac{\mathbf{j}^2}{2I} - \frac{\nabla_R^2}{2\mu} + V(R,\theta') \,. \tag{2.18}$$

The first term, in equation (2.18), corresponds to the rotational energy of relative motion of atom A and rotor BC. We may separate it into radial and angular parts:

$$-\frac{1}{2\mu}\nabla_R^2 = -\frac{1}{2\mu R}\frac{\partial^2}{\partial R^2}R + \frac{\mathbf{l}^2}{2\mu R^2} \ . \tag{2.19}$$

where μ is the reduced mass of system A+BC. The third term $V(R,\theta')$ represents the interaction potential between atom A and the rotor BC on a given potential energy surface (written above as $E_j(\mathbf{R})$ in equation (2.9)). The energy of the interaction potential is most naturally expressed in the BF frame coordinates R and θ'. The interaction potential is independent of ϕ' as the potential is invariant under rotations of the internuclear axis BC about the BF Z-axis.

Therefore, we may rewrite equation (2.18) as

$$\left[\frac{\mathbf{j}^2}{2I} - \frac{1}{2\mu R}\frac{\partial^2}{\partial R^2}R + \frac{\mathbf{l}^2}{2\mu R^2} + V(R,\theta') - E\right]\Psi = 0 \ , \tag{2.20}$$

where Ψ given by equation (2.16).

Using the eigenvalue equation for $\mathcal{Y}_{jlpJM}$

$$\mathbf{j}^2\mathcal{Y}_{jlpJM} = j(j+1)\mathcal{Y}_{jlpJM} \ ,$$

equation (2.20) may be rewritten as

$$\left[-\frac{1}{R}\frac{\partial^2}{\partial R^2}R + \frac{\mathbf{l}^2}{R^2} + 2\mu V(R,\theta') - k_j^2\right]\Psi = 0 \ , \tag{2.21}$$

where we have defined

$$\begin{aligned} k_j^2 &= 2\mu\left[E - E_{j\ \mathrm{rot.}}\right] \\ &= 2\mu\left[E - Bj(j+1)\right] \ , \end{aligned} \tag{2.22}$$

where $B = 1/(2I)$ is the rotational constant of the molecule BC, and $E_{j\ \mathrm{rot.}}$ is the rotational energy of the molecule BC with rotational angular momentum j.

The basis functions $\mathcal{Y}_{jlpJM}$ have the following orthonormality properties:

$$\int \mathcal{Y}^*_{jlpJM}(\hat{\mathbf{r}};\hat{\mathbf{R}})\mathcal{Y}_{j''l''p''J''M''}(\hat{\mathbf{r}};\hat{\mathbf{R}})d\hat{\mathbf{r}}\,d\hat{\mathbf{R}} = \delta_{jj''}\delta_{ll''}\delta_{pp''}\delta_{JJ''}\delta_{MM''} \ .$$

The double–prime ($''$) notation is used for dummy variables. It does not represent any further transitions.

Operating on equation (2.21) from the left with

$$\int \mathrm{d}\hat{\mathbf{r}}\ \mathrm{d}\hat{\mathbf{R}}\ \mathcal{Y}^*_{jlpJM}(\hat{\mathbf{r}};\hat{\mathbf{R}}) \ ,$$

and using equation (2.16) for the wave function, Ψ, equation (2.21) reduces to

$$\begin{aligned}&\left[\frac{\mathrm{d}^2}{\mathrm{d}R^2} - \frac{l(l+1)}{R^2} + k_j^2\right] F^{j'l'}(jlpJM|R) \\ &= 2\mu \sum_{j''l''p''J''M''} \langle jlpJM|V(R,\theta')|j''l''p''J''M''\rangle \\ &\qquad \times F^{j'l'}(j''l''p''J''M''|R) \ ,\end{aligned} \tag{2.23}$$

where we have made use of

$$\mathbf{l}^2\mathcal{Y}_{jlpJM} = l(l+1)\mathcal{Y}_{jlpJM} \ ,$$

which gives rise to the centrifugal term, $l(l+1)/R^2$. The more compact bra–ket notation has been used in writing the right hand side of equation (2.23).

Equations (2.23) are the *coupled–channel equations* for the SF frame coordinate system.

The matrix elements of the potential in equation (2.23) are given by

$$\begin{aligned}&\langle jlpJM|V(R,\theta')|j''l''p''J''M''\rangle \\ &= \int \mathcal{Y}^*_{jlpJM}(\hat{\mathbf{r}};\hat{\mathbf{R}})V(R,\theta')\mathcal{Y}_{j''l''p''J''M''}(\hat{\mathbf{r}};\hat{\mathbf{R}})\mathrm{d}\hat{\mathbf{r}}\ \mathrm{d}\hat{\mathbf{R}} \ .\end{aligned} \tag{2.24}$$

The interaction potential, $V(R,\theta')$, is expanded in a complete set of functions of the angular variable, θ',

$$V(R,\theta') = \sum_{\lambda=0}^{\infty} v_\lambda(R)P_\lambda(\cos\theta') \ , \tag{2.25}$$

where P_λ is a Legendre polynomial [26].

The matrix elements of the potential can now be rewritten as,

$$\begin{aligned}&\langle jlpJM|V(R,\theta')|j''l''p''J''M''\rangle \\ &= \sum_\lambda v_\lambda(R) \int \mathcal{Y}^*_{jlpJM}(\hat{\mathbf{r}};\hat{\mathbf{R}})P_\lambda(\cos\theta')\mathcal{Y}_{j''l''p''J''M''}(\hat{\mathbf{r}};\hat{\mathbf{R}})\mathrm{d}\hat{\mathbf{r}}\ \mathrm{d}\hat{\mathbf{R}} \ .\end{aligned} \tag{2.26}$$

To evaluate the integral we make use of the spherical harmonic addition theorem [27],

$$P_\lambda(\cos\theta') = \frac{4\pi}{2\lambda+1}\sum_{\nu=-\lambda}^{\lambda} Y_{\lambda\nu}(\hat{\mathbf{r}})Y^*_{\lambda\nu}(\hat{\mathbf{R}}) \ , \tag{2.27}$$

where $Y_{\lambda\nu}$ is a spherical harmonic. The theorem is used to transform the dependence of the potential from the BF coordinates, θ', to the SF angles $\hat{\mathbf{r}} = (\theta, \phi)$ and $\hat{\mathbf{R}} = (\Theta, \Phi)$. This allows the integrals in equation (2.26) to be evaluated.

With use of the SF basis functions in equation (2.12), and the composition relations for spherical harmonics [27] we obtain

$$\int Y^*_{jm}(\hat{\mathbf{r}})Y_{\lambda\nu}(\hat{\mathbf{r}})Y_{j''m''}(\hat{\mathbf{r}})\mathrm{d}\hat{\mathbf{r}} = \left[\frac{(2j''+1)(2\lambda+1)}{4\pi(2j+1)}\right]^{\frac{1}{2}} C^{j''\lambda j}_{m''\nu m}C^{j''\lambda j}_{000} \ , \tag{2.28}$$

and

$$\int Y^*_{lm_l}(\hat{\mathbf{R}})Y^*_{\lambda\nu}(\hat{\mathbf{R}})Y_{l''m_{l''}}(\hat{\mathbf{R}})\mathrm{d}\hat{\mathbf{R}} = (-1)^\nu\left[\frac{(2l+1)(2\lambda+1)}{4\pi(2l''+1)}\right]^{\frac{1}{2}} C^{l\lambda l''}_{m_l-\nu m_{l''}}C^{l\lambda l''}_{000} \ . \tag{2.29}$$

Thus, the matrix elements in equation (2.26) are given by

$$\begin{aligned}&\langle jlpJM|V(R,\theta')|j''l''p''J''M''\rangle\\ &= \sum_{\lambda\nu} v_\lambda(R)\left[\frac{(2j''+1)(2l+1)}{(2j+1)(2l''+1)}\right]^{\frac{1}{2}} C^{j''\lambda j}_{000}C^{l\lambda l''}_{000}\\ &\times \sum_{mm_lm''m_{l''}} C^{jlJ}_{mm_lM}C^{j''\lambda j}_{m''\nu m}C^{j''l''J''}_{m''m_{l''}M''}C^{l\lambda l''}_{m_l\nu m_{l''}} \ .\end{aligned} \tag{2.30}$$

Equation (2.30) may be expressed in terms of a Racah coefficient, W, through use of angular momentum recoupling theory [30]

$$\begin{aligned}&\langle jlpJM|V(R,\theta')|j''l''p''J''M''\rangle\\ &= \delta_{JJ''}\delta_{MM''}(-1)^{j+j''-J}\sum_\lambda v_\lambda(R)\frac{[(2j+1)(2l+1)(2j''+1)(2l''+1)]^{\frac{1}{2}}}{(2\lambda+1)}\\ &\times C^{jj''\lambda}_{000}C^{ll''\lambda}_{000}W(jlj''l'';J\lambda) \ .\end{aligned} \tag{2.31}$$

The Racah coefficient, W, is related to the $6j$–symbol by

$$W(jlj''l'';J\lambda) = (-1)^{j+l+j''+l''}\begin{Bmatrix} j & l & J \\ l'' & j'' & \lambda \end{Bmatrix} \ . \tag{2.32}$$

Conservation of the total angular momentum, J, and its projection M, on the SF z-axis is ensured by the presence of the Kronecker δ symbols in equation (2.31).

The Clebsch–Gordan coefficients, $C_{000}^{jj''\lambda}$ and $C_{000}^{ll''\lambda}$, vanish unless $j+j''+\lambda$ and $l+l''+\lambda$, respectively, are even. Hence

$$(-1)^{j+j''+\lambda+l+l''+\lambda} = +1 = (-1)^{j+l+j''+l''} , \tag{2.33}$$

as λ is an integer. Therefore

$$p = (-1)^{j+l} = (-1)^{j''+l''} = p'' , \tag{2.34}$$

and we confirm the parity is conserved. We may rewrite equation (2.31) in a more compact form

$$\langle jlpJM|V(R,\theta')|j''l''pJM\rangle = \sum_{\lambda} v_\lambda(R) f_\lambda(jl,j''l'';J) , \tag{2.35}$$

where

$$\begin{aligned} f_\lambda(jl,j''l'';J) = (-1)^{j+j''-J}&\frac{[(2j+1)(2l+1)(2j''+1)(2l''+1)]^{\frac{1}{2}}}{(2\lambda+1)} \\ &\times C_{000}^{jj''\lambda} C_{000}^{ll''\lambda} W(jlj''l'';J\lambda) , \end{aligned} \tag{2.36}$$

is an algebraic coefficient independent of the projection quantum number M. The coefficients $f_\lambda(jl,j''l'';J)$ are known as 'Percival–Seaton coefficients' and were first introduced by Percival and Seaton in [24]. We may rewrite the coupled equations (2.23) as

$$\begin{aligned} &\left[\frac{\mathrm{d}^2}{\mathrm{d}R^2} - \frac{l(l+1)}{R^2} + k_j^2\right] F^{j'l'}(jlpJ|R) \\ &= 2\mu \sum_{j''l''\lambda} v_\lambda(R) f_\lambda(jl,j''l'';J) F^{j'l'}(j''l''pJ|R) . \end{aligned} \tag{2.37}$$

We note that equation (2.37) is independent of M.

Examination of these equations provides insight into the relationship between the interaction potential and allowed transitions. For example when $\lambda = 0$ the Clebsch–Gordan coefficients in equation (2.36) are non–zero only when $j = j''$ and $l = l''$ and thus no collisional coupling between the rotational states of the molecule BC can occur. The $\lambda = 0$ term in the interaction potential is *angle independent.* It cannot induce rotationally inelastic transitions in the molecule. Hence $v_0(R)$ corresponds to *elastic scattering* of A on BC.

Terms with $\lambda \geq 1$ can induce rotationally inelastic transitions assuming the *triangular inequalities* $|j - j''| \leq \lambda \leq j + j''$ and $|l - l''| \leq \lambda \leq l + l''$, and the requirement that $j + j'' + \lambda$ should be an even integer are satisfied. These criteria ensure the Clebsch-Gordan coefficients are non-zero and hence collisional coupling between different states of the molecule can occur. Hence, if $j = 0$ then $\lambda = j' = j' - j \equiv \Delta j$. For example, in the molecule, HD, the transition $j = 0 \rightarrow j' = 1$ is induced by the $\lambda = 1$ term in the interaction potential. Similarly the $j = 0 \rightarrow j' = 2$ transition is induced by the $\lambda = 2$ term. The absolute magnitudes of $v_\lambda(R)$, in the expansion of the interaction potential (see equation (2.25)), tend to decrease as λ increases and so the probability of transitions involving higher Δj become smaller.

For homonuclear molecules, such as H_2 , the interaction potential is invariant under exchange of B and C. This is equivalent to the coordinate transformation $\theta' \rightarrow \pi - \theta'$. Since $\cos(\pi - \theta') = -\cos\theta'$, and

$$P_\lambda(-\cos\theta') = P_\lambda(\cos\theta') \ , \tag{2.38}$$

when λ is even, and

$$P_\lambda(-\cos\theta') = -P_\lambda(\cos\theta') \ , \tag{2.39}$$

when λ is odd, hence only terms with even values of λ appear in the interaction potential. Because $j + j' + \lambda$ must be an even integer, collisional transitions between even and odd values of j are forbidden.

2.2.2 The ‘body–fixed’ frame method

The polar angles of the rotor, BC, relative to the BF frame are given by (θ', ϕ').

To determine the coupled-channel equations in the body–fixed frame (BF) we follow a similar approach as that used for the SF case. We begin by expressing the wave function of the rotor in terms of a complete orthonormal set of functions $Y_{j\Omega}(\theta', \phi')$, where Ω is the projection of $\mathbf{j}$, the angular momentum of the rotor, on the BF Z-axis. To establish the relationship between between the BF functions, $Y_{j\Omega}(\theta', \phi')$, and SF functions, $Y_{jm}(\theta, \phi)$, we make use of the *Euler angles* and the *rotation matrix*, $\mathbf{D}$ [27].

The Euler angles (α, β, γ) describe a sequence of rotations that takes the SF coordinate system into the BF coordinate system. The rotations are taken in the positive sense. The first rotation is α about the z-axis, the second is β about the new y-axis, and the third is γ about the new z-axis. In this case the Euler angles are $\alpha = \Phi$, $\beta = \Theta$, and γ is taken to be zero. The elements of the rotation matrix, $\mathbf{D}$, as defined by Rose [27] are

$$D^{j}_{m''m}(\alpha, \beta, \gamma) = \langle jm''|\mathrm{e}^{-\mathrm{i}\alpha j_z}\mathrm{e}^{-\mathrm{i}\beta j_y}\mathrm{e}^{-\mathrm{i}\gamma j_z}|jm\rangle \ , \tag{2.40}$$

where $|jm\rangle = Y_{jm}(\theta, \phi)$ and j_z, j_y are components of the angular momentum operator in the SF system, and where

$$j_x^2 + j_y^2 + j_z^2 = \mathbf{j}^2 \ . \tag{2.41}$$

Using the quantum theory of angular momentum, we may rewrite equation (2.40) as

$$D^{j}_{m''m}(\alpha, \beta, \gamma) = \mathrm{e}^{-\mathrm{i}m''\alpha} d^{j}_{m''m}(\beta) \mathrm{e}^{-\mathrm{i}m\gamma} \ , \tag{2.42}$$

with

$$d^{j}_{m''m}(\beta) = \langle jm''|\mathrm{e}^{-\mathrm{i}\beta j_y}|jm\rangle \ . \tag{2.43}$$

Explicit expressions for $d^{j}_{m''m}(\beta)$ are given in [27].

Using equation (2.40) we may obtain

$$Y_{jm}(\theta, \phi) = \sum_{\Omega} D^{j*}_{m\Omega}(\Phi, \Theta, 0) Y_{j\Omega}(\theta', \phi') \ , \tag{2.44}$$

and the following inverse relation

$$Y_{j\Omega}(\theta', \phi') = \sum_{m} D^{j}_{m\Omega}(\Phi, \Theta, 0) Y_{jm}(\theta, \phi) \ . \tag{2.45}$$

The functions in equation (2.45) are eigenfunctions of $\mathbf{j}^2$ and j_Z with eigenvalues $j(j+1)$ and Ω, respectively.

We now consider the BF equivalent of the SF eigenfunctions, $\mathcal{Y}_{jlJM}$. These BF functions will be eigenfunctions of $\mathbf{J}^2$ and J_Z.

Through use of equation (2.44) and the following relationship

$$Y_{lm_l}(\Theta,\Phi) = \left(\frac{2l+1}{4\pi}\right)^{\frac{1}{2}} D^{l*}_{m_l0}(\Phi,\Theta,0) \ , \tag{2.46}$$

we may re-express equation (2.12) as

$$\begin{aligned}\mathcal{Y}_{jlJM}(\theta,\phi;\Theta,\Phi) = \left(\frac{2l+1}{4\pi}\right)^{\frac{1}{2}} \sum_{\substack{mm_l\\ \Omega}} C^{jlJ}_{mm_lM} Y_{j\Omega}(\theta',\phi') \\ \times D^{j*}_{m\Omega}(\Phi,\Theta,0) D^{l*}_{m_l0}(\Phi,\Theta,0) \ .\end{aligned} \tag{2.47}$$

Using the Clebsch–Gordan series [27] we obtain

$$D^{j}_{m\Omega}(\Phi,\Theta,0) D^{l}_{m_l0}(\Phi,\Theta,0) = \sum_{J''} C^{jlJ''}_{mm_lM} C^{jlJ''}_{\Omega0\Omega} D^{J''}_{M\Omega}(\Phi,\Theta,0) \ , \tag{2.48}$$

and as the Clebsch–Gordan coefficients are real we may rewrite equation (2.47) as

$$\begin{aligned}\mathcal{Y}_{jlJM}(\theta,\phi;\Theta,\Phi) = \left(\frac{2l+1}{4\pi}\right)^{\frac{1}{2}} \sum_{\substack{mm_l\\ J''\Omega}} C^{jlJ}_{mm_lM} C^{jlJ''}_{mm_lM} C^{jlJ''}_{\Omega0\Omega} \\ \times Y_{j\Omega}(\theta',\phi') D^{J''*}_{M\Omega}(\Phi,\Theta,0) \ .\end{aligned} \tag{2.49}$$

With use of the following orthonormality relation of the Clebsch-Gordan coefficients [30]

$$\sum_{mm_l} C^{jlJ}_{mm_lM} C^{jlJ''}_{mm_lM''} = \delta_{JJ''}\delta_{MM''} \ , \tag{2.50}$$

we may rewrite (2.49) as

$$\mathcal{Y}_{jlJM}(\theta,\phi;\Theta,\Phi) = \left(\frac{2l+1}{2J+1}\right)^{\frac{1}{2}} \sum_{\Omega} C^{jlJ}_{\Omega0\Omega} \mathcal{Z}_{j\Omega JM}(\theta',\phi';\Theta,\Phi) \ , \tag{2.51}$$

where

$$\mathcal{Z}_{j\Omega JM}(\theta',\phi';\Theta,\Phi) = \left(\frac{2J+1}{4\pi}\right)^{\frac{1}{2}} D^{J*}_{M\Omega}(\Phi,\Theta,0) Y_{j\Omega}(\theta',\phi') \ , \tag{2.52}$$

is an eigenfunction of $\mathbf{J}^2$ and J_Z. These eigenfunctions are the BF frame equivalent of $\mathcal{Y}_{jlJM}$ with equation (2.51) specifying the unitary transformation that relates the eigenfunctions of $\mathbf{J}^2$ in the SF frame, $\mathcal{Y}_{jlJM}(\theta,\phi;\Theta,\Phi)$, to the corresponding eigenfunctions in the BF frame, $\mathcal{Z}_{j\Omega JM}(\theta',\phi';\Theta,\Phi)$.

Equation (2.51) is an important result as it allows quantities evaluated in the BF frame to be transformed into the SF frame. (**Note:** As the BF Z-axis is taken to be coincident with MA, the projection of the orbital angular momentum, $\mathbf{l}$, of A relative to BC on this axis is zero, as $\mathbf{l}$ is perpendicular to MA. Therefore, $j_Z = J_Z$.)

We now consider the conservation of parity in the BF frame. Operating on equation (2.52) with P we find

$$\begin{aligned} P\mathcal{Z}_{j\Omega JM}(\theta',\phi';\Theta,\Phi) &= \mathcal{Z}_{j\Omega JM}(\theta',\pi-\phi';\pi-\Theta,\pi+\Phi) \\ &= (-1)^J\mathcal{Z}_{j,-\Omega JM}(\theta',\phi';\Theta,\Phi)\ . \end{aligned} \tag{2.53}$$

We see that $\mathcal{Z}_{j\Omega JM}$ is not an eigenfunction of P as Ω appears on the left side, and $-\Omega$ appears on the right side of equation (2.53). We may form such eigenfunctions from the linear combination

$$\mathcal{Z}_{j\bar{\Omega}\epsilon JM} = \frac{\left(\mathcal{Z}_{j\bar{\Omega}JM} + \epsilon\mathcal{Z}_{j,-\bar{\Omega}JM}\right)}{[2(1+\delta_{\bar{\Omega}0})]^{\frac{1}{2}}}\ , \tag{2.54}$$

where $\bar{\Omega} = |\Omega|$ and $\epsilon = \pm 1$. Operating on $\mathcal{Z}_{j\bar{\Omega}\epsilon JM}$ with P we find they are eigenfunctions of P with eigenvalues $p'' = (-1)^J\epsilon$. When $\epsilon = (-1)^{j+l+J}$ we find $p'' = p$, and $\mathcal{Y}_{jlJM}$ and $\mathcal{Z}_{j\bar{\Omega}\epsilon JM}$ are related by

$$\begin{aligned} \mathcal{Y}_{jlJM}(\theta,\phi;\Theta,\Phi) = \sum_{\bar{\Omega}} &\left[\frac{2(2l+1)}{(1+\delta_{\bar{\Omega}0})(2J+1)}\right]^{\frac{1}{2}} C^{jlJ}_{\bar{\Omega}0\bar{\Omega}} \\ &\times\mathcal{Z}_{j\bar{\Omega}\epsilon JM}(\theta',\phi';\Theta,\Phi)\ . \end{aligned} \tag{2.55}$$

Transforming from the SF to the BF frame leaves the parity of the wave function unchanged. Therefore equation (2.55) is only applicable when $p'' = p$. With $p'' = p = (-1)^J\epsilon$ we may rewrite equation (2.54) as

$$\mathcal{Z}_{j\bar{\Omega}pJM} = \frac{\left(\mathcal{Z}_{j\bar{\Omega}JM} + (-1)^J p\mathcal{Z}_{j,-\bar{\Omega}JM}\right)}{[2(1+\delta_{\bar{\Omega}0})]^{\frac{1}{2}}}\ .$$

We may now use the BF functions $\mathcal{Z}_{j\bar{\Omega}pJM}(\theta',\phi';\Theta,\Phi)$ as a basis to expand the total wave function, Ψ, as

$$\Psi(\hat{\mathbf{r}}',\mathbf{R}) = \sum_{j\bar{\Omega}pJM} \frac{G^{j'\bar{\Omega}'}(j\bar{\Omega}pJM|R)}{R}\mathcal{Z}_{j\bar{\Omega}pJM}(\hat{\mathbf{r}}';\hat{\mathbf{R}})\ , \tag{2.56}$$

where $\hat{\mathbf{r}}' = (\theta', \phi')$, $\hat{\mathbf{R}} = (\Theta, \Phi)$ and $\mathbf{R} = (R, \Theta, \Phi)$ are polar coordinates. Using the orthonormality properties of $\mathcal{Z}_{j\bar{\Omega}pJM}$

$$\int \mathcal{Z}^*_{j\bar{\Omega}pJM}(\hat{\mathbf{r}}'; \hat{\mathbf{R}}) \mathcal{Z}_{j''\bar{\Omega}''p''J''M''}(\hat{\mathbf{r}}'; \hat{\mathbf{R}}) \mathrm{d}\hat{\mathbf{r}}' \, \mathrm{d}\hat{\mathbf{R}} = \delta_{jj''}\delta_{\bar{\Omega}\bar{\Omega}''}\delta_{pp''}\delta_{JJ''}\delta_{MM''} \ ,$$

and operating on the left of equation (2.21) with

$$\int \mathrm{d}\hat{\mathbf{r}}' \, \mathrm{d}\hat{\mathbf{R}} \ \mathcal{Z}^*_{j\bar{\Omega}pJM}(\hat{\mathbf{r}}'; \hat{\mathbf{R}}) \ ,$$

we obtain the following coupled-equations in the BF frame

$$\begin{aligned} &\left[\frac{\mathrm{d}^2}{\mathrm{d}R^2} + k_j^2\right] G^{j'\bar{\Omega}'}(j\bar{\Omega}pJM|R) \\ &= 2\mu \sum_{j''\bar{\Omega}''p''J''M''} \langle j\bar{\Omega}pJM|V(R,\theta') + \frac{\mathbf{l}^2}{2\mu R^2}|j''\bar{\Omega}''p''J''M''\rangle \\ &\qquad G^{j'\bar{\Omega}'}(j''\bar{\Omega}''p''J''M''|R) \ . \end{aligned} \tag{2.57}$$

When considering the matrix elements of the potential in equation (2.57) we introduce the *effective potential* V_{eff},

$$V_{\text{eff}}(r, \theta') = V(R, \theta') + \mathbf{l}^2/(2\mu R^2) \ . \tag{2.58}$$

The matrix of elements of the effective potential V_{eff} are given by

$$\begin{aligned} &\langle j\bar{\Omega}pJM|V(R,\theta') + \frac{\mathbf{l}^2}{(2\mu R^2)}|j''\bar{\Omega}''p''J''M''\rangle \\ &= \int \mathcal{Z}^*_{j\bar{\Omega}pJM}(\hat{\mathbf{r}}'; \hat{\mathbf{R}}) \left[V(R,\theta') + \frac{\mathbf{l}^2}{(2\mu R^2)}\right] \mathcal{Z}_{j''\bar{\Omega}''p''J''M''}(\hat{\mathbf{r}}'; \hat{\mathbf{R}}) \mathrm{d}\hat{\mathbf{r}}' \, \mathrm{d}\hat{\mathbf{R}} \end{aligned} \tag{2.59}$$

We first consider the contribution due to the interaction potential $V(R, \theta')$ to the integral in equation (2.59). We make use of the BF basis functions from equation (2.52), the following relation

$$P_\lambda(\cos\theta') = \left(\frac{4\pi}{2\lambda + 1}\right)^{\frac{1}{2}} Y_{\lambda 0}(\theta', \phi') \ , \tag{2.60}$$

the orthogonality relation for the rotation matrix elements D

$$\int D^J_{M\Omega}(\Phi, \Theta, 0) D^{J''*}_{M''\Omega}(\Phi, \Theta, 0) \sin\Theta \ \mathrm{d}\Theta \ \mathrm{d}\Phi = \delta_{JJ''}\delta_{MM''} \left(\frac{4\pi}{2J+1}\right) \ , \tag{2.61}$$

the composition relation for spherical harmonics

$$\int Y^*_{j\Omega}(\hat{\mathbf{r}}')Y_{\lambda 0}(\hat{\mathbf{r}}')Y_{j''\Omega''}(\hat{\mathbf{r}}')\mathrm{d}\hat{\mathbf{r}}' = \delta_{\Omega\Omega''}\left[\frac{(2j''+1)(2\lambda+1)}{4\pi(2j+1)}\right]^{\frac{1}{2}} C^{j''\lambda j}_{\Omega 0\Omega} C^{j''\lambda j}_{000} \,, \tag{2.62}$$

to obtain

$$\begin{aligned} &\langle j\bar{\Omega}pJM|V(R,\theta')|j''\bar{\Omega}''p''J''M''\rangle \\ &= \delta_{\bar{\Omega}\bar{\Omega}''}\delta_{pp''}\delta_{JJ''}\delta_{MM''}(-1)^{\bar{\Omega}}\sum_{\lambda} v_{\lambda}(R)\frac{[(2j+1)(2j''+1)]^{\frac{1}{2}}}{(2\lambda+1)} \\ &\quad \times C^{jj''\lambda}_{000} C^{jj''\lambda}_{\bar{\Omega},-\bar{\Omega}0} \,. \end{aligned} \tag{2.63}$$

The Kronecker δ symbols ensure the same conservation properties ($J = J''$, $M = M''$, $p = p''$) as those obtained in the SF analysis. In addition, $\bar{\Omega} = \bar{\Omega}''$, is conserved. This arises from the invariance of the potential under rotations about the BF Z-axis, as $V(R,\theta')$ is independent of ϕ'.

We now consider the contribution of the centrifugal potential operator in equation (2.59). Using the quantum theory of angular momentum, it may be shown [25], [31], [32]

$$\begin{aligned} &\langle j\bar{\Omega}pJM|\frac{\mathbf{l}^2}{2\mu R^2}|j\bar{\Omega}pJM\rangle \\ &= \frac{J(J+1)+j(j+1)-2\bar{\Omega}^2}{2\mu R^2} \,, \end{aligned} \tag{2.64}$$

and

$$\begin{aligned} &\langle j\bar{\Omega}pJM|\frac{\mathbf{l}^2}{2\mu R^2}|j,\bar{\Omega}\pm 1,pJM\rangle \\ &= -(1+\delta_{\bar{\Omega}0})^{\frac{1}{2}}(1+\delta_{\bar{\Omega}\pm 1,0})^{\frac{1}{2}} \\ &\times\frac{[J(J+1)-\bar{\Omega}(\bar{\Omega}\pm 1)]^{\frac{1}{2}}[j(j+1)-\bar{\Omega}(\bar{\Omega}\pm 1)]^{\frac{1}{2}}}{2\mu R^2} \,. \end{aligned} \tag{2.65}$$

Matrix elements for the case $|\Omega'' - \bar{\ }\,| > \Omega$ are equal to zero. The additional complexity of equations (2.64) and (2.65) when compared to their SF counterparts is due to the existence of Coriolis and centrifugal forces in the BF frame.

We observe that equations (2.63–2.65) are independent of the projection quantum number, M. Hence,we may rewrite the coupled equations (2.57) as

$$\begin{aligned}&\left[\frac{\mathrm{d}^2}{\mathrm{d}R^2} + k_j^2\right] G^{j'\bar{\Omega}'}(j\bar{\Omega}pJ|R)\\ &= 2\mu \sum_{j''\bar{\Omega}''} V_{\text{eff}}(j\bar{\Omega}, j''\bar{\Omega}''; J|R) G^{j'\bar{\Omega}'}(j''\bar{\Omega}''pJ|R)\ ,\end{aligned} \tag{2.66}$$

where $V_{\text{eff}}(j\bar{\Omega}, j''\bar{\Omega}''; J|R)$ denotes a matrix element, from equation (2.59), of the effective potential, from equation (2.58).

2.3 Scattering of an atom by a vibrating rotor

We now consider the case of an atom colliding with a vibrating rotor. In doing so we must allow for the extra degree of freedom, of the diatom BC, given by the internuclear distance (vibrational coordinate), r. The interaction potential is now given by

$$V(r, R, \theta') = \sum_{\lambda=0}^{\infty} v_\lambda(r, R) P_\lambda(\cos\theta')\ . \tag{2.67}$$

This summation is, in principle, infinite but is usually truncated to a small number of terms when solving the problem computationally.

Consider the eigenvalue equation

$$H\Psi = E\Psi, \tag{2.68}$$

which may be solved in the space–fixed (SF) coordinates, $\Psi = \Psi(\mathbf{r}, \mathbf{R})$, or body–fixed (BF) coordinates, $\Psi = \Psi(\mathbf{r}', \mathbf{R})$.We note that $|r| = |r'|$.

The Hamiltonian, H, of the atom–molecule system is given by

$$H = h - \frac{\nabla_R^2}{2\mu} + V(r, R, \theta'), \tag{2.69}$$

where

$$h = -\frac{\nabla_r^2}{2m} + v(r), \tag{2.70}$$

is the internal Hamiltonian of the diatomic molecule BC at infinite separation from the atom, and $m = m_B m_C/(m_B + m_C)$ is the reduced mass of the molecule.

The kinetic energy operator in equation (2.70) is given by

$$-\frac{1}{2m}\nabla_r^2 = -\frac{1}{2mr}\frac{\partial^2}{\partial r^2}r + \frac{\mathbf{j}^2}{2mr^2} , \tag{2.71}$$

where $\mathbf{j}$ is the rotational angular momentum of the molecule.

The eigenvalue equation for the isolated vibrating rotor is given by

$$h\psi(\mathbf{r}) = \epsilon\psi(\mathbf{r}) , \tag{2.72}$$

with the vibrational eigenfunctions, $\psi(\mathbf{r})$, taking the form

$$\psi(\mathbf{r}) = \frac{\chi(\nu j|r)}{r}Y_{jm_j}(\hat{\mathbf{r}}) , \tag{2.73}$$

where ν is the vibrational quantum number.

The rovibrational wave functions, $\chi(\nu j|r)$, satisfy

$$\left[-\frac{\mathrm{d}^2}{\mathrm{d}r^2} + \frac{j(j+1)}{r^2} + 2mv(r) - \kappa^2\right]\chi(\nu j|r) = 0 , \tag{2.74}$$

where $\kappa^2 = 2m\epsilon$.

We may solve (2.74) numerically subject to the boundary conditions

$$\chi(\nu j|r) \to 0 ,$$

as $r \to 0$ or $r \to \infty$. Alternatively we may wish to approximate the form of the internuclear potential, $v(r)$, for which the wave functions $\chi(\nu j|r)$ are known analytically. The evaluation of the vibrational eigenfunctions is discussed further in Section 4.1.

As in the case for equation (2.16) and equation (2.56), the total wave function Ψ of the atom–molecule system is expanded as functions of radial and angular coordinates. For the SF coordinates case we have

$$\Psi(\mathbf{r},\mathbf{R}) = \sum_{\nu jlpJM} \frac{F^{\nu' j' l'}(\nu jlpJM|R)}{R}\frac{\chi(\nu j|r)}{r}\mathcal{Y}_{jlpJM}(\hat{\mathbf{r}};\hat{\mathbf{R}}) , \tag{2.75}$$

and for the case of BF coordinates

$$\Psi(\mathbf{r}',\mathbf{R}) = \sum_{\nu j\bar{\Omega}pJM} \frac{G^{\nu' j'\bar{\Omega}'}(\nu j\bar{\Omega}pJM|R)}{R}\frac{\chi(\nu j|r)}{r}\mathcal{Z}_{j\bar{\Omega}pJM}(\hat{\mathbf{r}}';\hat{\mathbf{R}}) . \tag{2.76}$$

Using an approach analogous to the rigid rotor case, the eigenvalue equation (2.68) may be reduced to a set of coupled differential equations. For the SF case we obtain

$$\begin{aligned}&\left[\frac{\mathrm{d}^2}{\mathrm{d}R^2} - \frac{l(l+1)}{R^2} + k_{\nu j}^2\right] F^{\nu' j' l'}(\nu j l p J|R)\\ &= 2\mu \sum_{\nu'' j'' l'' \lambda} f_\lambda(jl, j''l''; J) y_\lambda(\nu j, \nu'' j''|R) F^{\nu' j' l'}(\nu'' j'' l'' p J|R) \ , \qquad (2.77)\end{aligned}$$

where

$$y_\lambda(\nu j, \nu'' j''|R) = \int_0^\infty \chi^*(\nu j|r) v_\lambda(r,R) \chi(\nu'' j''|r) \mathrm{d}r \ , \qquad (2.78)$$

and $f_\lambda(jl, j''l''; J)$ is a Percival–Seaton coefficient given by (2.36), $k_{\nu j}^2 = 2\mu(E - \epsilon_{\nu j})$, where $\epsilon_{\nu j}$ is the rovibrational energy of the molecule BC in the state (ν, j). The coefficient $y_\lambda(\nu j, \nu'' j''|R)$ determines the coupling between the vibrational states ν and ν''.

For the case of the BF coordinate system, equation (2.76), we obtain the following coupled equations

$$\begin{aligned}&\left[\frac{\mathrm{d}^2}{\mathrm{d}R^2} + k_{\nu j}^2\right] G^{\nu' j' \bar{\Omega}'}(\nu j \bar{\Omega} p J|R)\\ &= 2\mu \sum_{\nu'' j'' \bar{\Omega}''} V_{\mathrm{eff}}(\nu j \bar{\Omega}, \nu'' j'' \bar{\Omega}''; J|R) G^{\nu' j' \bar{\Omega}'}(\nu'' j'' \bar{\Omega}'' p J|R) \ , \qquad (2.79)\end{aligned}$$

where

$$\begin{aligned}&V_{\mathrm{eff}}(\nu j \bar{\Omega}, \nu'' j'' \bar{\Omega}''; J|R)\\ &= \langle \nu j \bar{\Omega} p J M | V(r,R,\theta') + \frac{\mathbf{l}^2}{2\mu R^2} | \nu'' j'' \bar{\Omega}'' p J M \rangle \ , \qquad (2.80)\end{aligned}$$

are the matrix elements of the effective potential

$$V_{\mathrm{eff}}(r,R,\theta') = V(r,R,\theta') + \frac{\mathbf{l}^2}{2\mu R^2} \ , \qquad (2.81)$$

and are independent of the projection quantum number, M.

The non–vanishing elements of $\mathbf{l}^2/(2\mu R^2)$ are given by equation (2.64) and equation (2.65). The non–vanishing elements of $V(r,R,\theta')$ are

$$\begin{aligned}&\langle \nu j \bar{\Omega} p J M | V(r,R,\theta') | \nu'' j'' \bar{\Omega} p J M \rangle\\ &= (-1)^{\bar{\Omega}} \sum_\lambda \frac{[(2j+1)(2j''+1)]^{\frac{1}{2}}}{(2\lambda+1)} C_{000}^{jj''\lambda} C_{\bar{\Omega},-\bar{\Omega}0}^{jj''\lambda} y_\lambda(\nu j, \nu'' j''|R) \ , \qquad (2.82)\end{aligned}$$

where $y_\lambda(\nu j, \nu'' j''|R)$ is given by equation (2.78).

2.4 Solving the equations

The scattering problems considered in this thesis are concerned with problems where

$$V(R,\theta') >> E \ ,$$

as $R \to 0$, and

$$V(R,\theta') \sim R^{-n} \ ,$$

as $R \to \infty$, where $n \geq 2$ is an integer. Boundary conditions are required for the SF and BF frame cases to solve the coupled equations. The first boundary condition appropriate for these problems is

$$F^{\nu'j'l'}(\nu jlpJ|R) \to 0 \ ,$$

or

$$G^{\nu'j'\bar{\Omega}'}(\nu j\bar{\Omega}pJ|R) \to 0 \ ,$$

as $R \to 0$. This boundary condition is in the classically forbidden region, where the potential is much greater than the total energy, and is typically located near the origin.

The solutions are propagated numerically, from the classically forbidden region, into the *asymptotic region* where the potential V has become vanishingly small (i.e. very small compared to the collision energy). The asymptotic region is usually taken to occur at large values of R. When using the BF frame solution a unitary transformation is applied in the asymptotic region to convert it to the SF frame solution. The transformation used is analogous to that in equation (2.51). This transformation is required as the quantities we wish to calculate (e.g. cross sections) are measured experimentally in a space-fixed (or laboratory) frame.

The information from the scattering event is obtained by matching the SF solutions to the appropriate asymptotic ($R \to \infty$) forms [33]

$$\begin{aligned} F^{\gamma' l'}(\gamma lpJ|R) &\sim \delta_{\gamma\gamma'}\delta_{ll'} \sin\left(k_{\gamma'}R - \frac{l'\pi}{2}\right) \\ &+ \left(\frac{k_{\gamma'}}{k_{\gamma}}\right)^{\frac{1}{2}} K^{\gamma' l'}(\gamma lpJ) \cos\left(k_{\gamma}R - \frac{l\pi}{2}\right) \ , \end{aligned} \tag{2.83}$$

where γ denotes νj, γ' denotes $\nu' j'$, and $K^{\gamma' l'}(\gamma l p J)$ are elements of the reactance matrix $\mathbf{K}$. We use matrix notation for efficiency. The transmission matrix, $\mathbf{T}$, and the scattering matrix, $\mathbf{S}$, are given by

$$\begin{aligned} \mathbf{T} &= -2\mathrm{i}\mathbf{K}(1-\mathrm{i}\mathbf{K})^{-1} \\ &\equiv \mathbf{1}-\mathbf{S} \, . \end{aligned} \tag{2.84}$$

All the information from the scattering event is contained in these three matrices. All derivable collision quantities may be obtained using these matrices. The probability, P, of transition $\gamma' \rightarrow \gamma$ is given by

$$P_{Jp}(\gamma \rightarrow \gamma') = \frac{1}{(2j+1)} \sum_{ll'} |T^{\gamma' l'}(\gamma l p J)|^2 \, , \tag{2.85}$$

for each value of J and p. The transition probabilities are used to determine the total cross sections which are given by

$$\sigma(\gamma \rightarrow \gamma') = \frac{\pi}{k_\gamma^2} \sum_{Jp} (2J+1) P_{Jp}(\gamma \rightarrow \gamma') \, . \tag{2.86}$$

Finally, the principle of detailed balance gives the relationship between cross sections for a transition and its reverse process as

$$\sigma(\gamma \leftarrow \gamma') k_{\gamma'}^2 \omega_{\gamma'} = \sigma(\gamma' \leftarrow \gamma) k_\gamma^2 \omega_\gamma \, . \tag{2.87}$$

where ω_γ is the statistical weight

$$\omega_\gamma = \omega_{\nu j} = 2j+1 \, ,$$

and $k_\gamma = k_{\nu j}$, with $k_{\nu j}^2 = 2\mu(E - \epsilon_{\nu j})$.

So far the theoretical determination of the cross sections has been presented. In Section 4.4 the computational methods used to solve the equations are discussed.

2.5 Determination of rate coefficients

Rate coefficients are often required for the interpretation of experimental data or astronomical observations. They are related to the cross sections through

$$\langle \sigma v \rangle = \int_0^\infty v \sigma(v) f(v,T) \; dv \, , \tag{2.88}$$

where v denotes the relative collision velocity of the atom and molecule and

$$f(v,T) = 4\pi \left(\frac{\mu}{2\pi k_{\mathrm{B}}T}\right)^{\frac{3}{2}} \nu^2 \exp\left(-\frac{\mu\nu^2}{2k_{\mathrm{B}}T}\right) , \tag{2.89}$$

is the velocity distribution at kinetic temperature, T. The distribution chosen is of Maxwellian form. This form is justified as the elastic collisions in a molecular gas, which tend to thermalise the velocity distribution, occur more quickly than those for inelastic collisions (which also have smaller cross sections than elastic collisions). We define the dimensionless quantity, $x = \mu v^2/(2k_{\mathrm{B}}T)$, so that equation (2.88) can be re–written as

$$\langle\sigma v\rangle = \left(\frac{8k_{\mathrm{B}}T}{\pi\mu}\right)^{\frac{1}{2}} \int_0^\infty x\sigma(x)\mathrm{e}^{-x}\,\mathrm{d}x , \tag{2.90}$$

where $[8k_{\mathrm{B}}T/(\pi\mu)]^{\frac{1}{2}}$ is the mean relative collision velocity. The rate coefficients obtained using equation (2.90) are also known as *thermally–averaged rate coefficients.*

Rate coefficients for excitational transitions may readily be obtained from those of de–excitational transitions, and vice versa, using detailed balance

$$(2j+1)\langle\sigma v\rangle_{\nu j\to\nu' j'}(T) = (2j'+1)\langle\sigma v\rangle_{\nu' j'\to\nu j}(T)\exp\left[-\frac{(E_{\nu' j'} - E_{\nu j})}{k_{\mathrm{B}}T}\right] , \tag{2.91}$$

where k_{B} denotes Boltzmann's constant.

Chapter 3

Interaction potential

In this chapter the interaction potentials available for the H+H_2 system are discussed.

The interaction potential between two systems is defined as the change in total energy when the systems are brought together from infinite separation. When determining the interaction potential there can be considerable difficulties in performing experimental measurements. Therefore, theoretical methods are often used in conjunction with whatever reliable experimental data are available.

The interaction potential plays a fundamental role in the study of collisions. For collisions between an atom, A, and diatomic molecule, BC, the interaction potential, $V(r, R, \theta')$, and terms derived from it, v_λ, appear directly in the coupled–channel equations.

The theoretical calculation of interaction potentials [34] involves determining the total energy of the collection of all the electrons and nuclei in the systems present. The electronic motion is considerably faster than that of the nuclei, so the problem is reduced to determining the electronic energy as a function of fixed nuclear geometry (Born–Oppenheimer approximation). Typically, the largest contributions to the energy are the kinetic energy of the electrons, the Coulomb interactions between the electrons and the nuclei, and other effects such as spin-orbit interaction. Generally, when performing the calculation, the problem is broken down in to three parts:

1. **Long internuclear distances** – at large distances the systems can be described as non–overlapping charge distributions. The calculation then reduces to a standard electrostatic problem of interacting permanent and induced dipole moments. In this region the interaction is small and can be represented accurately as a perturbation of separated systems.

2. **Small internuclear distances** – where the charge distribution of the systems overlap strongly, and the interaction is repulsive. In this region the systems can be described as a single molecule and molecular orbital techniques such as the Hartree–Fock (HF) method may be used.

3. **Intermediate internuclear distances** – are the most difficult to perform calculations for as the long–range attractive forces and short–range repulsive forces compete to perform a potential well. In this region the perturbative and HF methods become inadequate and configuration interaction (CI) methods must be used.

Calculations are performed for a large number of nuclear geometries resulting in an equally large number of interaction energies. The energies are then fitted to a suitable polynomial form, so that interaction energies may be calculated for arbitrary nuclear geometries. The quality of the fit is extremely important as the accuracy of the interaction potential is directly related to it.

The calculation of an accurate interaction potential is extremely detailed and computationally demanding. Only an overview has been presented here as calculations in this thesis only make use of the potential; no calculations were performed for determining the interaction potential of $H+H_2$.

3.1 Survey of previous potentials for $H+H_2$

A large number of theoretical and experimental studies have been performed for the $H+H_2$ system over the years. As a result, several interaction potentials have been computed. The most widely known are those of Liu [35], Varandas *et al.* [36], Boothroyd *et al.* [37], and Boothroyd *et al.* [38] which are denoted by LSTH, DMBE, BKMP1, and BKMP2, respectively. More recently the potential of Mielke *et al.* [39] has been made available. Whilst all these calculations agree with regard to the general features of the potential (which becomes repulsive at short range, displays only a shallow Van der Waals minimum of approximately ~2 meV (~20 K), and becomes attractive at long range) there remain significant differences in the predicted anisotropy of the potential; and it is the anisotropy which determines the magnitude of the rovibrationally inelastic cross sections.

3.2 Choosing the 'best' interaction potential

When performing the scattering calculations we wish to use the most accurate and suitable interaction potential available. This is achieved by examining the accuracy of the fit for each interaction potential and by surveying the performance in scattering calculations from previous work.

Table 3.1 compares the root-mean-square (rms) errors and largest errors for the fits of the interaction potentials of $H+H_2$. The potential with the smallest errors is that of Mielke *et al.* [39] which is the most recently calculated potential.

A considerable amount of work has previously been performed on the inelastic scattering of $H+H_2$. Forrey *et al.* [16] provide a detailed survey, of which a summary is given here. Full quantum calculations for rotationally inelastic cross sections at low velocities were performed by Sun and Dalgarno [13] using the DMBE potential, which was considered to be more accurate than the earlier LSTH potential. They found that rate coefficients calculated using the DMBE potential were larger. Semiclassical calculations were performed by Lepp, Buch and Dalgarno [40] using the DMBE and LSTH potentials which demonstrated that the differences in the size of the rate coefficients were largely due to the interaction potentials. Boothroyd *et al.* [38] conducted a comparison of the LSTH, DMBE, and BKMP1 potentials which concluded that the LSTH and DMBE potentials were too poorly constrained at the intermediate distances (~ 3.5 a_0) most responsible for low-energy rotational excitation. However, the BKMP1 was also found to be too weakly constrained in the critical interaction region so a refined potential, BKMP2, was developed. BKMP2 has the same functional form as BKMP1 but with additional constraints. Flower and Wroe [14], using the rigid rotor approximation showed that rotationally inelastic cross sections obtained using the BKMP1 potential were approximately an order of magnitude smaller than those obtained by Sun and Dalgarno [13] who used the DMBE potential. However, because the rigid rotor approximation underestimates the magnitude of rotational cross sections, it is difficult to determine how much of the difference is due to the potential and how much to the scattering approximation. Boothroyd *et al.* [38] performed quasi-classical trajectory calculations for the LSTH, DMBE, BKMP1, and BKMP2 potentials to confirm the sensitivity of low-energy rotational transition rate coefficients to the nature of the interaction potential. They suggested that the BKMP2 potential, and quantum mechanical calculations, are required when calculating low-temperature rate coefficients. Forrey *et al.* [16] used full coupled-channel calculations and a vibrating oscillator model to show that the BKMP2 potential is the most reliable for rotational transition cross sections. No previous calculations have been performed with the potential of Mielke *et al.* [39]. However Mielke *et al.* [39] claim that their potential offers a considerable improvement over earlier potentials.

After careful investigation the potentials of Boothroyd *et al.* [38] and Mielke *et al.* [39] were chosen for the scattering calculations presented in this thesis.

3.3 Comparing the interaction potentials

The interaction potentials are used to calculate the $y_\lambda(\nu j, \nu' j' | R)$ integrals. The magnitude and behaviour of cross sections for the $\nu j \rightarrow \nu' j'$ transitions are directly dependent on these integrals.

In Figure 3.1 the $y_\lambda(\nu j, \nu' j' | R)$ integrals are plotted for $\nu = \nu' = j = j' = 0$ and $\lambda = 0, 2$ using the potentials of Mielke *et al.* [39] and Boothroyd *et al.* [38]. There is excellent agreement for the isotropic term, $\lambda = 0$, but, as the expanded plot at the bottom of Figure 3.1 shows, there are important differences for the first non-zero anisotropic term, $\lambda = 2$. The calculations

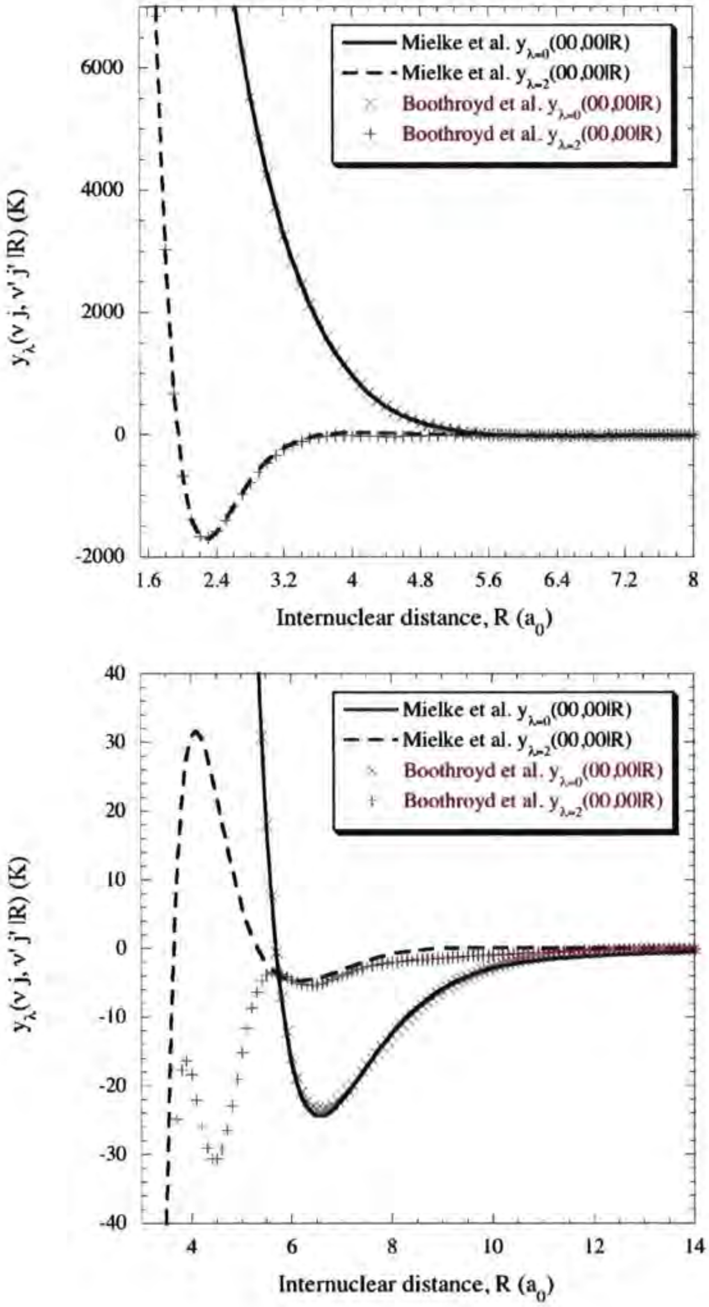

Figure 3.1: A comparison of $y_\lambda(\nu j, \nu' j'|R)$ using the potential of Mielke *et al.* [39] (lines) and the potential of Boothroyd *et al.* [38] (markers). In this Figure, $\nu = \nu' = j = j' = 0$. The 'exact oscillator' model was used for the molecule.

of Boothroyd *et al.* [38] imply a $\lambda = 2$ term which remains negative beyond its minimum, at $R = 2.25\ a_0$, whereas the calculations of Mielke *et al.* [39] lead to a $\lambda = 2$ term which varies between positive and negative values for $3.7 \leq R \leq 12.9\ a_0$. For atom–molecule separations that correspond to low classically–allowed energies, the v_2 term is small in magnitude for both potentials. Therefore, one would expect the rotationally inelastic cross sections to be small at low collision energies.

3.4 Summary

The H+H_2 system is the simplest triatomic system, in terms of its structure, but it has proved to be difficult to obtain an interaction potential which is sufficiently accurate to yield reliable collision cross sections near threshold. The interaction potential of Mielke *et al.* [39] (with an rms error of 3.25 K) represents a significant improvement in accuracy over earlier interaction potentials, such as that of Boothroyd *et al.* [38] (with an rms error of 85.59 K). The potential surface of Mielke *et al.* [39] should yield more accurate scattering data, particularly near–threshold cross sections and their corresponding low–temperature rate coefficients.

Surface (year)	rms error (K)	Largest deviation (K)
LSTH (1973)	85.55	276.77
DMBE (1987)	120.77	n/a
BKMP1 (1991)	80.51	608.89
BKMP2 (1996)	85.55	1957.51
Mielke *et al.* (2002)	3.25	87.56

Table 3.1: Root–mean–square (rms) errors and largest errors for the fits of the interaction potentials of $H+H_2$.

Chapter 4

Numerical Methods

In this chapter the numerical methods used in performing the scattering calculations are presented. For each calculation the method is presented, followed by details specific to our calculations.

4.1 Determination of rovibrational eigenfunctions

The rovibrational eigenfunctions were obtained by solving the following eigenvalue equation

$$h\psi(\mathbf{r}) = \epsilon\psi(\mathbf{r}) \ , \tag{4.1}$$

with the vibrational eigenfunctions, $\psi(\mathbf{r})$, taking the form

$$\psi(\mathbf{r}) = \frac{\chi(\nu j|r)}{r} Y_{jm_j}(\hat{\mathbf{r}}) \ , \tag{4.2}$$

where ν is the vibrational quantum number. The vibrational wave functions, $\chi(\nu j|r)$, satisfy

$$\left[-\frac{\mathrm{d}^2}{\mathrm{d}r^2} + \frac{j(j+1)}{r^2} + 2mv(r) - \kappa^2\right] \chi(\nu j|r) = 0 \ , \tag{4.3}$$

where $\kappa^2 = 2m\epsilon$. In determining $\chi(\nu j|r)$ we must decide what form of $v(r)$ to use. One may choose an approximate form of the internuclear potential, $v(r)$, for which the wave functions, $\chi(\nu j|r)$, are known analytically. One such approximation would be to approximate the vibrating rotor as a simple harmonic oscillator (SHO) where

$$v(r) = \frac{1}{2}K(r - r_0)^2 , \tag{4.4}$$

where the *force constant*, K, and the *equilibrium distance*, r_0, are determined by a best fit to the energy levels, as determined from spectroscopic data. The analytic wave functions for the harmonic oscillator potential are well known [41].

An alternative, and more accurate, form of $v(r)$ used was the Morse oscillator (MO) potential

$$v(r) = D\left[\mathrm{e}^{-a(r-r_0)} - 1\right]^2 . \tag{4.5}$$

The constants a and D were derived by a best fit to the spectroscopic data; D is the dissociation energy of the molecule measured relative to the minimum of the potential well, at $r = r_0$, where $v(r) = 0$. The wave functions for the MO potential are known analytically [42].

The 'exact oscillator' wave functions were determined by solving equation (4.3), using an internuclear potential $v(r)$ derived from the interaction potential (e.g. the potentials of Boothroyd *et al.* BKMP2 or Mielke *et al.* [39]) subject to the boundary condition

$$\chi(\nu j|r) \rightarrow 0 , \tag{4.6}$$

as $r \rightarrow 0$ or $r \rightarrow \infty$.

An alternative approximation to the 'exact oscillator' model is to neglect the centrifugal term, $\frac{j(j+1)}{r^2}$, in equation (4.3). In this case wave functions with no j–dependence are produced. This approximation is denoted as the ENCO model.

The wave functions for the ENCO and 'exact oscillator' models were obtained by solving equation (4.3) using the LEVEL [43] code. The internuclear potential was determined, for either interaction potential, by setting the atom-molecule distance to be very large (in theory, infinite) and then varying the internuclear distance, r, and noting $v(r)$. This data is inputted into LEVEL. The vibrational wave functions calculated using LEVEL were verified using the independent method and code of Marston *et al.* [44]. Excellent agreement was found between the codes.

In Figures 4.1–4.3 the wave functions for increasing vibrational quantum number, ν, are shown for the SHO and 'exact oscillator' models. Using the 'exact' internuclear potential has introduced an asymmetry within the wave functions. This is expected as the internuclear potential is also asymmetric. For larger ν the discrepancies between the SHO and 'exact oscillator' wave functions increase. As $j = 0$ in Figures 4.1–4.3 the wave functions for the 'exact oscillator' correspond to those for the ENCO model too.

In Figure 4.4 the effect of including the centrifugal term in equation (4.3) is shown for the $\nu = 1$ wave function. As j increases the wave function is 'stretched' towards increasing r. For large j this effect can become significant, for low j the effect is small. The case where $j = 0$ corresponds to the $\nu = 1$ wave function for the ENCO model.

For the scattering calculations presented in this thesis:

- Wave functions with $0 \leq \nu \leq 6$ and $0 \leq j \leq 28$, for even j, were calculated for para–H_2 .
- Wave functions with $0 \leq \nu \leq 6$ and $1 \leq j \leq 29$, for odd j, were calculated for ortho–H_2 .
- Wave functions with $0 \leq \nu \leq 6$ and $0 \leq j \leq 29$ were calculated for HD.

There was good agreement found between rovibrational eigenfunctions obtained using the potential of Boothroyd *et al.* [38] and the potential of Mielke *et al.* [39].

4.2 Determination of the potential expansion coefficients

The potential expansion coefficients $v_\lambda(r, R)$, in equation (2.67), were calculated by solving

$$v_\lambda(r, R) = \int_{-1}^{1} V(r, R, \theta')P_\lambda(\cos\theta')\mathrm{d}\cos\theta' \ , \tag{4.7}$$

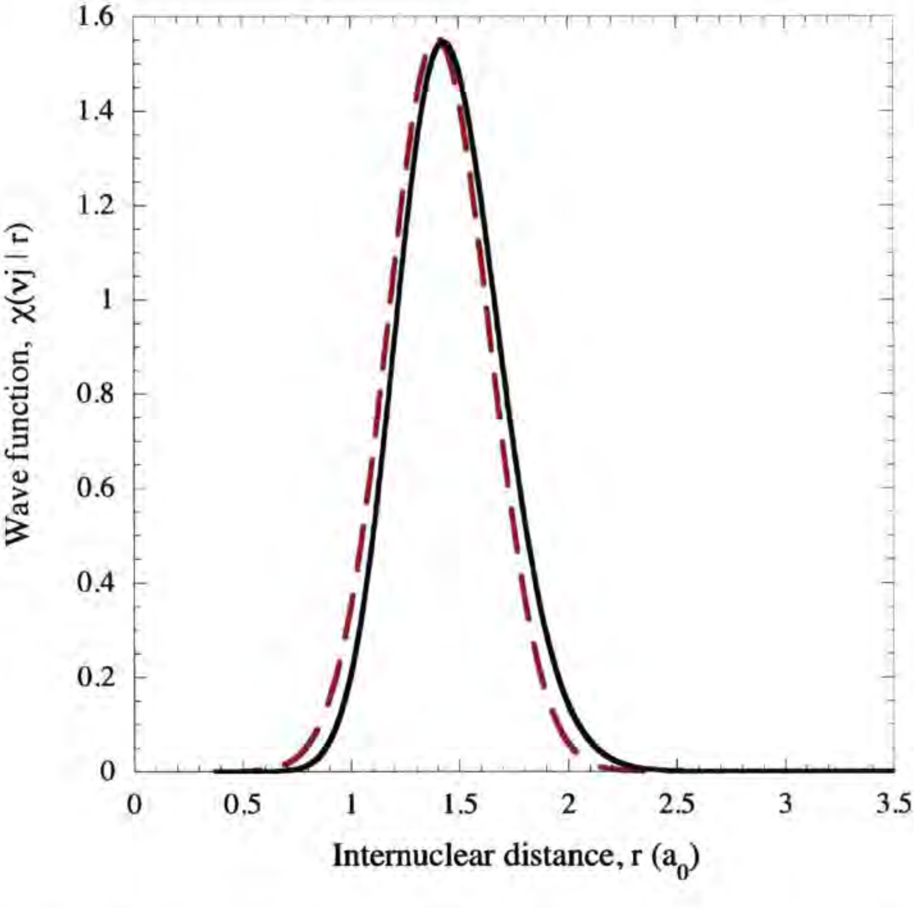

Figure 4.1: A comparison of results obtained for the $\nu = 0$, $j = 0$ wave function, $\chi(\nu j|r)$, using the SHO (broken curve) and 'exact oscillator' (full curve) models for H_2 . The interaction potential of Mielke *et al.* [39] was used in these calculations.

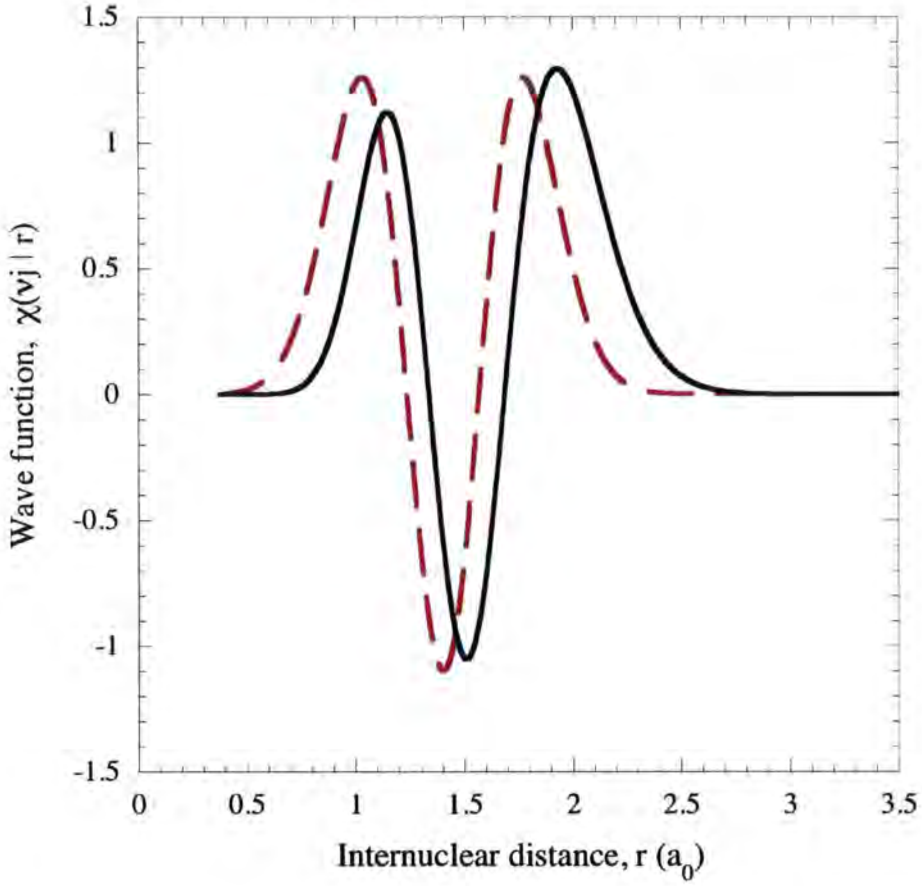

Figure 4.2: A comparison of results obtained for the $\nu = 2$, $j = 0$ wave function, $\chi(\nu j|r)$, using the SHO (broken curve) and 'exact oscillator' (full curve) models for H_2 . The interaction potential of Mielke *et al.* [39] was used in these calculations.

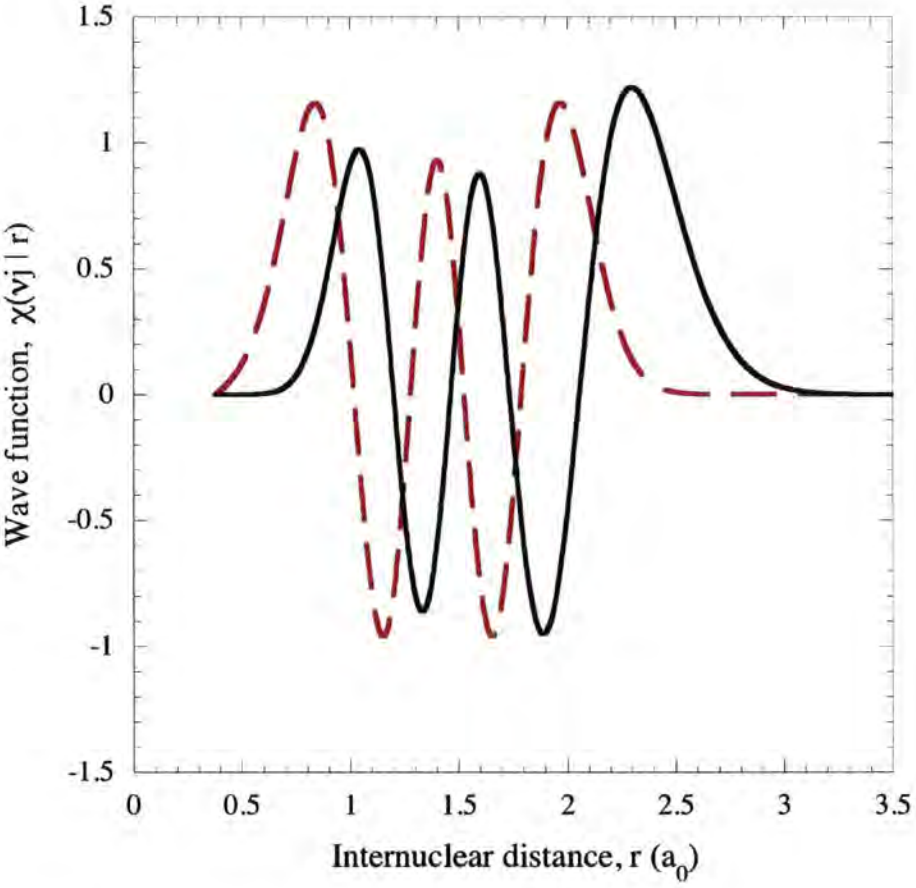

Figure 4.3: A comparison of results obtained for the $\nu = 4$, $j = 0$ wave function, $\chi(\nu j|r)$, using the SHO (broken curve) and 'exact oscillator' (full curve) models for H_2 . The interaction potential of Mielke *et al.* [39] was used in these calculations.

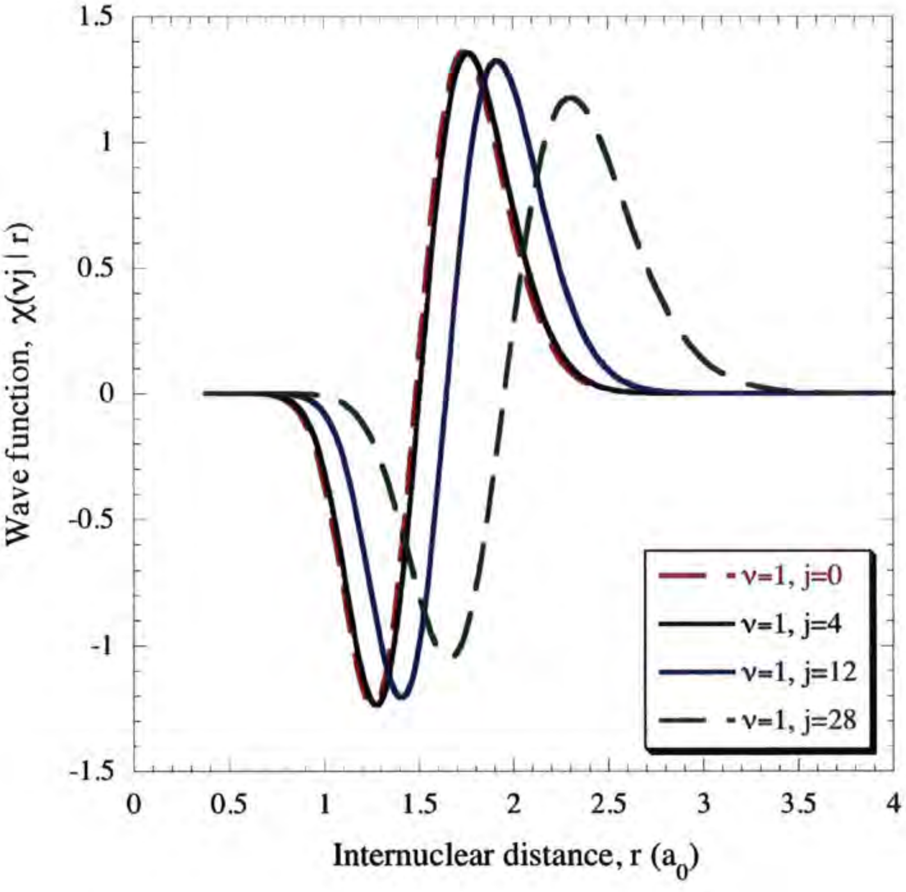

Figure 4.4: A comparison of results obtained for the H_2 wave functions $\chi(\nu j|r)$ for $\nu = 1$ and various j. The interaction potential of Mielke *et al.* [39] was used in these calculations.

where P_λ is a Legendre polynomial. The numerical integration is performed using the Gauss–Legendre integration method [45].

In principle the sum in equation (2.67) is infinite; in practice we truncate the series to a fixed number of terms. This is reasonable because as λ increases the magnitude of $v_\lambda(r, R)$ decreases rapidly. This is illustrated in Figure 4.5 where we see a rapid decrease in the magnitude of $v_\lambda(r, R)$ as λ increases. For larger values of R the difference in magnitudes between the $v_\lambda(r, R)$ terms, for different λ, can be several orders of magnitude. The number of terms retained is determined by performing cross section calculations for a fixed number of terms. Higher order terms are then added until suitable convergence is found. In our calculations the convergence criterion was to 4 significant figures within the cross sections.

For calculations presented in this thesis:

- Terms with $0 \leq \lambda \leq 6$ were retained for the H_2 calculations.
- Terms with $0 \leq \lambda \leq 6$ were retained for the HD calculations. Note: HD contains odd values of λ in its potential expansion due to the asymmetric position of its centre of mass.

4.3 Calculating the $y_\lambda(\nu j, \nu' j' | R)$ integrals

The rovibrational eigenfunctions $\chi(r)/r$ and the potential expansion coefficients $v_\lambda(r, R)$ are required to calculate the integrals

$$y_\lambda(\nu j, \nu' j' | R) = \int_0^\infty \chi^*(\nu j | r) v_\lambda(r, R) \chi(\nu' j' | r) \, \mathrm{d}r \, . \tag{4.8}$$

The integrals were calculated numerically using a form of Romberg integration [45]. The results were verified through agreement with independent integration routines. The $y_\lambda(\nu j, \nu' j' | R)$ integrals are discussed in more detail for H_2 and HD in the results Sections 5.1 and 6.1 respectively.

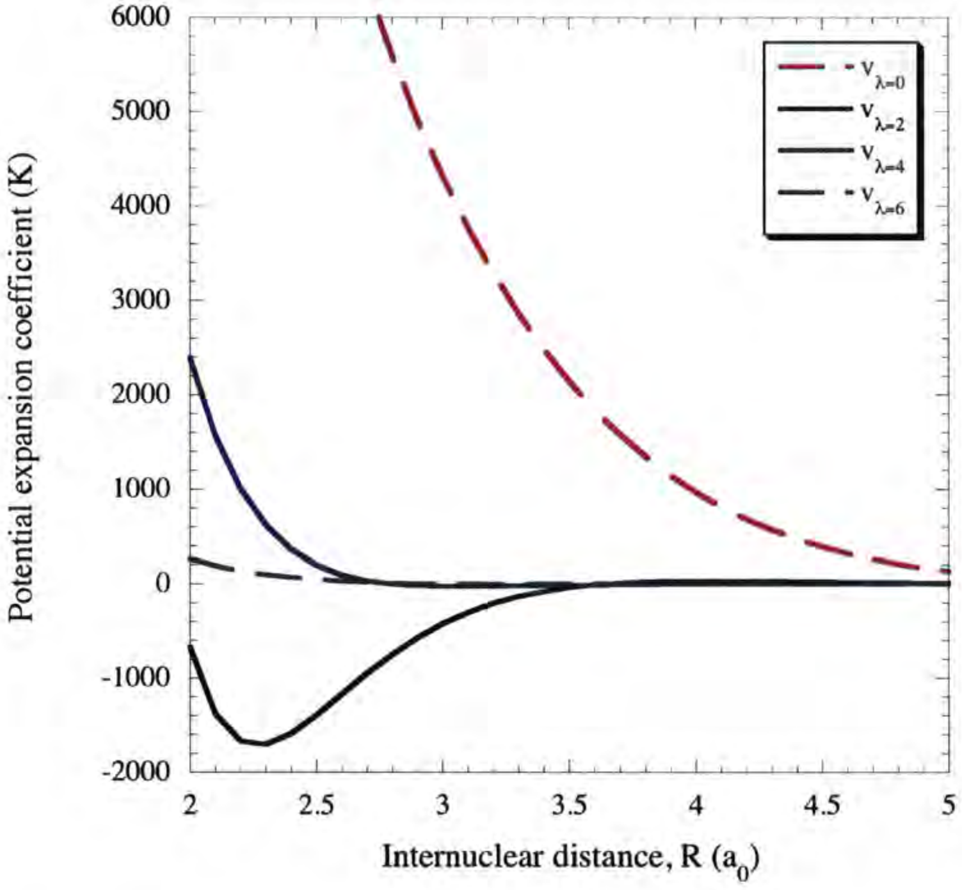

Figure 4.5: A comparison of $v_\lambda(r, R)$ where $0 \leq \lambda \leq 6$ for H_2 . Note $r = 1.4012a_0$, where a_0 is the Bohr radius.The interaction potential of Mielke *et al.* [39] was used in these calculations.

4.4 Cross sections

The cross sections are calculated by solving the coupled–channel equations for the SF frame, equation (2.77), or the BF frame, equation (2.79). Both methods are equivalent and identical cross sections are obtained (assuming no further approximations are made). Both sets of equations share the following properties:

1. Both are sets of ordinary differential equations which are linear in the functions of the radial co-ordinates, $F(R)$ or $G(R)$[1].
2. Both involve second order derivatives with respect to R.
3. Both are 'coupled' through the matrix elements on the right hand side of the equations.

There are several computational packages available for specifically solving problems of this nature. Examples include MOLCOL [46], MOLSCAT [47], and HIBRIDON [48]. The calculations presented in this thesis were performed using MOLCOL.

4.4.1 MOLCOL

MOLCOL [46] is a FORTRAN program that enables cross sections to be calculated for collisions between two systems of arbitrary angular momentum. It uses the quantal coupled channel method. Previous calculations have been performed for the H+H_2 system using MOLCOL [15, 18].

Numerical method

MOLCOL solves the BF coupled–channel equations (2.79). The equations are solved numerically, subject to the inner and outer boundary conditions. The inner boundary condition is applied at point $R_{\rm in}$, which is sufficiently

---

[1] $F(R)$ and $G(R)$ correspond to matrices containing the solutions for transitions from all available initial states to all final states, for given values of J and p, at a fixed R. The elements of matrices $F(R)$ and $G(R)$ are represented by $F^{\nu' j' l'}(\nu j l p J|R)$ and $G^{\nu' j' \Omega'}(\nu j \Omega p J|R)$ respectively.

far into the classically forbidden region that $V(R,\theta') \gg E$, where E is the barycentric collision energy relative to the ground states of A and BC. At this point $G(R_{\text{in}}) = 0$. The coupled equations are propagated from R_{in} to a point R_{out} where the potential is vanishingly small compared to the barycentric collision energy relative to all internal states of A + BC, E_{all} (i.e. $V(R,\theta') \ll E_{\text{all}}$). At this point a transformation to the SF frame is made using a unitary transformation [49]. The SF solutions are matched to spherical Bessel functions of the first and second kinds, and the **T**–matrix is derived. The cross sections are derived from the **T**–matrix (see Section 2.4).

Many routines exist that can perform the numerical propagation for the coupled–channel equations (2.79). The routines used for the calculations presented within this thesis were based on the log–derivative algorithm of Johnson [50]. This method was chosen as it is the most stable and quickest of the available routines in MOLCOL. Stabilisation issues can arise when $G(R)$ is propagated through the classically forbidden region. This is due to the exponential growth of the individual solutions within the classically forbidden region. In most cases one solution can grow more rapidly than others, dominating each column in the matrix, which destroys the linear independence of the solutions. To prevent this from happening stabilisation routines are used. However, in the log–derivative method the log–derivative $X(R)$,

$$X(R) = \frac{\mathrm{d}}{\mathrm{dR}} \ln G(R) = \frac{G'(R)}{G(R)}, \tag{4.9}$$

where $G'(R)$ is the first derivative of $G(R)$ with respect to R, is propagated from the inner to outer boundary conditions. This eliminates the stability problems when starting the propagation deep inside the classically forbidden region.

Propagation parameters

MOLCOL requires several input parameters to use the propagation routines. The parameters were varied until convergence of the computed cross sections, to four significant figures, had been obtained.

- **RDB** – the inner boundary condition point, R_{in}, which must be sufficiently within the classically forbidden region (short-range repulsive region of interaction potential) that $G(R) = 0$. This is the point at which $X(R)$ is propagated outwards to the asymptotic region.

- **RFN** – the outer boundary condition point, R_{out}, at which the interaction potential has become negligible and the outer boundary condition may be applied. This is the point where $X(R)$ is propagated to.

- **FPT** – the number of integration points per arch of the oscillatory arch of the scattering wave function. A value of 10 was found to be satisfactory.

- **RMIN** – the value of R at which the minimum of the most attractive potential energy curve occurs (taken to be $y_{\lambda=0}(\nu = 0\, j = 0, \nu' = 0\, j' = 0|R)$).

- **DELTAE** – the absolute value of this minimum, in atomic units.

The variables FPT, RMIN, and DELTAE are used to determine the step size for the numerical propagator routines.

Input

The basis set used to represent the system A + BC is inputted into MOLCOL by entering several variables. These are the vibrational and rotational quantum numbers, for each level, and their corresponding bound-state energy level value, with respect to the $\nu = 0$, $j = 0$, in kelvin. When determining the size of the basis set one wishes it to be as complete in terms of ν and j as possible. However when performing full coupled–channel equations the number of equations, or coupled-channels, can grow rapidly [21]. This is because each vibrational manifold, v, contains a certain number, j_v, of bound rotational states. For coupled–channel calculations the number of coupled–channels is given by

$$\sum_{j=0}^{j_v}(j+1) = (j_v+1)(j_v+2)/2 \, ,$$

for one value p, and

$$\sum_{j=0}^{j_v} j = j_v(j_v+1)/2 \ ,$$

for the other value of p. For $j_v = 16$ there are 153 and 136 coupled equations, respectively, for the vibrational manifold, v. In our calculations we must consider several manifolds at once (all $\nu \leq 6$). Also, in our systems the energy levels of the vibrational manifolds overlap as states with small ν and large j have similar energies to those with large ν and small j. When performing coupled–channel calculations one tries to include all states below a given energy in the basis set for completeness and reliability of the results. Hence, large j_v are necessary for the lower manifolds. As the number of coupled channels depends quadratically on j_v, and with the coupling between vibrational manifolds, the problem can quickly become computationally demanding or impractical. It is only for the lightest molecules H_2 and HD that the full coupled–channels calculations are possible, as in our case. The size of the basis sets used for calculations in this thesis were considerably larger than those used in previous calculations. The method of determining the size of the basis sets is discussed in Sections 5.2 and 6.2.

MOLCOL also requires the values for the $y_\lambda(\nu 0, \nu' 0|R)$ integrals. MOLCOL, in its original form, does not have the facilities to handle j–dependent y_λ integrals.

Cross section parameters

MOLCOL calculates the partial cross sections for each value of the total angular momentum, J. The partial cross sections are then summed over J to give the total cross section. The highest value of J, for which the partial cross sections are calculated at, is determined by the parameters:

- **FJDB** – the initial value of of J. For our calculations, FJDB = 0.
- **FJFN** – the final value of J. This is set sufficiently large to ensure prior convergence of the partial wave series. For our calculations, FJFN = 500.

- **OPCMN** – this parameter determines the convergence of the partial wave series. Partial cross sections are calculated until the probabilities for inelastic scattering transitions become less than OPCMN. For our calculations, OPCMN $= 10^{-8}$.

These parameters were chosen for convergence to four significant figures in the total cross sections.

Cross section tests

To ensure the calculated cross sections were reliable, several tests were performed for a variety of collision energies:

1. Cross sections were calculated using an alternative numerical propagation routine. In our case, alternative routines based on the algorithm of de Vogelaere [51] were used.
2. Cross sections were calculated independently using MOLSCAT [47]. Independent numerical methods are used by MOLSCAT too.
3. Cross sections were compared to previous results, using the same basis set size, obtained for the SHO model [15].

For all tests excellent agreement was found; typically to four significant figures.

4.4.2 Modifying MOLCOL

As mentioned previously, MOLCOL in its present form cannot handle j–dependent y_λ integrals. This means it can only perform calculations for the SHO, Morse oscillator and ENCO models. Extensive modifications were made to the program to allow j–dependent y_λ integrals to be used. The modified MOLCOL is capable of performing calculations for the 'exact oscillator' model. To ensure the modified program was functioning correctly, computed cross sections were compared with those determined with MOLSCAT.

MOLSCAT can handle j–dependent y_λ integrals in its original form. Excellent agreement between the programs was found; typically to four significant figures. However, MOLCOL was found to be moderately quicker for most calculations.

4.5 Determination of the rate coefficients

The rate coefficients are determined from the total cross sections using (see Section 2.5 for more details) the following equation

$$\langle \sigma v \rangle = \left(\frac{8 k_\mathrm{B} T}{\pi \mu} \right)^{\frac{1}{2}} \int_0^\infty x \sigma(x) \mathrm{e}^{-x} \, \mathrm{d}x \ . \tag{4.10}$$

When calculating the cross sections, the grid of collision energies (i.e. the collision energies at which cross sections were calculated) must have sufficiently high resolution to pick up energy–dependent features within the cross section. This is particularly important near threshold where the cross sections can vary rapidly. Considerable effort was made to ensure a fine enough collision energy grid was used for our calculations. This can be a considerably difficult task due to the large number of transitions and the extra computational resources that are required for extra collision energies.

The rate coefficients were calculated numerically on a grid of temperatures. Specific calculation details are given in Sections 5.4 and 6.4. A simple quadrature method (the trapezium rule) was used with cubic spline interpolation, to determine cross section values between energy grid points, when evaluating the rate coefficient integrals.

Part III

Calculations

Chapter 5

Calculations for $H+H_2$

In this chapter the results of the scattering calculations for $H+H_2$ are presented. We begin with an analysis of the potential expansion coefficients for the $H+H_2$ system. Next, we discuss the basis sets used to describe the system in the scattering calculations. Then the cross sections as a function of the barycentric collision energy, $\bar{E}$, are presented. Finally, the corresponding rate coefficients are presented as function of kinetic temperature, T.

Results from this chapter have been presented in [52–54].

5.1 Potential expansion coefficients

When performing the scattering calculations it is necessary to express the interaction potential as an expansion in terms of Legendre polynomials

$$V(\mathbf{r},\mathbf{R}) = \sum_{\lambda} v_{\lambda}(r,R)P_{\lambda}(\hat{\mathbf{r}}\cdot\hat{\mathbf{R}}), \tag{5.1}$$

where $\mathbf{r}$ is the intramolecular vector, which is taken to coincide with the internuclear axis, $\mathbf{R}$ is the vector associated with distance between the atom and the centre of mass of the molecule, $P_{\lambda}(\hat{\mathbf{r}}\cdot\hat{\mathbf{R}})$ is a Legendre polynomial of order λ, and $v_{\lambda}(r,R)$ is a potential expansion coefficient. In the case of a homonuclear molecule, such as H_2, only even values of λ contribute to the expansion in equation (5.1); symmetry considerations dictate that the terms with odd values of λ vanish identically.

The potential expansion coefficients, $v_\lambda(r, R)$, are used to determine the integrals

$$y_\lambda(\nu j, \nu' j'|R) = \int_0^\infty \chi^*(\nu j|r)v_\lambda(r, R)\chi(\nu' j'|r), \tag{5.2}$$

where $\chi(r)/r$ are the rovibrational eigenfunctions of the molecule. The numerical calculation of the rovibrational eigenfunctions was discussed earlier in Chapter 4. The $y_\lambda(\nu j, \nu' j'|R)$ are calculated numerically for later use by the scattering program.

The integrals, $y_\lambda(\nu j, \nu' j'|R)$, were calculated using the interaction potential of Mielke *et al.* [39] and Boothroyd *et al.* [38], for $0 \leq \lambda \leq 6$ and $1.0 \leq R \leq 25.0\ a_0$; the terms with $\lambda = 0, 2, 4, 6$ were sufficient to obtain convergence of the potential expansion. The magnitude of the integrals rapidly decreases as λ increases. This was confirmed by inspection of the coefficients and by performing some cross section calculations with higher order terms included. In terms of the cross sections, 'convergence' was to 4 significant figures.

Figure 5.1 shows $y_\lambda(\nu j, \nu' j'|R)$ for $\lambda = 0, 2$ using the interaction potential of Mielke *et al.* [39] and the 'exact oscillator' functions. The full black line represents $y_{\lambda=0}(00, 00|R)$, which controls elastic scattering. It is considerably larger in magnitude than the $y_{\lambda=2}(\nu 0, \nu' 0|R)$ terms also shown in Figure 5.1. This trend agrees with the previous observation that the $y_\lambda(\nu j, \nu' j'|R)$ rapidly decrease in magnitude as λ increases.

The integrals, $y_\lambda(\nu j, \nu' j'|R)$, for the interaction potential of Mielke *et al.* [39] and the SHO functions are shown in Figure 5.2. In comparison to the case for the exact oscillator, shown in Figure 5.1, we see that the $y_{\lambda=0}(00, 00|R)$ is approximately the same in magnitude for the SHO case. However, the $y_{\lambda=2}(\nu 0, \nu' 0|R)$ for the SHO case are considerably smaller in magnitude than the corresponding results for the 'exact oscillator' case.

We note that the $y_{\lambda=2}(\nu 0, \nu' 0|R)$ shown in Figures 5.1 and 5.2 contribute to transitions involving $\Delta J = 2$. The cases where $\nu \neq \nu'$ are associated with vibrationally inelastic transitions and the $y_{\lambda=2}(\nu 0, \nu' 0|R)$ are much larger in magnitude for the 'exact oscillator' case than they are for the SHO case.

The integrals $y_\lambda(\nu j, \nu' j'|R)$ also were determined using the interaction potential of Boothroyd *et al.* [38] for both the 'exact oscillator' and SHO functions. The same trends were observed between the two vibrational representations

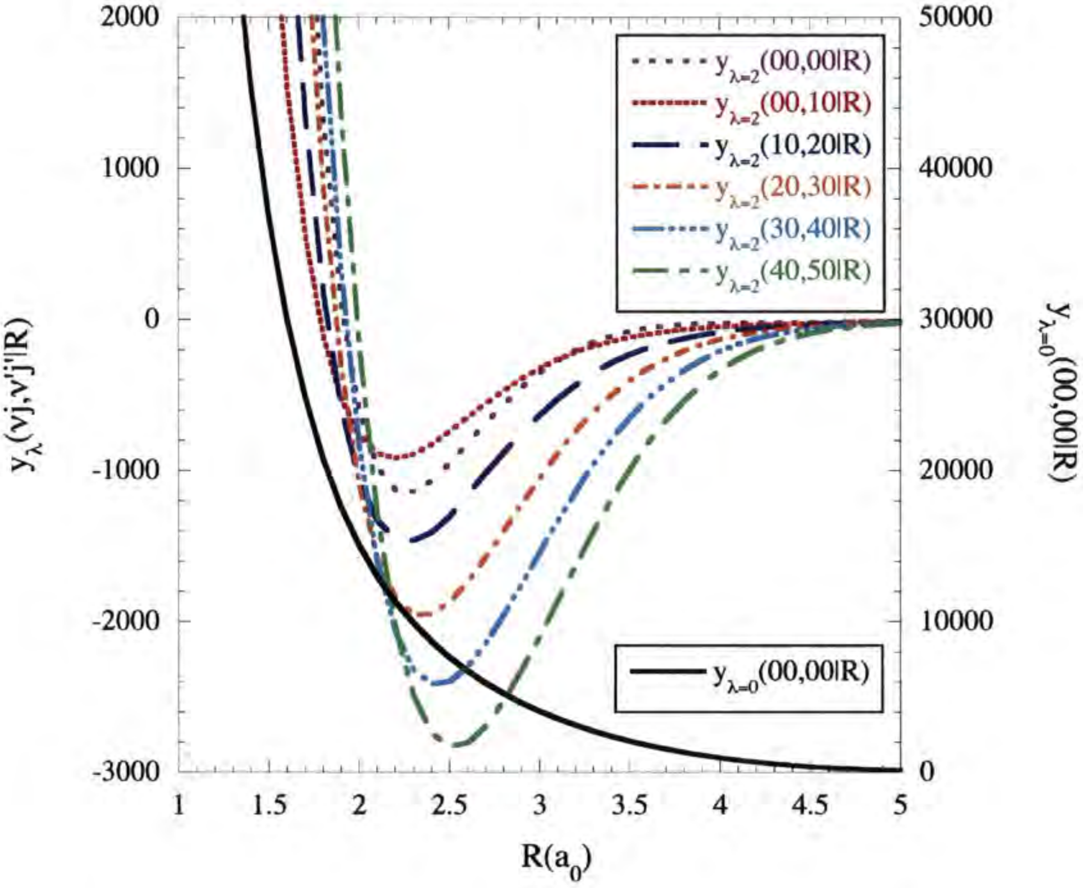

Figure 5.1: The variation with R of $y_\lambda(\nu 0, \nu' 0|R)$, in units of kelvin, for $\lambda = 2$ and selected pairs of values of ν, ν'. The full black line represents $y_{\lambda=0}(00, 00|R)$, which controls elastic scattering. The results presented here refer to the potential of Mielke *et al.* [39] and the exact oscillator functions. Note that the magnitudes of terms ($\nu \neq \nu'$), which control vibrationally inelastic scattering, increase with increasing ν, ν'.

for the interaction potentials of Boothroyd *et al.* [38] and Mielke *et al.* [39]. The magnitudes of the $y_\lambda(\nu j, \nu' j'|R)$ were comparable between the two different interaction potentials.

5.2 Basis set

Molecular hydrogen exists in two forms, ortho–H_2 and para–H_2, and we must take this into account when selecting a suitable basis set. The para–H_2 basis set contains rovibrational energy levels with even values of j, and the ortho–H_2 basis set contains rovibrational energy levels with odd values of j.

At high collision energies (~5000 K) the potential barrier to reactive scattering may be overcome by the incident H atom and H–atom exchange may occur. As a consequence the hydrogen molecule may undergo a transition from an ortho–state to a para–state and vice versa. The product H_2 may be formed in rovibrationally excited states in which case the reactive scattering process contributes to the total excitation probability and the corresponding cross sections. In our calculations the reactive scattering processes have been neglected and the incident H–atom retains its identity throughout the collision. As a consequence the results presented in this thesis provide only a lower limit to the rovibrational excitation probabilities, and their corresponding cross sections, at collision energies $E \gtrsim 5000$ K. When hydrogen atom exchange is neglected the calculations for para– and ortho–H_2 can be performed completely independently.

The incident H–atom is assumed to be structureless and therefore cannot undergo internal excitation. The electronic excitation of the incident H–atom is also neglected. We may justify this assumption in two ways. Firstly, the first excited electronic state of atomic hydrogen requires requires an excitation energy of $\sim 118,500$ K (~ 10.2 eV), from the ground state, which is considerably larger than even the largest collision energy calculations were performed for. Secondly, the transfer of energy from the heavy nuclei to the relatively light electrons is an inefficient process.

The electronic excitation within the hydrogen molecule is also neglected. This may be justified, again, by the inefficient transfer of energy from the

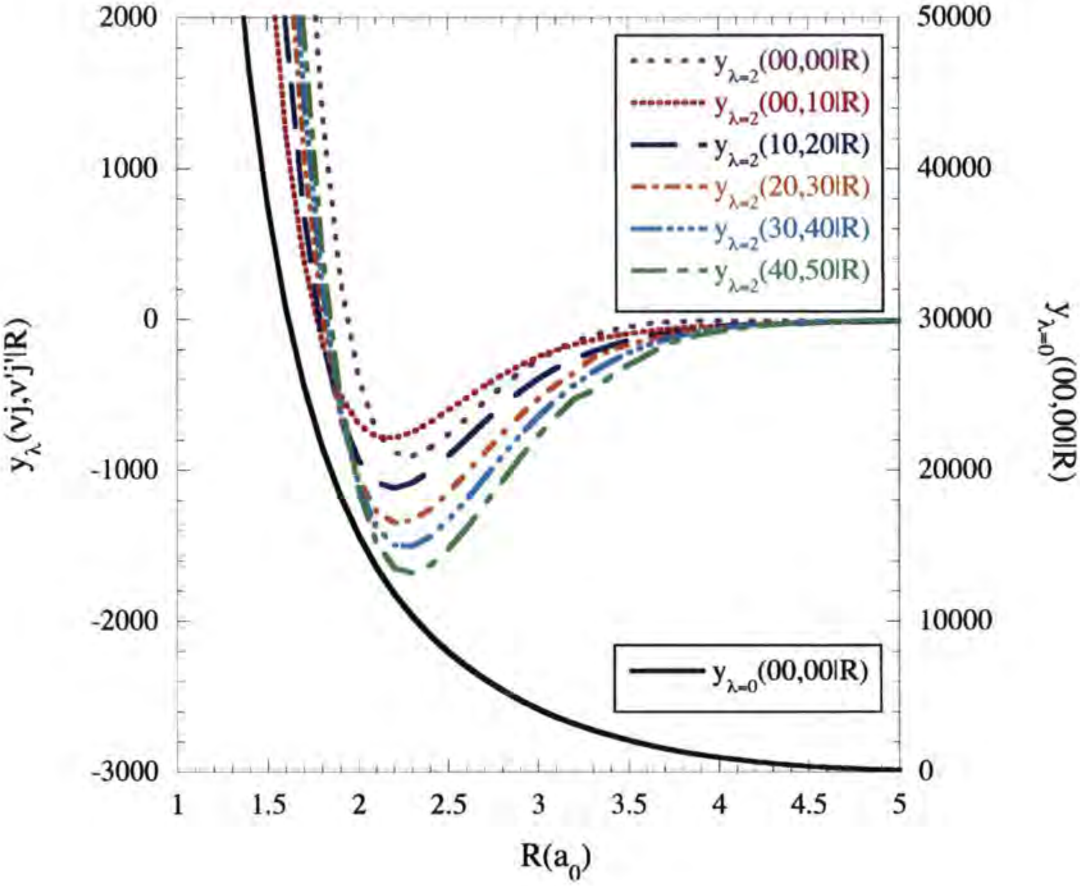

Figure 5.2: The variation with R of $y_\lambda(\nu 0, \nu' 0|R)$, in units of kelvin, for $\lambda = 2$ and selected pairs of values of ν, ν'. The full black line represents the $y_{\lambda=0}(00, 00|R)$, which controls elastic scattering. The results presented here refer to the potential of Mielke *et al.* [39] and the simple harmonic oscillator functions. Note that terms ($\nu \neq \nu'$), which control vibrationally inelastic scattering, are considerably smaller in magnitude than the corresponding 'exact oscillator' results in Figure 5.1.

heavy nuclei to the light electrons. Also, the energy required to achieve the electronically excited states is typically much larger than the incident H–atom collision energies used in our calculations.

The basis set used in our calculations consisted of one energy level, corresponding to the ground state of the structureless atom, and the rovibrational energy levels of para–H_2 or ortho–H_2 (depending on which form of H_2 is being considered). The rovibrational energy levels of the hydrogen molecule used in our calculations were taken from the paper by Dabrowski [55] who calculated a total of 318 rovibrational energies with $0 \leq \nu \leq 14$ and $0 \leq j \leq 29$, where ν is the vibrational quantum number and j is the rotational quantum number, from experimental observations and theoretical data. For para–H_2 the basis set levels used corresponded to the even valued j rovibrational energy levels from [55]. The basis set levels used for ortho–H_2 were the odd valued j rovibrational energy levels from [55]

5.2.1 Determining the size of the basis set

When performing the cross section calculations we truncate the size of the basis set because use of a 'complete' basis set, consisting of all the rovibrational energy levels of ortho– or para–H_2, is computationally impractical. Our approach in determining the size of the basis set was empirical: the basis set was extended upwards in the energy of the H_2 rovibrational levels until satisfactory convergence was obtained. Owing to the strong coupling between the vibrational levels (see Figures 5.1 and 5.2), it was necessary to include energy levels which were much higher than the relative collision energy of the atom and the molecule. This is illustrated in Figures 5.3 and 5.4. The results are presented as a function of basis set size for para–H_2, with rotational states $j = 0, 2, 4, 6$ being included in each vibrational manifold, up to the specified value of the vibrational quantum number, ν. We see that rovibrational levels upto $\nu = 6$ are required to achieve a satisfactory convergence for the $\nu = 0,\ j = 2 \rightarrow \nu' = 0,\ j' = 0$ transition[1]. Similar results were found for the case of ortho–H_2 .

---

[1] Transitions involving higher initial rovibrational states may require a basis set that includes rovibrational levels with $\nu > 6$ to achieve satisfactory convergence.

In summary, for the calculations presented in this thesis:

- the first 54 rovibrational levels of para–H_2 (up to and including $\nu = 6$, $j = 4$) were included for calculations involving para–H_2 . They are listed in Appendix A.
- the first 54 rovibrational levels of ortho–H_2 (up to and including $\nu = 0$, $j = 23$) were included for calculations involving ortho–H_2 . They are listed in Appendix B.

5.3 Cross sections

With a basis set size of 54 levels there will be data produced for 2916 transitions. Therefore only a representative subset of our results can be presented here although the general conclusions drawn are believed to apply to most transitions. Checks have been made by sampling different transitions to observe the general conclusions still hold.

De–excitation cross sections are presented within this thesis. The principle of detailed balance (see equation (2.87)) may be used to obtain the corresponding excitation cross sections. The complete set of cross sections, as a function of barycentric collision energy, is available from http://ccp7.dur.ac.uk.

The cross section results are presented for both the para–H_2 and ortho–H_2 cases.

5.3.1 Cross sections for H+para–H_2

Cross sections for H+para–H_2 were calculated for 130 barycentric collision energies ranging from 560 K to 60000 K. When selecting specific collision energies care was taken to choose values sufficiently close to threshold energies (as the cross sections vary rapidly near threshold). The collision energies chosen are believed to give good coverage for low-energy and high-energy structure in the cross sections.

Calculations were performed using the interaction potentials of Mielke *et al.* [39] and Boothroyd *et al.* [38]. Cross sections were obtained for SHO, Morse

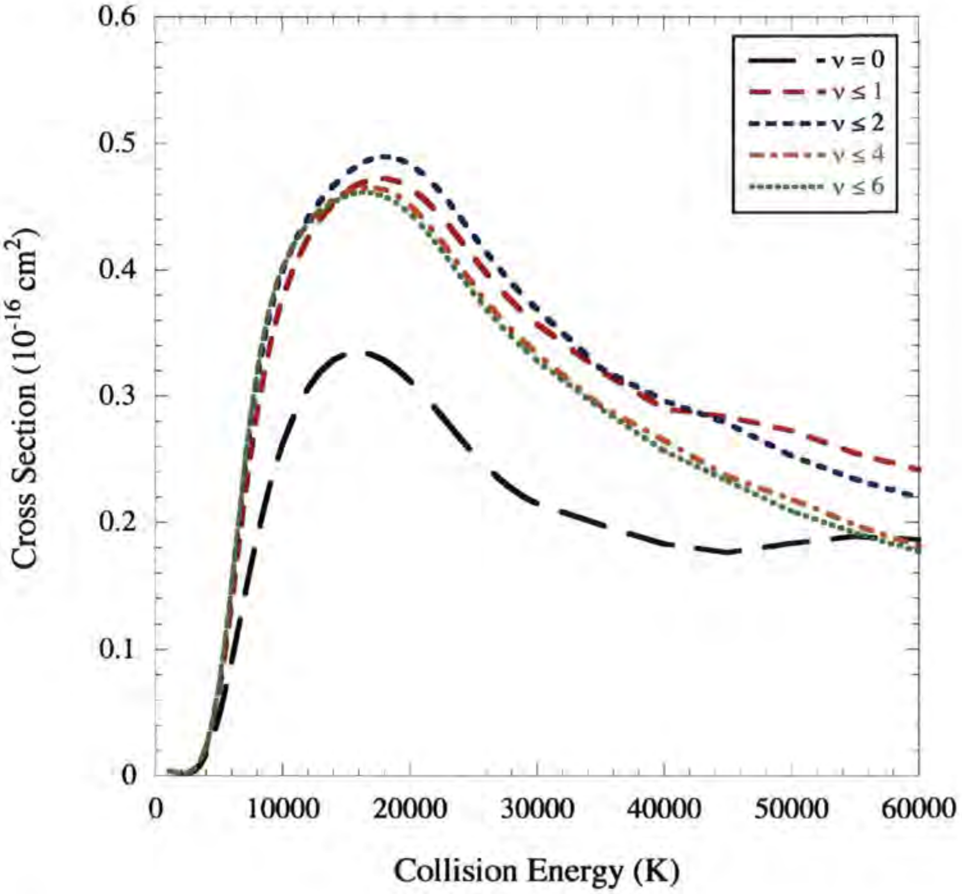

Figure 5.3: Cross section for the $\nu = 0,\ j = 2 \rightarrow \nu' = 0,\ j' = 0$ transition, calculated using SHO vibrational eigenfunctions. The results are given as a function of basis set size, with rotational states $j = 0, 2, 4, 6$ being included in each vibrational manifold, up to the specified value of the vibrational quantum number, ν.

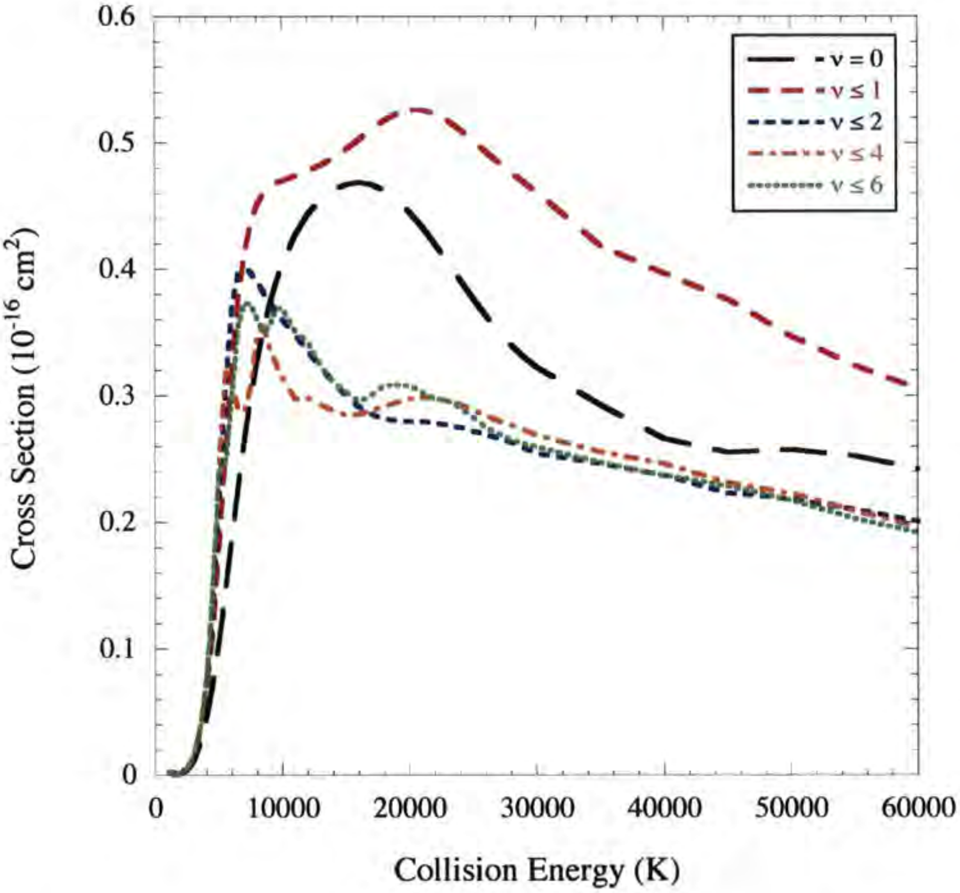

Figure 5.4: Cross section for the $\nu = 0,\ j = 2 \rightarrow \nu' = 0,\ j' = 0$ transition, calculated using the ENCO vibrational eigenfunctions. The results are given as a function of basis set size, with rotational states $j = 0, 2, 4, 6$ being included in each vibrational manifold, up to the specified value of the vibrational quantum number, ν.

oscillator, ENCO[2], and 'exact oscillator' vibrational representations of the H_2 molecule. The greatest discrepancies were between the SHO and 'exact oscillator' calculations; the Morse oscillator and ENCO results were closer to the 'exact oscillator' results. Discussion of the results is restricted to the SHO, ENCO, and 'exact oscillator' representations within this thesis.

Comparison of cross sections between different representations of the vibrational motion of the molecule for H+para–H_2

First, we compare the results obtained using different representations of the vibrational motion of the molecule. Figures 5.3 and 5.4 show the cross section plotted for the vibrationally elastic transition $\nu = 0,\ j = 2 \rightarrow \nu' = 0,\ j' = 0$, as a function of the barycentric collision energy; the cross section was calculated using both the SHO and the ENCO rovibrational eigenfunctions and the potential of Mielke *et al.* [39]. The results are shown for increasing vibrational basis set size, including the rotational states $j = 0, 2, 4, 6$ in each vibrational manifold. It may be seen that convergence with respect to the vibrational quantum number, ν, is slow, particularly when the ENCO functions are used: states up to at least $\nu = 6$ are required for complete convergence. Furthermore, there are substantial differences between the cross sections calculated using the SHO approximation and the ENCO vibrational functions, even in this case of a vibrationally elastic transition. The cross section increases more rapidly from threshold when the ENCO rather than the SHO vibrational functions are used, as was demonstrated earlier by Forrey *et al.* [16], who employed previous potentials.

Figures 5.5 and 5.6 show the analogous results for the first rovibrationally inelastic transition $\nu = 1,\ j = 2 \rightarrow \nu' = 0,\ j' = 0$. There is considerable variation in the cross section as levels with higher vibrational quantum numbers are added. Once again, the rotational states $j = 0, 2, 4, 6$ were included in each vibrational manifold. The slow convergence of the cross sections, with respect to the vibrational basis, is evident. When vibrational states $\nu > 1$ are included in the basis, the cross section calculated using the ENCO repre-

---

[2] ENCO refers to the exact oscillator rovibrational eigenfunctions with the centrifugal term neglected, see section 4.1.

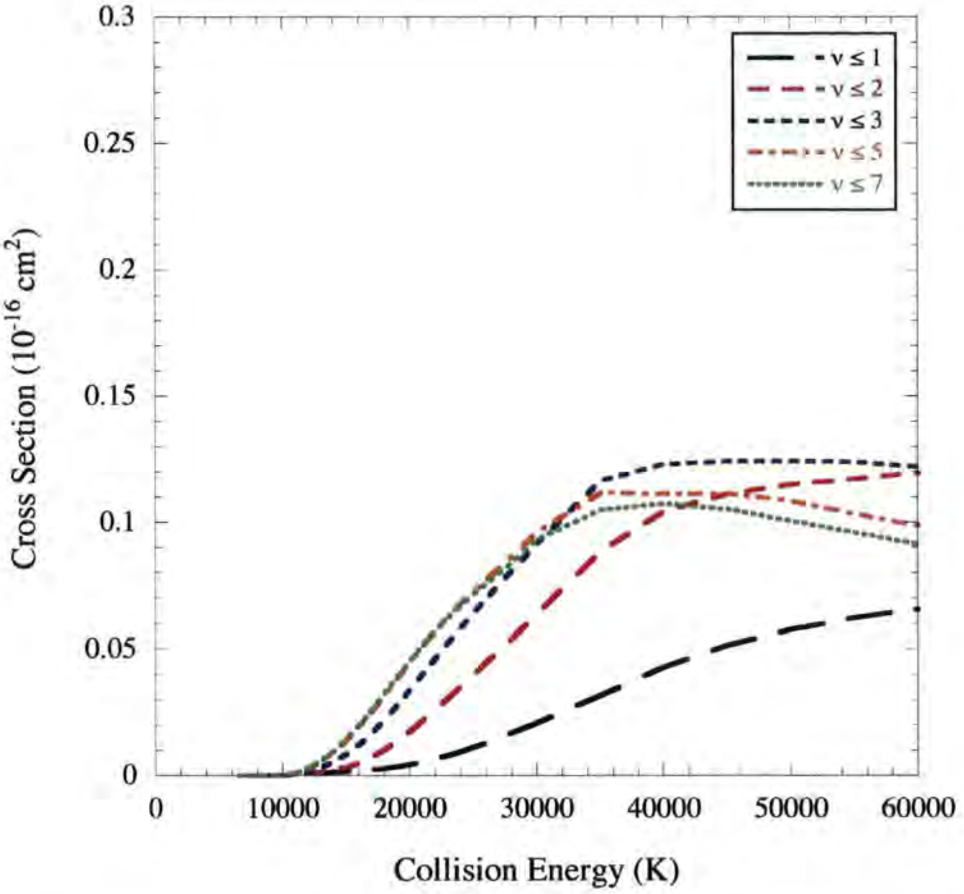

Figure 5.5: Cross section for the $\nu = 1,\ j = 2 \rightarrow \nu' = 0,\ j' = 0$ transition, calculated using SHO vibrational eigenfunctions. The results are given as a function of basis set size, with rotational states $j = 0, 2, 4, 6$ being included in each vibrational manifold, up to the specified value of the vibrational quantum number, ν. The ranges of the axes are identical to those of Figure 5.6 in order to facilitate the comparison with this figure.

sentation of the vibrational eigenfunctions increases much more rapidly from threshold (at 6472 K) than is predicted by the SHO approximation. The sensitivity of the cross section to the inclusion of high vibrational levels in the basis set relates to the magnitudes of the corresponding coupling terms, which are plotted in Figure 5.1; these terms are smaller in magnitude when the SHO approximation is used.

Calculations were performed for the potential of Mielke *et al.* [39] using the 'exact oscillator' vibrational functions. Figure 5.7 shows the case for the $\nu = 0,\ j = 2 \rightarrow \nu' = 0,\ j' = 0$ transition. Substantially more structure is observed in the data for the 'exact oscillator' case, at collision energies 10000 K – 20000 K, than for cross sections obtained using the SHO functions. The rate of increase from threshold is faster for the 'exact oscillator' case than for the SHO case, although the cross section peaks at a lower value when using the 'exact oscillator' functions.

The cross section for the $\nu = 1,\ j = 2 \rightarrow \nu' = 0,\ j' = 0$ transition is shown in Figure 5.8 using the 'exact oscillator' rovibrational eigenfunctions. There is more structure contained in the cross section, using the 'exact oscillator' functions, than for those obtained using the ENCO representation. A faster increase in the cross section from threshold is obtained using the 'exact oscillator' functions than those obtained using the SHO and ENCO representations. The logarithmic plot in Figure 5.8 clearly shows the large discrepancies in the cross section near threshold between the SHO and 'exact oscillator' representations for the vibrationally inelastic transition.

Comparison of cross sections between different representations of the interaction potential for H+para–H$_2$

We proceed now to a comparison of the results obtained using the ENCO vibrational eigenfunctions but using different representations of the interaction potential [39], [38]. Figure 5.9 shows a comparison of converged calculations of the cross section for the $\nu = 0,\ j = 2 \rightarrow \nu' = 0,\ j' = 0$ pure rotational transition, obtained using these two potentials. It may be seen that, over the extended range of collision energies in this figure, the results are generally in good agreement. In an earlier study [52], a similar comparison over

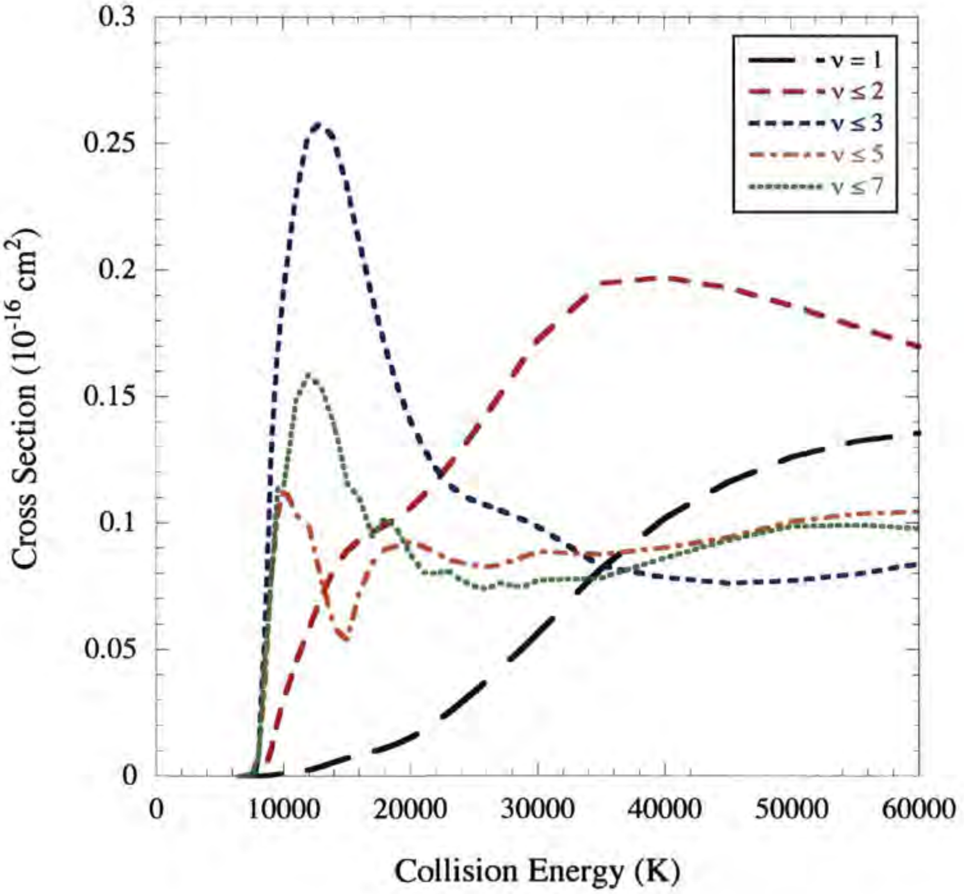

Figure 5.6: Cross section for the $\nu = 1$, $j = 2 \rightarrow \nu' = 0$, $j' = 0$ transition, calculated using the ENCO vibrational eigenfunctions. The results are given as a function of basis set size, with rotational states $j = 0, 2, 4, 6$ being included in each vibrational manifold, up to the specified value of the vibrational quantum number, ν.

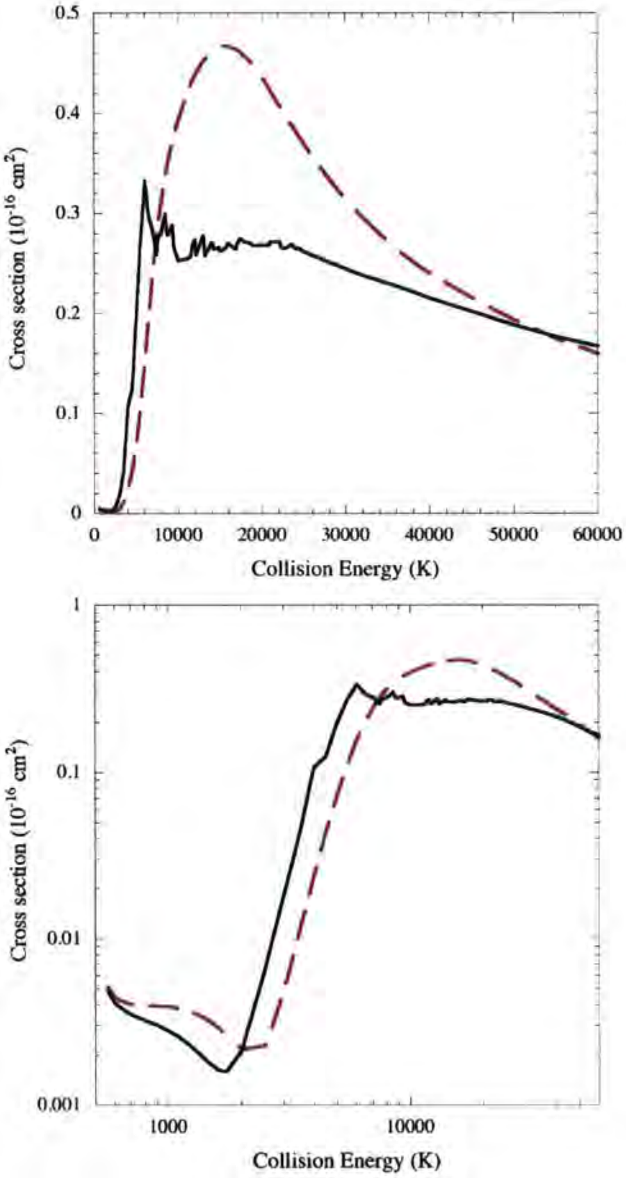

Figure 5.7: A comparison of converged results obtained for the $\nu = 0,\ j = 2 \rightarrow \nu' = 0,\ j' = 0$ transition using the SHO (broken curve) and 'exact oscillator' (full curve) models. The interaction potential of Mielke *et al.* [39] was used in these calculations and a basis set comprising all states of para–H$_2$ up to and including $\nu = 6, j = 4$.

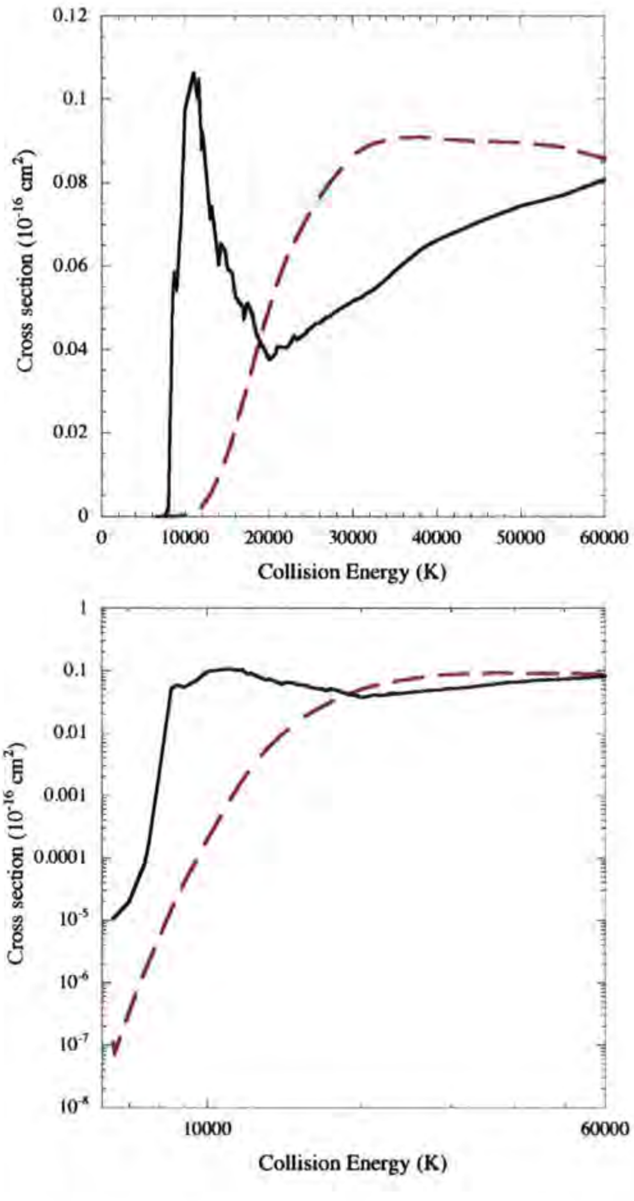

Figure 5.8: A comparison of converged results obtained for the $\nu = 1,\ j = 2 \rightarrow \nu' = 0,\ j' = 0$ transition using the SHO (broken curve) and 'exact oscillator' (full curve) models. The interaction potential of Mielke *et al.* [39] was used in these calculations and a basis set comprising all states of para–H$_2$ up to and including $\nu = 6, j = 4$.

a more restricted range of collision energies, $E \leq 10\ 000$ K, was made. As the threshold of the transition, at $E = 510$ K, is approached, significant differences between cross sections computed using the two potentials become apparent; they are just discernible in Figure 5.9.

For the $\nu = 1,\ j = 2 \rightarrow \nu' = 0,\ j' = 0$ rovibrationally inelastic transition, shown in Figure 5.10, there are substantial differences between results obtained using the two potentials, notably in the near-threshold region, where the cross section computed with the potential of Mielke *et al.* [39] increases less steeply. The structure which is seen in the energy dependence of the cross sections arises from the potential coupling (see right-hand side of equation (2.79)).

5.3.2 Cross sections for H+ortho–H_2

The results for the H+ortho–H_2 scattering calculations are presented in this section. The results follow similar trends to those found for H+para–H_2 in Section 5.3.1.

For the H+ortho–H_2 system calculations were performed for 130 barycentric collision energies ranging from 1000 K to 60000 K; the first inelastic scattering channel opens at 1015.2 K.

Comparison of cross sections between different representations of the vibrational motion of the molecule for H+ortho–H_2

In Figure 5.11 the cross section for the $\nu = 0,\ j = 3 \rightarrow \nu' = 0,\ j' = 1$ transition is plotted, as a function of barycentric collision energy, using the SHO (broken curve) and 'exact oscillator' (full curve) models representations. Again, as in the case for H+para–H_2 , the cross sections increase more rapidly from threshold when the 'exact oscillator', rather than the SHO, vibrational eigenfunctions are used.

Figure 5.12 shows the the cross section for the $\nu = 1,\ j = 3 \rightarrow \nu' = 0,\ j' = 1$ transition, plotted as a function of barycentric collision energy, using the SHO (broken curve) and 'exact oscillator' (full curve) representations. There are substantial differences between the 'exact oscillator' and SHO representa-

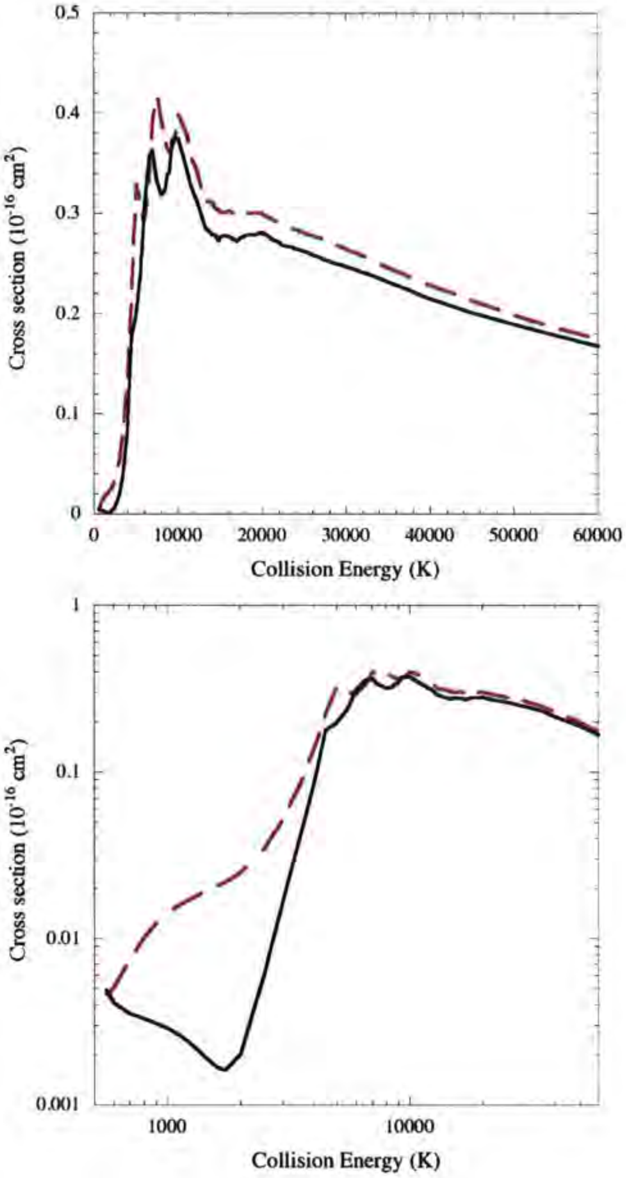

Figure 5.9: A comparison of converged results obtained for the $\nu = 0,\ j = 2 \rightarrow \nu' = 0,\ j' = 0$ transition using the potentials of Boothroyd *et al.* [38] (broken curve) and Mielke *et al.* [39] (full curve). The ENCO vibrational functions were employed in these calculations and a basis set comprising all states of para–H$_2$ up to and including $\nu = 6, j = 4$.

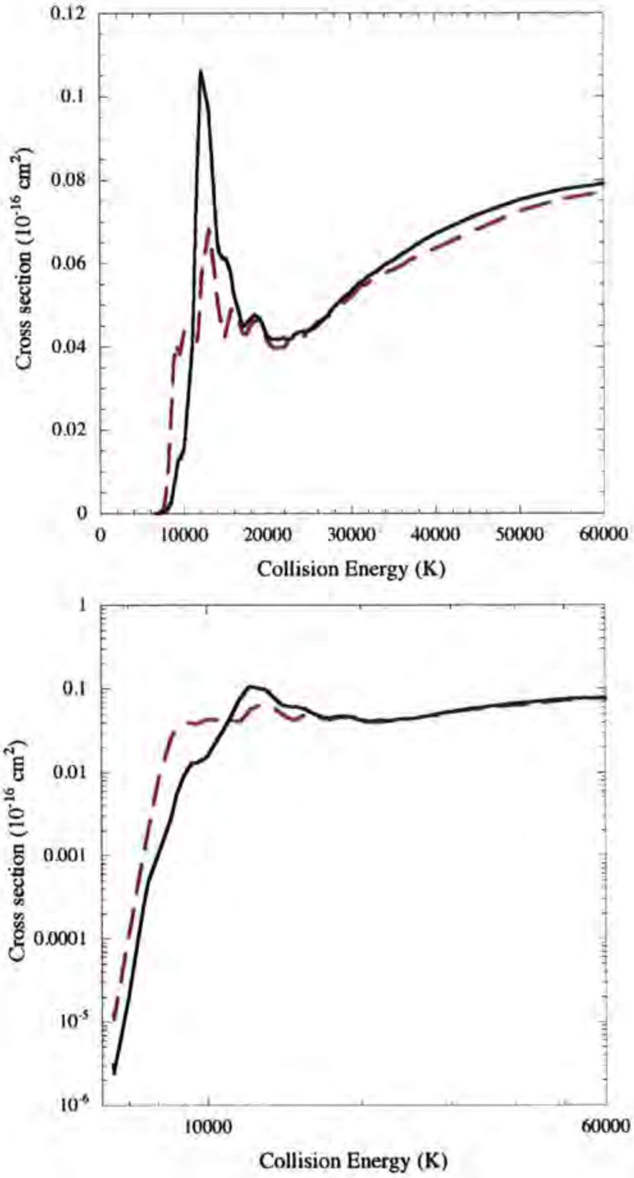

Figure 5.10: A comparison of converged results obtained for the $\nu = 1,\ j = 2 \rightarrow \nu' = 0,\ j' = 0$ transition using the potentials of Boothroyd *et al.* [38] (broken curve) and Mielke *et al.* [39] (full curve). The ENCO vibrational functions were employed in these calculations and a basis set comprising all states of para–H$_2$ up to and including $\nu = 6, j = 4$.

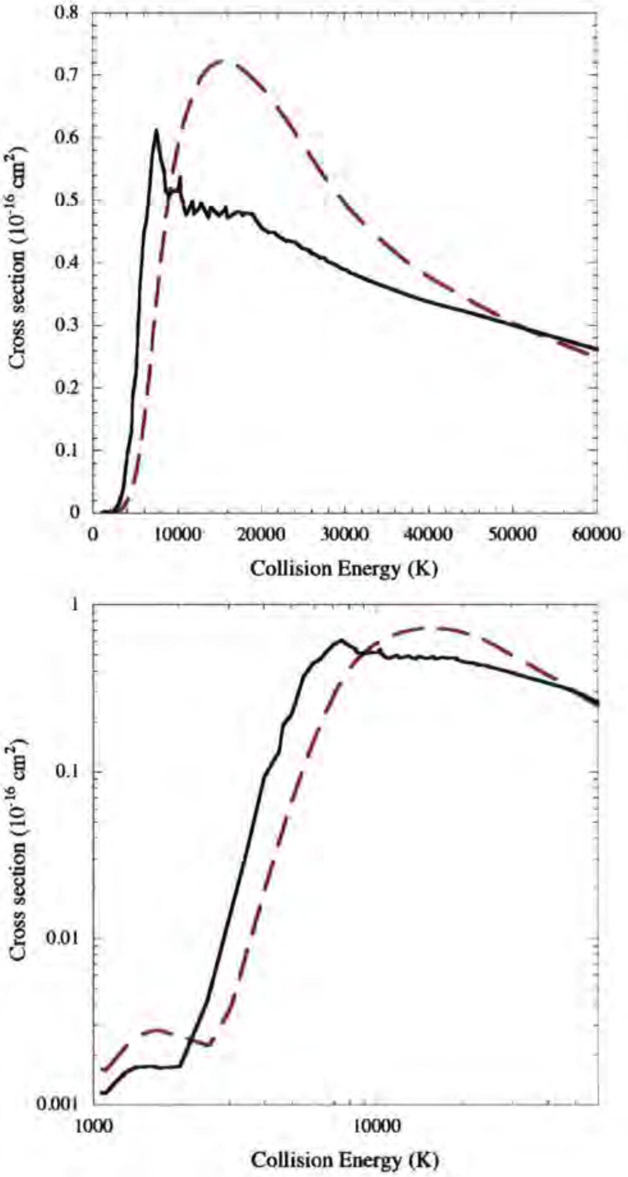

Figure 5.11: A comparison of results obtained for the $\nu = 0,\ j = 3 \rightarrow \nu' = 0,\ j' = 1$ transition using the SHO (broken curve) and 'exact oscillator' (full curve) models. The interaction potential of Mielke *et al.* [39] was used in these calculations and a basis set comprising all states of ortho–H$_2$ up to and including $\nu = 0, j = 23$.

tions. These differences are related to the differences in magnitude between the vibrationally inelastic potential expansion coefficients for the SHO (Figure 5.2) and 'exact oscillator' (Figure 5.1) representations.

Comparison of cross sections between different representations of the interaction potential for H+ortho–H$_2$

Cross sections for the transition $\nu = 0,\ j = 3 \rightarrow \nu' = 0,\ j' = 1$ are shown in Figure 5.13. Here the ENCO functions have been used and a comparison has been taken between the two interaction potentials of Boothroyd *et al.* [38] (broken curve) and Mielke *et al.* [39] (full curve). At low collision energies (near threshold) there are significant differences between the two potentials. However at higher collision energies there is generally good agreement.

In Figure 5.14 considerable differences are found between the two potentials for the $\nu = 1,\ j = 3 \rightarrow \nu' = 0,\ j' = 1$ transition, when using the ENCO representation. In the near-threshold region the cross sections computed with the potential of Mielke *et al.* [39] increase less steeply than those computed with the potential of Boothroyd *et al.* [38]. At higher energies there are considerable differences between the cross sections calculated for the two potentials. At approximately $E > 25000$ K, and higher, the results are generally in good agreement.

5.3.3 Further examples of transitions in H+para–H$_2$ and H+ortho–H$_2$

The first inelastic rotational transition and first inelastic rovibrational transition have been presented for H+para–H$_2$ and H+ortho–H$_2$. There are substantially more transitions available, approximately 6000, for presentation. It is, of course, impractical to present every transition within this thesis. Therefore transitions have been selected that represent the overall findings from the calculations. For 'completeness' sake we present cross sections for several other transitions in the H+para–H$_2$ and H+ortho–H$_2$ systems.

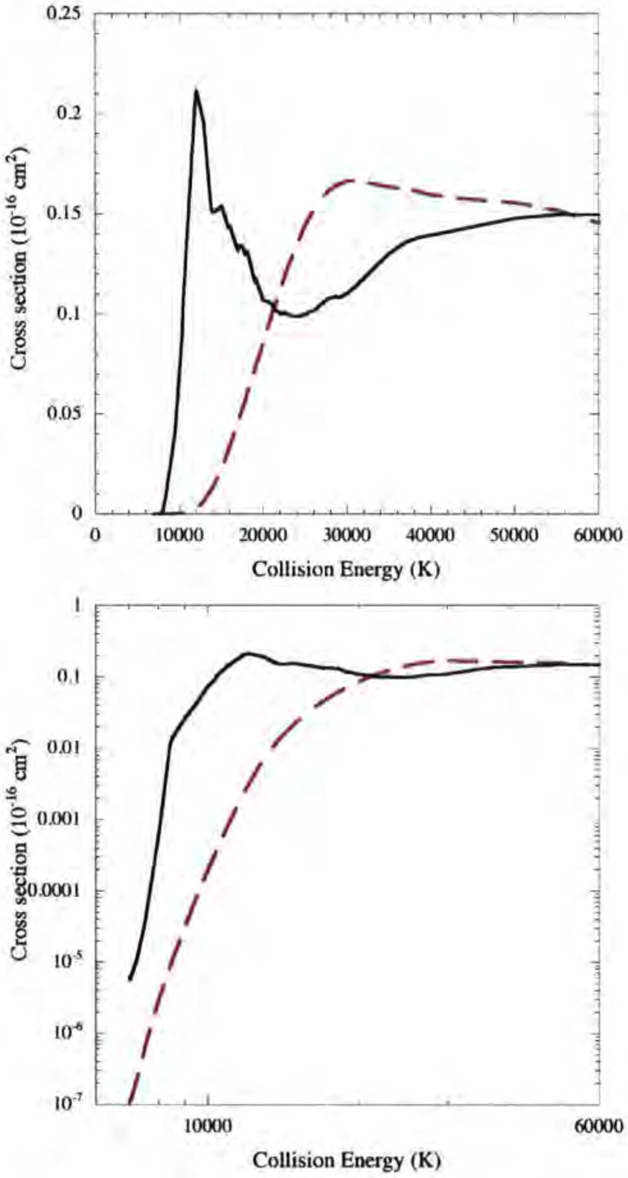

Figure 5.12: A comparison of results obtained for the $\nu = 1,\ j = 3 \rightarrow \nu' = 0,\ j' = 1$ transition using the SHO (broken curve) and 'exact oscillator' (full curve) models. The interaction potential of Mielke *et al.* [39] was used in these calculations and a basis set comprising all states of ortho–H_2 up to and including $\nu = 0, j = 23$.

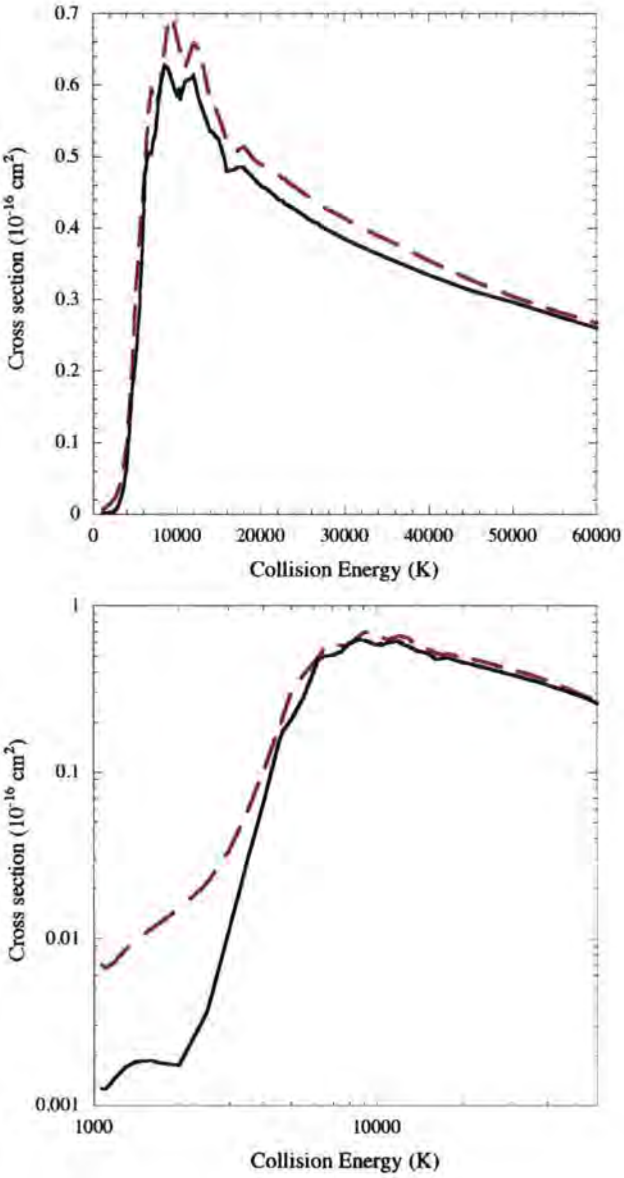

Figure 5.13: A comparison of converged results obtained for the $\nu = 0,\ j = 3 \rightarrow \nu' = 0,\ j' = 1$ transition using the potentials of Boothroyd *et al.* [38] (broken curve) and Mielke *et al.* [39] (full curve). The ENCO vibrational functions were employed in these calculations and a basis set comprising all states of ortho–H_2 up to and including $\nu = 0, j = 23$.

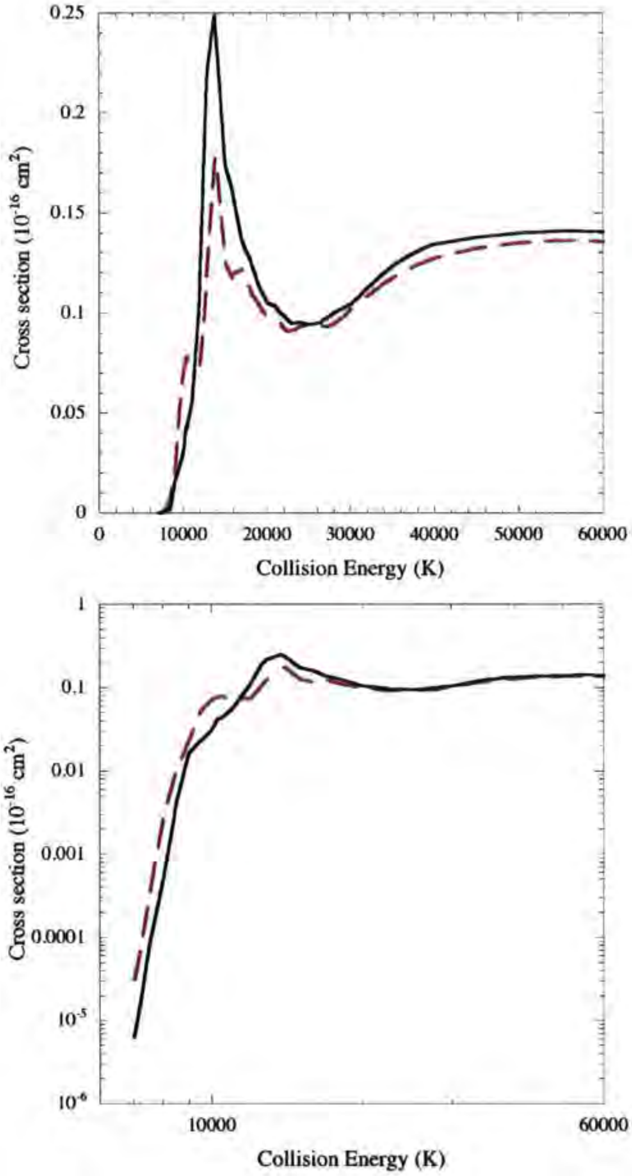

Figure 5.14: A comparison of converged results obtained for the $\nu = 1,\ j = 3 \rightarrow \nu' = 0,\ j' = 1$ transition using the potentials of Boothroyd *et al.* [38] (broken curve) and Mielke *et al.* [39] (full curve). The ENCO vibrational functions were employed in these calculations and a basis set comprising all states of ortho–H_2 up to and including $\nu = 0, j = 23$.

Comparison of cross sections between different representations of the vibrational motion of the molecule

Figure 5.15 shows a rotationally inelastic transition with $\Delta j = 6$, and Figure 5.16 shows a rotationally inelastic transition with $\Delta j = 4$. Similar trends are seen in both. Despite both transitions being vibrationally elastic there are substantial differences between the cross sections obtained using the SHO and 'exact oscillator' functions. The cross sections obtained using the 'exact oscillator' model are orders of magnitude larger than those for the SHO model. The cross sections calculated for the 'exact oscillator' increase more rapidly from threshold and have more structure.

In Figure 5.17 the cross section for a rovibrationally inelastic transition with $\Delta\nu = 2$ and $\Delta j = 2$ is shown. Figure 5.18 shows the case for a transition with $\Delta\nu = 3$ and $\Delta j = 2$. Despite a difference in the magnitude of $\Delta\nu$ similar trends appear in both cases. The cross sections, obtained using the 'exact oscillator' model are orders of magnitude larger near threshold. The magnitude of the discrepancy increases as the magnitude of $\Delta\nu$ increases. The rate of increase in the cross sections, from threshold, is greater using the 'exact oscillator' model and the corresponding cross sections are larger over the entire energy range.

Comparison of cross sections between different representations of the interaction potential

Figures 5.19–5.20 show cross sections for pure rotationally inelastic transitions (cf. Figures 5.15–5.16) obtained for different interaction potentials. For both transitions there is reasonable agreement between the potentials of Boothroyd *et al.* [38] and Mielke *et al.* [39] near threshold. Cross sections obtained using the potential of Mielke *et al.* [39] increase at a slightly faster rate, from threshold, than those obtained with Boothroyd *et al.* [38]. At higher energies there are notable discrepancies between cross sections obtained using the two potentials.

In Figures 5.19–5.20 the cross sections are shown for rovibrationally inelastic transitions (cf. Figures 5.15–5.16) using different interaction potentials.

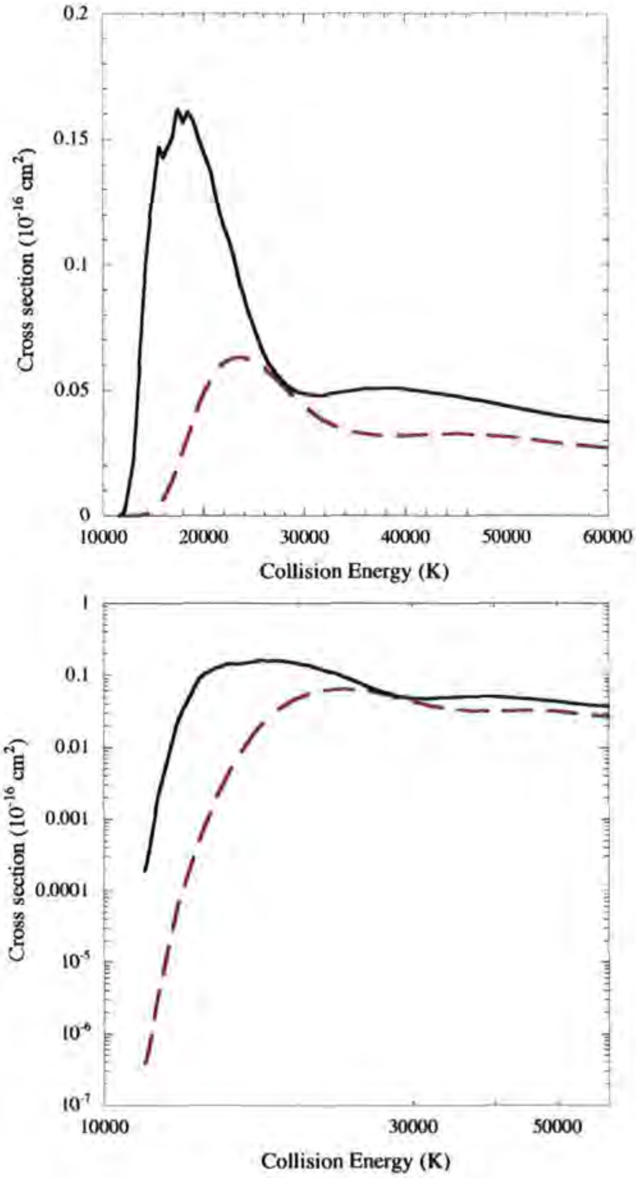

Figure 5.15: A comparison of converged results obtained for the $\nu = 1,\ j = 8 \rightarrow \nu' = 1,\ j' = 2$ transition using the SHO (broken curve) and 'exact oscillator' (full curve) models. The interaction potential of Mielke *et al.* [39] was used in these calculations and a basis set comprising all states of para–H_2 up to and including $\nu = 6, j = 4$.

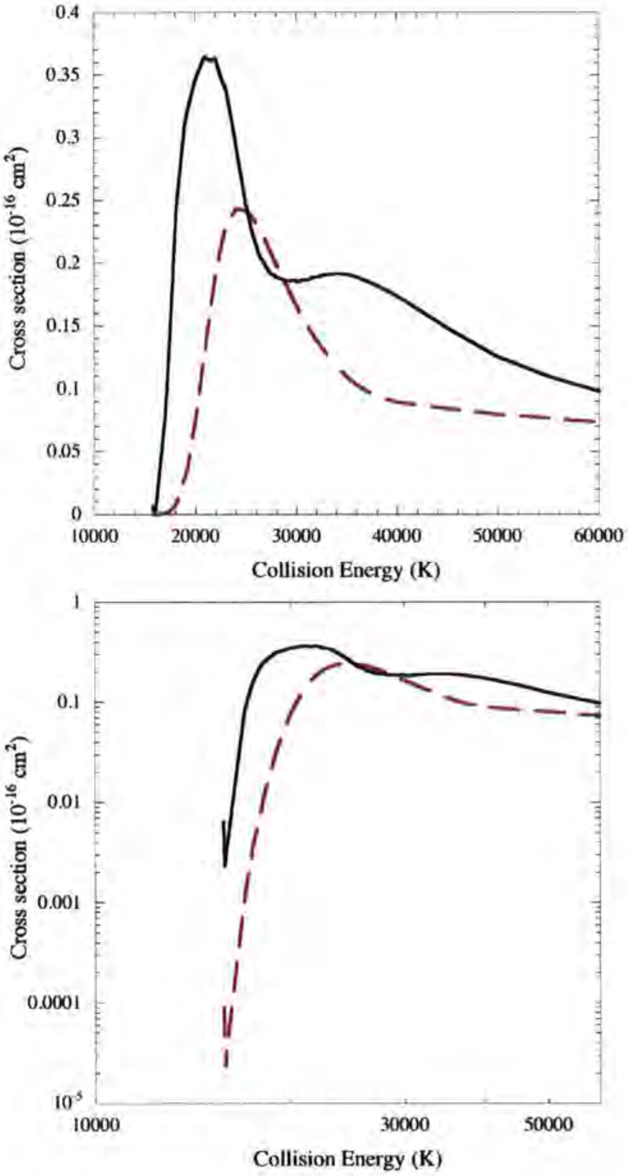

Figure 5.16: A comparison of converged results obtained for the $\nu = 2,\ j = 7 \rightarrow \nu' = 2,\ j' = 3$ transition using the SHO (broken curve) and 'exact oscillator' (full curve) models. The interaction potential of Mielke *et al.* [39] was used in these calculations and a basis set comprising all states of ortho–H_2 up to and including $\nu = 0, j = 23$.

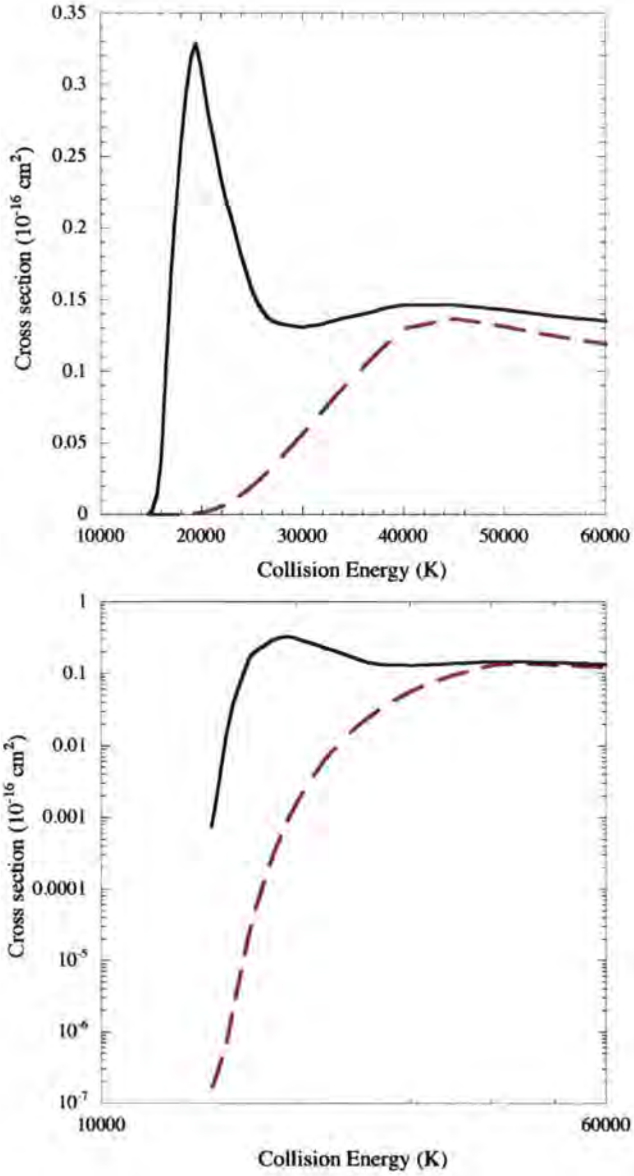

Figure 5.17: A comparison of converged results obtained for the $\nu = 2,\ j = 6 \rightarrow \nu' = 0,\ j' = 4$ transition using the SHO (broken curve) and 'exact oscillator' (full curve) models. The interaction potential of Mielke *et al.* [39] was used in these calculations and a basis set comprising all states of para–H$_2$ up to and including $\nu = 6, j = 4$.

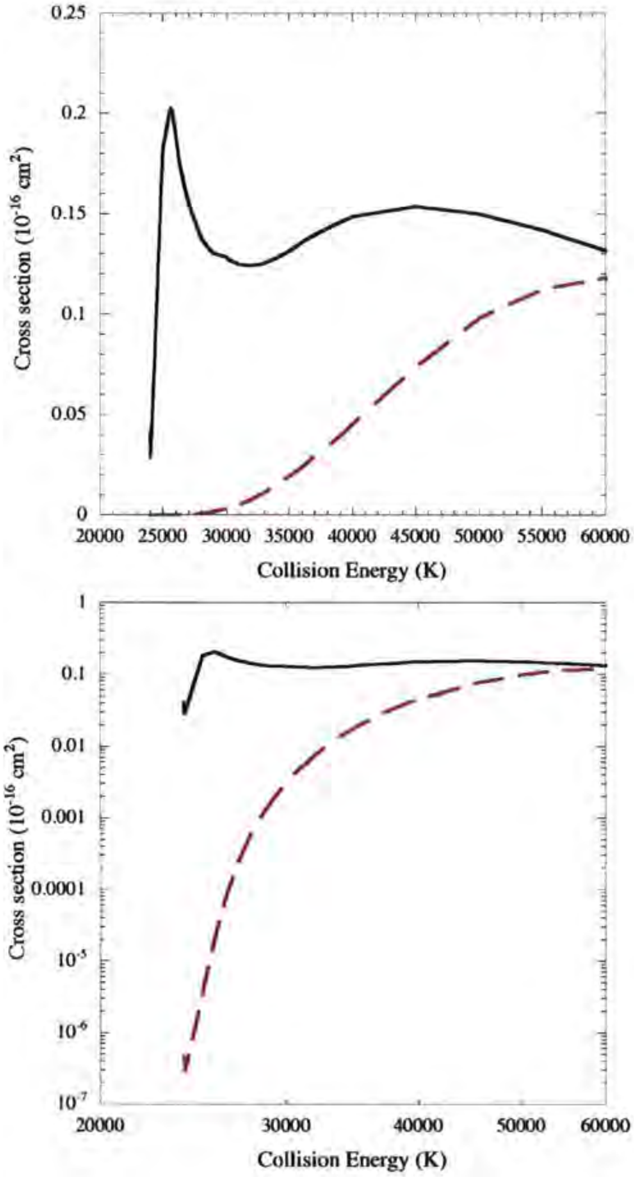

Figure 5.18: A comparison of converged results obtained for the $\nu = 4,\ j = 5 \rightarrow \nu' = 1,\ j' = 3$ transition using the SHO (broken curve) and 'exact oscillator' (full curve) models. The interaction potential of Mielke *et al.* [39] was used in these calculations and a basis set comprising all states of ortho-H_2 up to and including $\nu = 0, j = 23$.

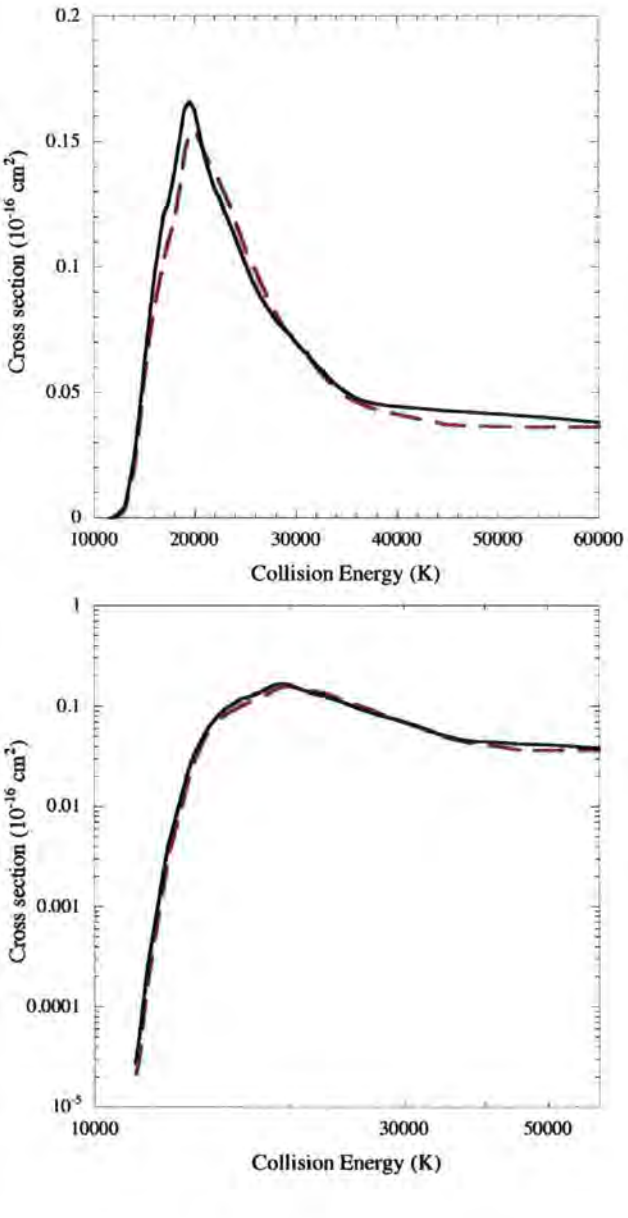

Figure 5.19: A comparison of results obtained for the $\nu = 1,\ j = 8 \rightarrow \nu' = 1,\ j' = 2$ transition using the potentials of Boothroyd *et al.* [38] (broken curve) and Mielke *et al.* [39] (full curve). The ENCO vibrational functions were employed in these calculations and a basis set comprising all states of para–H$_2$ up to and including $\nu = 6, j = 4$.

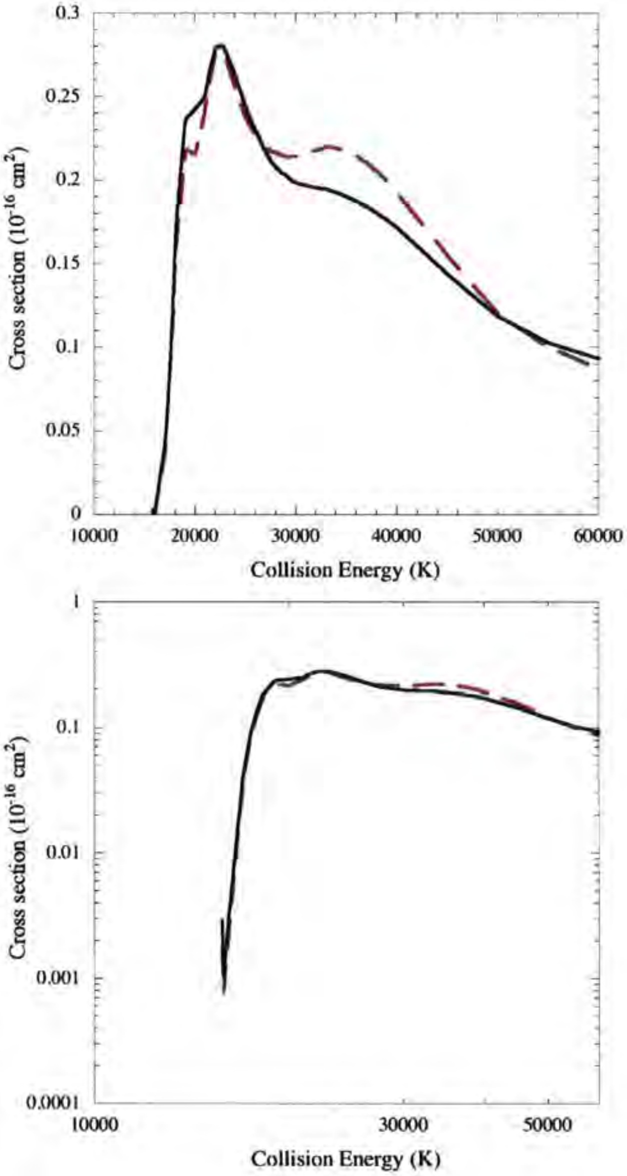

Figure 5.20: A comparison of results obtained for the $\nu = 2,\ j = 7 \rightarrow \nu' = 2,\ j' = 3$ transition using the potentials of Boothroyd *et al.* [38] (broken curve) and Mielke *et al.* [39] (full curve). The ENCO vibrational functions were employed in these calculations and a basis set comprising all states of ortho–H$_2$ up to and including $\nu = 0, j = 23$.

There is good agreement between the potential of Mielke *et al.* [39] and Boothroyd *et al.* [38] near threshold. For both transitions the cross sections peak at a higher value when using the potential of Boothroyd *et al.* [38]. There are notable discrepancies between the cross sections, obtained for each potential, at higher energies.

5.3.4 Summary of cross sections for H+H$_2$

- Cross sections have been presented for rovibrationally inelastic transitions in H+para–H$_2$ and H+ortho–H$_2$ using the quantum mechanical coupled–channels method.

- The convergence of the cross sections with respect to the extent of the basis of rovibrational states was investigated carefully. Convergence was found to be slow, with couplings to states with vibrational quantum number $\nu = 6$ being significant for transitions between $\nu = 1$ and $\nu = 0$, for example. One possible reason for slow convergence is that vibrational excitation requires a substantial transfer of energy to the internal nuclear motion of H$_2$. This can only occur when the H atom is sufficiently close to the H$_2$ molecule for energy transfer to be effective. Therefore the use of vibrational states of the isolated H$_2$ as a basis set may be unsatisfactory. In other words, the slow convergence relates to the fact that H can undergo reactive scattering with H$_2$, at collision energies exceeding a few thousand kelvin. The increase in the magnitudes of the potential coupling coefficients, $y_\lambda(\nu j, \nu' j'|R)$ $(\nu \neq \nu')$ (equation 5.2), which control vibrationally inelastic scattering, with increasing ν, ν' (see Figure 5.1), reflects this fact.

- Considerable differences were found in the cross sections between the vibrational representation of the molecule. The SHO model of the vibrational motion was found to be unsatisfactory, particularly with regard to the predicted rate of increase from threshold of cross sections for vibrationally inelastic transitions.

- Cross sections obtained using the ENCO and 'exact oscillator' models displayed considerably more structure than those obtained using the

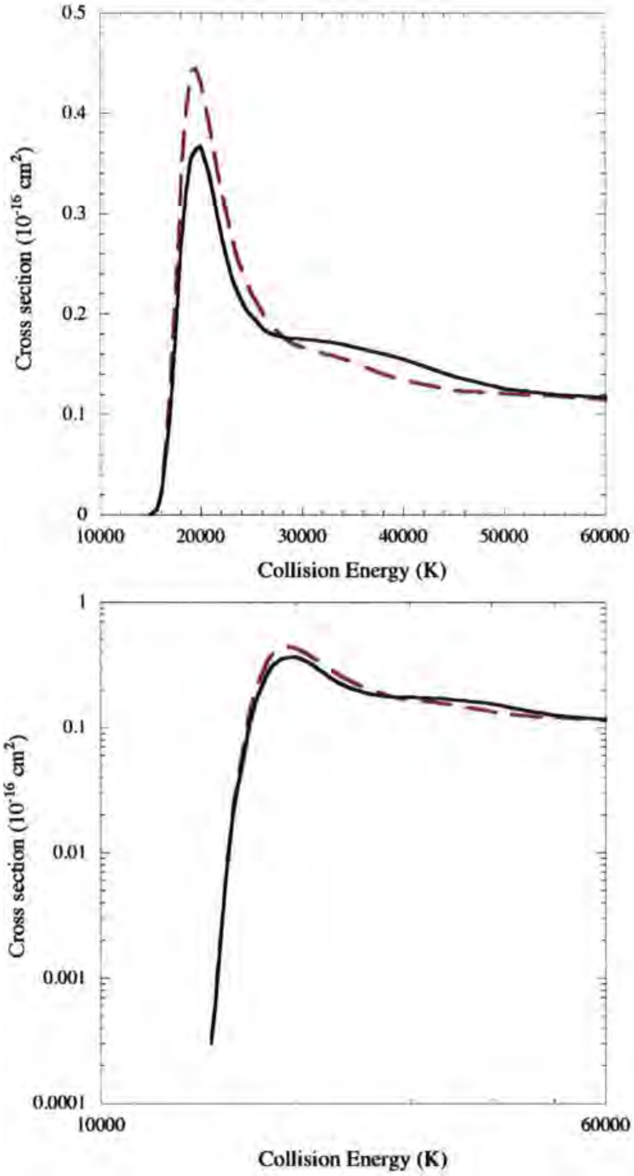

Figure 5.21: A comparison of results obtained for the $\nu = 2,\ j = 6 \rightarrow \nu' = 0,\ j' = 4$ transition using the potentials of Boothroyd *et al.* [38] (broken curve) and Mielke *et al.* [39] (full curve). The ENCO vibrational functions were employed in these calculations and a basis set comprising all states of para–H$_2$ up to and including $\nu = 6, j = 4$.

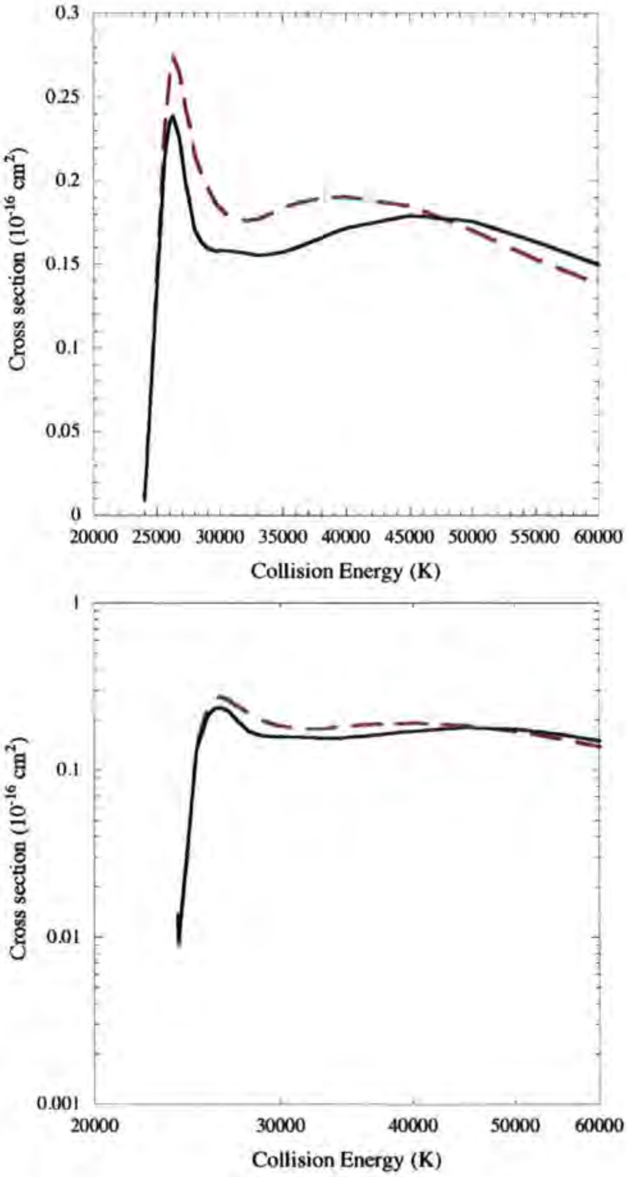

Figure 5.22: A comparison of results obtained for the $\nu = 4,\ j = 5 \rightarrow \nu' = 1,\ j' = 3$ transition using the potentials of Boothroyd *et al.* [38] (broken curve) and Mielke *et al.* [39] (full curve). The ENCO vibrational functions were employed in these calculations and a basis set comprising all states of ortho–H$_2$ up to and including $\nu = 0, j = 23$.

SHO model.

- Cross sections for rovibrationally inelastic scattering, obtained using the potentials of Mielke *et al.* [39] and Boothroyd *et al.* [38], exhibit significant differences in magnitude, notably in the near–threshold region.

5.4 Rate coefficients

In order to obtain rate coefficients as functions of the kinetic temperature, T, the cross sections are integrated over a Maxwellian velocity distribution (see equation (2.90)). When calculating the rate coefficients care was taken to ensure the grid of collision energies was adapted to the opening of new thresholds and other effects which caused rapid variation in the cross sections as a function of barycentric collision energy. However due to the increased structure observed when the 'exact oscillator' representation is used it becomes difficult to incorporate every feature for all transitions.

The rate coefficients were computed numerically on a grid of temperatures extending from 0 K to 6000 K at every 100 K. Only a subset of the calculated rate coefficients are presented in this thesis. A complete collection of the calculated rate coefficients can be found at http://ccp7.dur.ac.uk.

Comparison of rate coefficients between different representations of the vibrational motion of the molecule

Figure 5.23a shows the rate coefficient, as a function of kinetic temperature, for the $\nu = 0,\ j = 2 \rightarrow \nu' = 0,\ j' = 0$ transition using the SHO (broken curve) and 'exact oscillator' (full curve) models. The potential of Mielke *et al.* [39] was used. There is reasonable agreement in the magnitude of the rate coefficients between the two vibrational representations over the entire temperature range. However, there are differences in the behaviour of the rate coefficients between the two models and this is related to the behaviour of their associated cross sections as function of energy (see Figures 5.3 and 5.4). At low temperatures the rate coefficients for the 'exact oscillator' model are smaller than those for the SHO model. A similar trend is seen in the corresponding cross sections, at low energies. At intermediate energies the cross sections for the 'exact oscillator' rise more rapidly than those for the SHO and this is seen at intermediate temperatures for their corresponding rate coefficients. For the highest temperature values the SHO rate coefficient is larger than that of the 'exact oscillator'. This is reflected in the high energy behaviour of the corresponding cross sections.

In Figure 5.23b the rate coefficient, as a function of kinetic temperature, is shown for the $\nu = 1,\ j = 2 \rightarrow \nu' = 0,\ j' = 0$ transition for the SHO (broken curve) and 'exact oscillator' (full curve) models using the potential of Mielke *et al.* [39]. At low temperatures the rate coefficients obtained using the 'exact oscillator' model are over two orders of magnitude larger than those determined using the SHO model. Large discrepancies remain between the two vibrational representations as the temperature increases. Only at higher temperatures ($T > 5000$ K) do the rate coefficients become comparable. The large discrepancies in the rate coefficients between the SHO and 'exact oscillator' models are related to the large discrepancies between their corresponding cross sections (see Figures 5.5 and 5.6). At higher collision energies there is better agreement between the cross sections and this is reflected in the behaviour of the high temperature rate coefficients.

Figures 5.24a and 5.24b show pure rotationally inelastic transitions for $\Delta j = 6$ and $\Delta j = 4$, respectively. At low temperatures the rate coefficients calculated using 'exact oscillator' functions are several orders of magnitude larger than those obtained using the SHO functions. At higher temperatures the rate coefficients for the 'exact oscillator' are several factors larger than those obtained using the SHO functions.

In Figures 5.24c and 5.24d the rate coefficients are presented for rovibrationally inelastic transitions with $\Delta\nu = 2,\ \Delta j = 2$ and $\Delta\nu = 3,\ \Delta j = 2$, respectively. At low temperatures the rate coefficients for the 'exact oscillator' model are several orders of magnitude larger than those obtained using SHO functions. The discrepancies at low temperature increase as $\Delta\nu$ increases. The rate coefficients obtained using 'exact oscillator' functions remain substantially larger, than those using SHO functions, over the entire temperature range calculations were performed at.

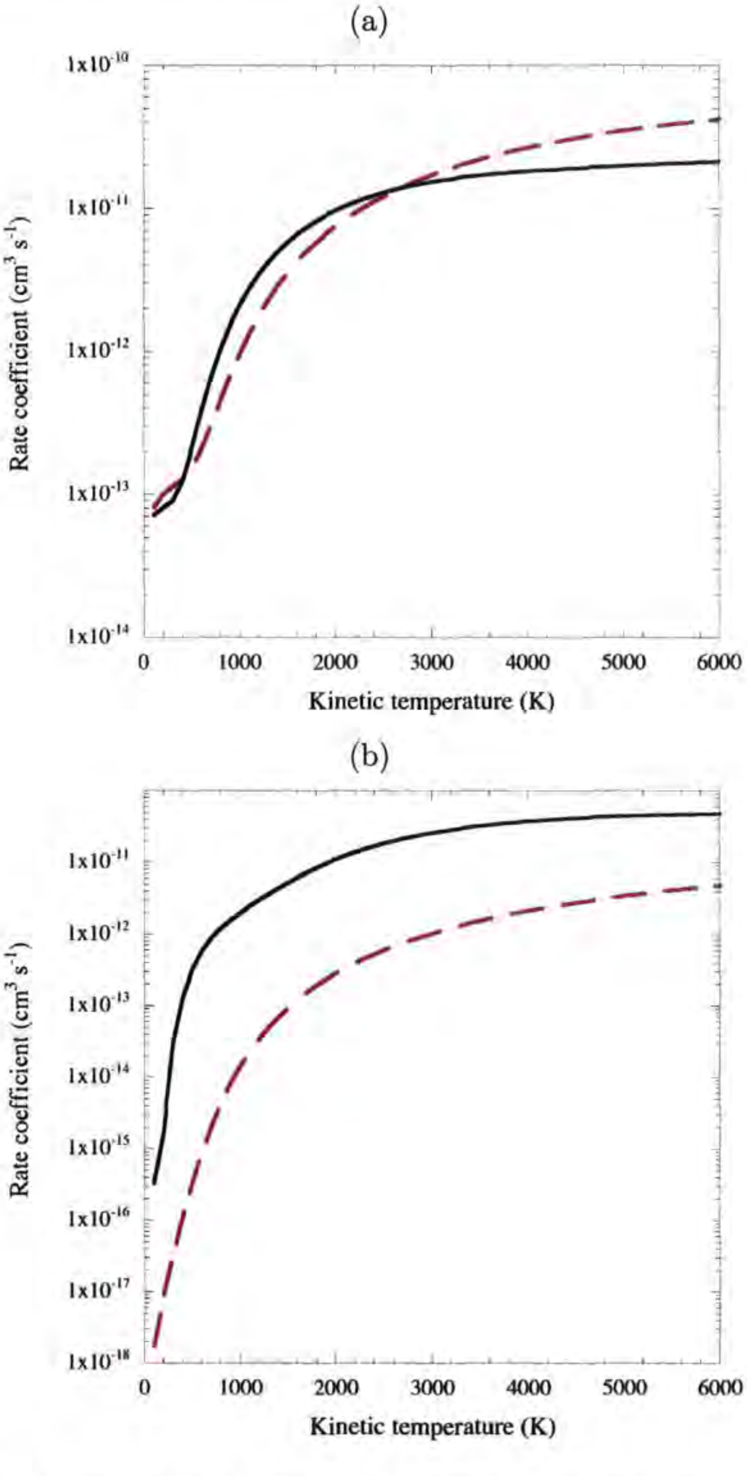

Figure 5.23: A comparison of rate coefficients, as a function of kinetic temperature T, obtained for the for the (a) $\nu = 0,\ j = 2 \rightarrow \nu' = 0,\ j' = 0$, (b) $\nu = 1,\ j = 2 \rightarrow \nu' = 0,\ j' = 0$ transitions using the SHO (broken curve) and 'exact oscillator' (full curve) models. The interaction potential of Mielke *et al.* [39] was used in these calculations.

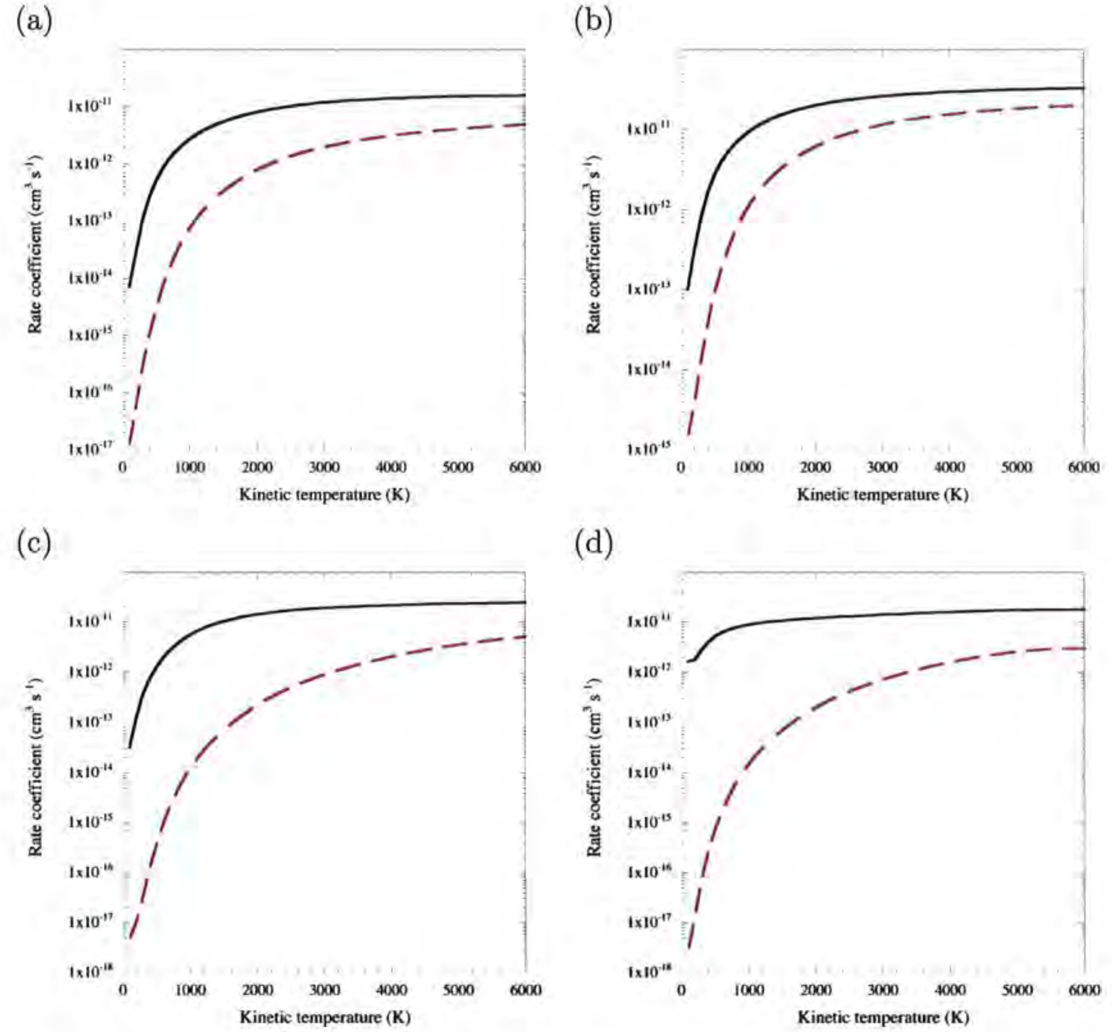

Figure 5.24: A comparison of rate coefficients, as a function of kinetic temperature T, obtained for the for the (a) $\nu = 1,\ j = 9 \rightarrow \nu' = 1,\ j' = 3$, (b) $\nu = 2,\ j = 7 \rightarrow \nu' = 2,\ j' = 3$, (c) $\nu = 2,\ j = 6 \rightarrow \nu' = 0,\ j' = 4$, (d) $\nu = 4,\ j = 5 \rightarrow \nu' = 1,\ j' = 3$ transitions using the SHO (broken curve) and 'exact oscillator' (full curve) models. The interaction potential of Mielke *et al.* [39] was used in these calculations.

Comparison of rate coefficients between different representations of the interaction potential

The rate coefficients, as a function of kinetic temperature T, obtained for the $\nu = 0,\ j = 2 \rightarrow \nu' = 0,\ j' = 0$ transition using the potentials of Boothroyd *et al.* [38] (broken curve) and Mielke *et al.* [39] (full curve) are shown in Figure 5.25a. The ENCO vibrational functions were employed in these calculations. There is reasonable agreement between the two potentials, although the rate coefficients determined for the potential of Boothroyd *et al.* [38] are larger than those of Mielke *et al.* [39] over the entire temperature range. This is expected, as examination of the corresponding cross sections (see Figure 5.9) shows those obtained with the potential of Boothroyd *et al.* [38] are larger over the entire energy range.

Figure 5.25b shows the rate coefficients, as a function of kinetic temperature T, obtained for the $\nu = 1,\ j = 2 \rightarrow \nu' = 0,\ j' = 0$ transition using the potentials of Boothroyd *et al.* [38] (broken curve) and Mielke *et al.* [39] (full curve). Again, the ENCO vibrational functions were employed. There are considerable differences between the rate coefficients obtained for each potential which are directly related to the considerable differences found between their corresponding cross sections (see Figure 5.10).

Rate coefficients for pure rotationally inelastic transitions with $\Delta j = 6$ and $\Delta j = 4$ are presented in Figures 5.26a and 5.26b, respectively. There is good agreement between the rate coefficients obtained using the potentials of Boothroyd *et al.* [38] and Mielke *et al.* [39] for all calculated temperatures. Any notable discrepancies occur at the lowest temperatures.

In Figures 5.26c and 5.26d rate coefficients are presented for rovibrationally inelastic transitions $\Delta\nu = 2,\ \Delta j = 2$ and $\Delta\nu = 3,\ \Delta j = 2$, respectively. At low temperatures good agreement is found between rate coefficients obtained using both potentials. As the temperature increases the rate coefficients calculated using the potential of Boothroyd *et al.* [38] becomes moderately larger than those obtained for the potential of Mielke *et al.* [39].

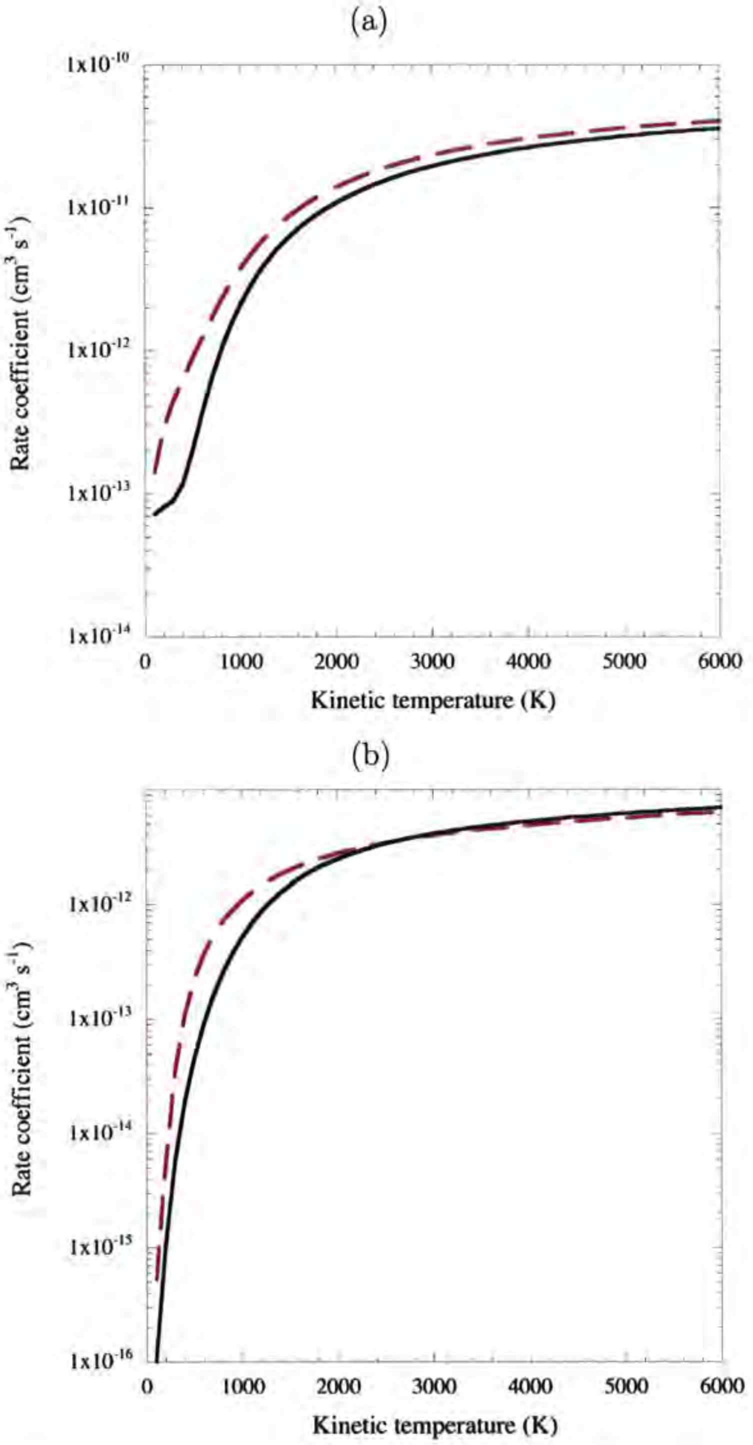

Figure 5.25: A comparison of rate coefficients, as a function of kinetic temperature T, obtained for the for the (a) $\nu = 0,\ j = 2 \rightarrow \nu' = 0,\ j' = 0$, (b) $\nu = 1,\ j = 2 \rightarrow \nu' = 0,\ j' = 0$ transitions using the potentials of Boothroyd *et al.* [38] (broken curve) and Mielke *et al.* [39] (full curve). The ENCO vibrational functions were employed in these calculations.

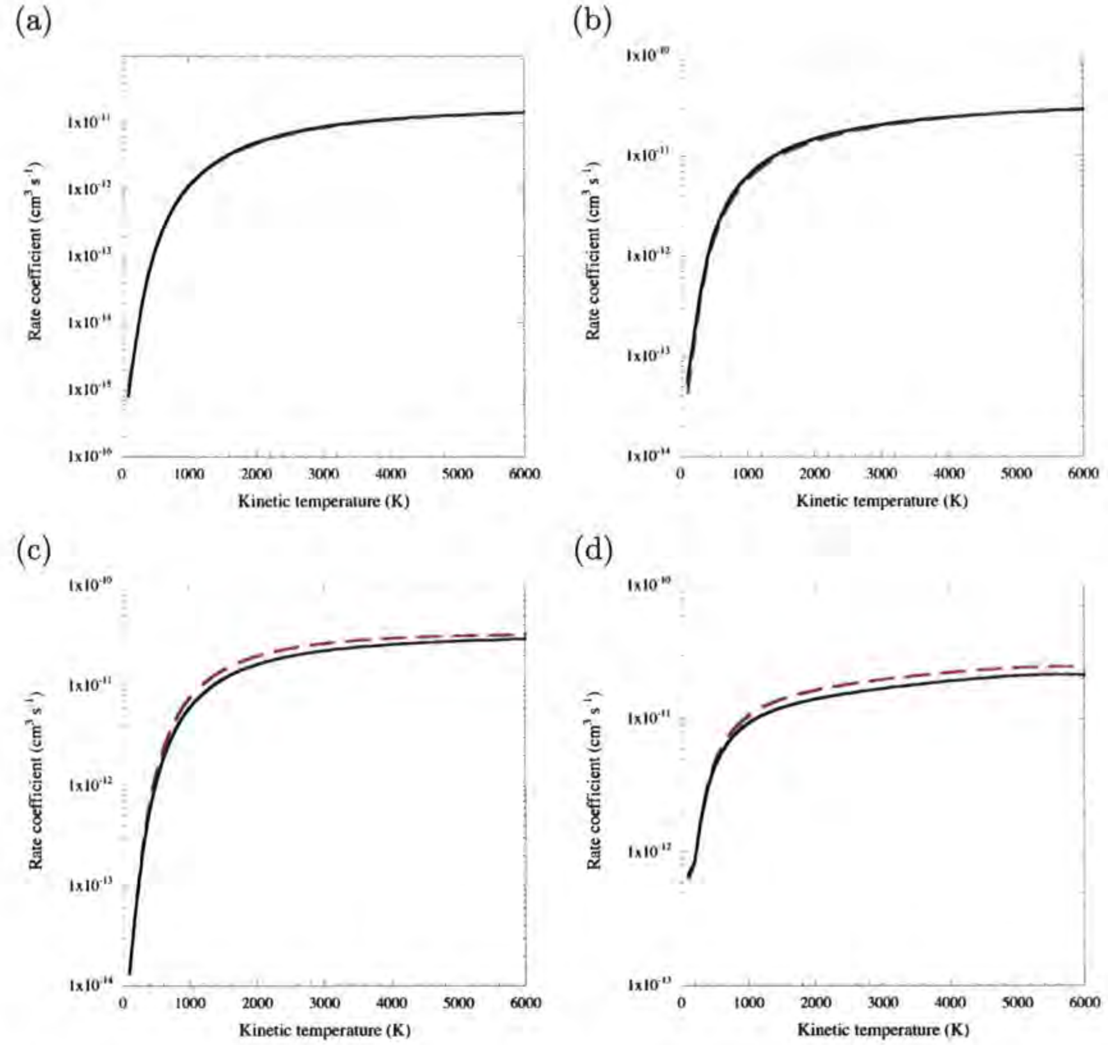

Figure 5.26: A comparison of rate coefficients, as a function of kinetic temperature T, obtained for the for the (a) $\nu = 1,\ j = 9 \rightarrow \nu' = 1,\ j' = 3$, (b) $\nu = 2,\ j = 7 \rightarrow \nu' = 2,\ j' = 3$, (c) $\nu = 2,\ j = 6 \rightarrow \nu' = 0,\ j' = 4$, (d) $\nu = 4,\ j = 5 \rightarrow \nu' = 1,\ j' = 3$ transitions using the potentials of Boothroyd *et al.* [38] (broken curve) and Mielke *et al.* [39] (full curve). The ENCO vibrational functions were employed in these calculations.

5.4.1 Summary of rate coefficients for $H+H_2$

- Thermally averaged rate coefficients have been presented for rovibrationally inelastic transitions in H+para–H_2 and H+ortho–H_2 .

- Rate coefficients calculated using the 'exact oscillator' and ENCO models were considerably larger than those obtained using the SHO model at low temperatures. The 'exact oscillator' rate coefficients were typically the largest over the entire temperature range.

- The rate coefficients calculated for the potentials of Mielke *et al.* [39] and Boothroyd *et al.* [38] were in reasonable agreement. Some discrepancies were found at low temperatures.

Chapter 6

Calculations for H+HD

In this chapter the results of the scattering calculations for H+HD are presented. We begin with an analysis of the potential expansion coefficients for the H+HD system. Next, we discuss the basis sets used to describe the system in the scattering calculations. Then the cross sections as a function of the barycentric collision energy, E, are presented. Finally, the corresponding rate coefficients are presented as function of kinetic temperature, T.

Results from this chapter have been presented in [54].

6.1 Potential Expansion Coefficients

As for the case of H+H_2 , the potential expansion coefficients are required to proceed with the scattering calculation. The theoretical methods used are the same as those discussed in Section 5.1.

The electrostatic interaction between H and HD is identical to that between H and H_2 . Therefore the same interaction potentials, as those used in the H+H_2 calculations, may be used. However, the centre of mass of HD is displaced from the midpoint of its internuclear axis. As the (Jacobi) coordinates of the incoming atom are expressed relative to the centre of mass of the molecule, the corresponding interaction potential contains terms which give rise to inelastic scattering in which the rotational quantum number, j, of the HD molecule changes by both even and odd integers, Δj. For example, transitions with $\Delta j = 1$, forbidden in non-reactive H+H_2 scattering, are

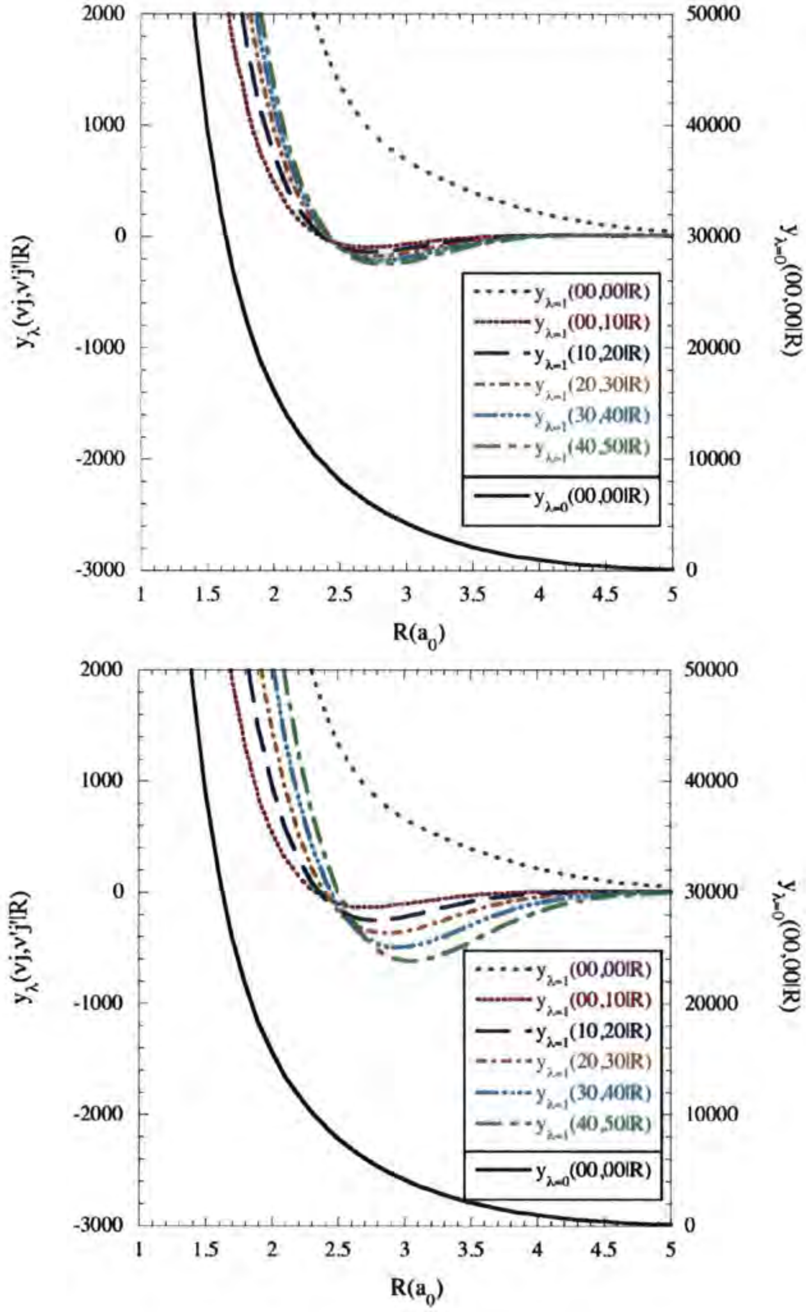

Figure 6.1: The variation with R of $y_\lambda(\nu 0, \nu' 0|R)$, in units of kelvin, for $\lambda = 1$ and selected pairs of values of ν, ν'. The full black line represents $y_{\lambda=0}(00, 00|R)$, which controls elastic scattering. The results presented here refer to the potential of Mielke *et al.* [39] with the SHO functions (top) and the ENCO functions (bottom).

allowed in collisions of H with HD. Essentially odd λ terms are now included in the expansion of the interaction potential (see equation (5.1)).

The potential expansion coefficients are used to determine the integrals given in equation (5.2). The rovibrational eigenfunctions for HD are different to those for H_2, due to the difference in the reduced mass of HD, and were calculated using the methods given in Chapter 4.

The integrals $y_\lambda(\nu j, \nu' j'|R)$ were calculated using the interaction potential of Mielke *et al.* [39] and Boothroyd *et al.* [38], for $0 \leq \lambda \leq 6$ and $1.0 \leq R \leq 25.0\ a_0$; the terms with $\lambda = 0, 1, 2, \cdots, 6$ were sufficient to obtain convergence of the potential expansion. This was confirmed by inspection of the coefficients and by performing some cross section calculations with higher order terms included. In terms of the cross sections, 'convergence' was to 4 significant figures.

In Figure 6.1 the integrals, $y_\lambda(\nu j, \nu' j'|R)$, for $\lambda = 0, 1$ are shown for the interaction potential of Mielke *et al.* [39] using the 'exact oscillator' and SHO functions. The integrals are larger in magnitude for $\nu \neq \nu'$ when the 'exact oscillator' functions are used.

Figure 6.2 shows the integrals, $y_\lambda(\nu j, \nu' j'|R)$, for $\lambda = 0, 2$ calculated using the interaction potential of Mielke *et al.* [39] and using the 'exact oscillator' and SHO functions. The integrals are, again, larger for the 'exact oscillator' case. In comparison to the $\lambda = 2$ terms for H_2 (see Figure 5.1), the terms for HD are moderately smaller in magnitude.

Also, the integrals, $y_\lambda(\nu j, \nu' j'|R)$, calculated for the interaction potential of Boothroyd *et al.* [38] were comparable to those determined from the potential of Mielke *et al.* [39].

6.2 Basis Set

The HD molecule contains rovibrational energy levels with even and odd values of j. As for the case of $H+H_2$, reactive scattering may occur at high collision energies (see section 5.2). For H+HD the reactive channels open for collision energies higher than $E \sim 4500$ K [56]. For the calculations presented in this thesis reactive scattering is neglected. Therefore no reactive scattering

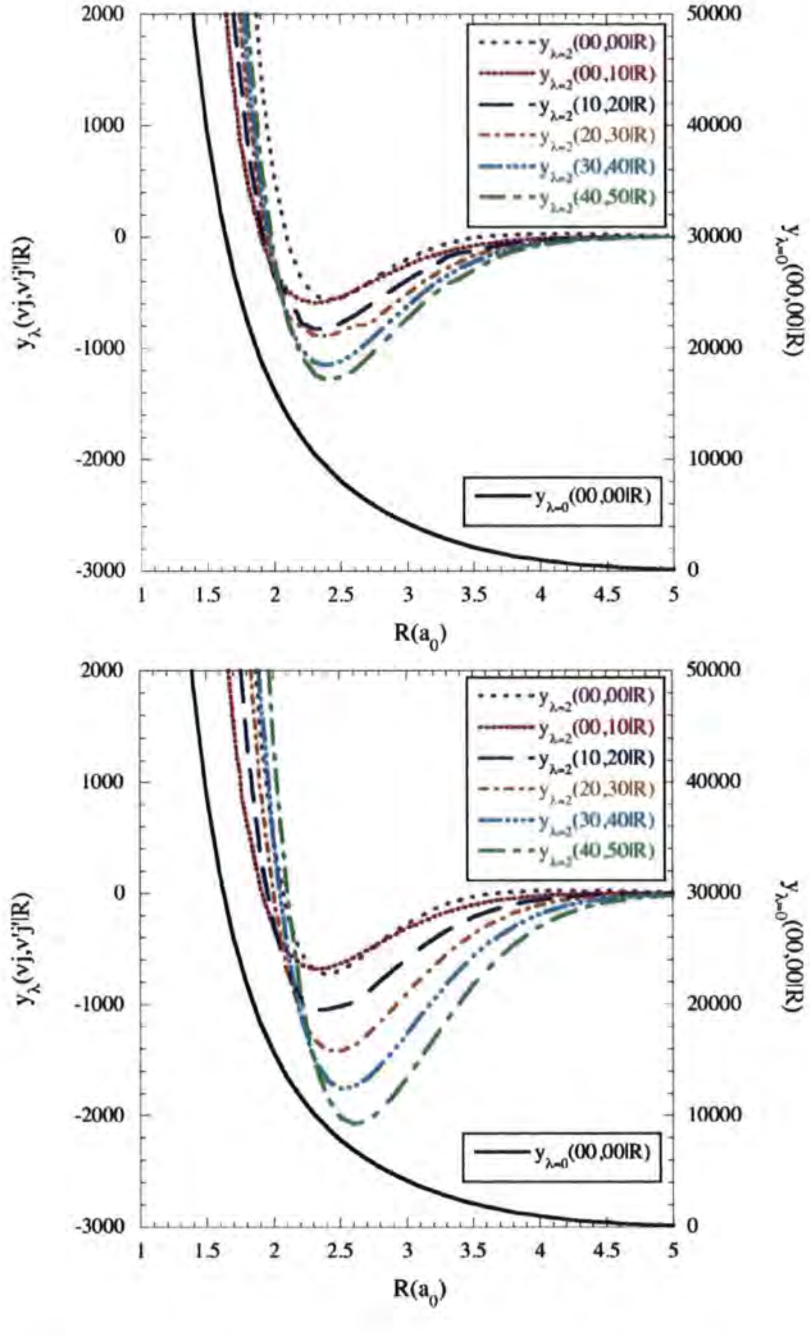

Figure 6.2: The variation with R of $y_\lambda(\nu 0, \nu' 0|R)$, in units of kelvin, for $\lambda = 2$ and selected pairs of values of ν, ν'. The full black line represents $y_{\lambda=0}(00, 00|R)$, which controls elastic scattering. The results presented here refer to the potential of Mielke *et al.* [39] with the SHO functions (top) and the ENCO functions (bottom).

states are present in the basis set.

States associated with the electronic excitation of the H–atom or the HD molecule are not included in the basis set. The energy transfer from heavy nuclei to the relatively light electrons is typically an inefficient process and the energy required to achieve electronically excited states is typically higher than the barycentric collision energies at which calculations have been performed for.

The basis set set used for the calculations of H+HD contains one energy level corresponding to the ground state of the structureless atom, and the rovibrational energy levels of HD. The rovibrational energy levels of the HD molecule used in our calculations were taken from the experimental work of Dabrowski and Herzberg [57] complemented by the theoretical values of Abgrall, Roueff, and Viala [58].

6.2.1 Determining the size of the basis set

The approach in determining the size of the basis set was empirical: the basis set was extended upwards in the energy of the HD rovibrational levels until satisfactory convergence was obtained. Owing to the strong coupling between the vibrational levels (see Figures 6.1 and 6.2), it was necessary to include energy levels which were much higher than the relative collision energy of the atom and the molecule.

Figures 6.3–6.4 show the first two pure rotational transitions in HD as a function of basis set size, with rotational states $j = 0, 1, 2, \cdots, 6$ being included in each vibrational manifold, up to the specified value of the vibrational quantum number, ν. The $\nu = 0,\ j = 1 \rightarrow \nu' = 0,\ j' = 0$ transition[1] (in Figure 6.3) achieves convergence to four significant figures for $\nu \leq 6$. For the case of the $\nu = 0,\ j = 2 \rightarrow \nu' = 0,\ j' = 0$ transition, the convergence rate is slower. With a basis set size of $\nu \leq 6$ the convergence was achieved to several percent over the energy range.

The convergence problem for the first two rovibrationally inelastic transi-

---

[1] Transitions involving higher initial rovibrational states may require a basis set that includes rovibrational levels with $\nu > 6$ to achieve satisfactory convergence.

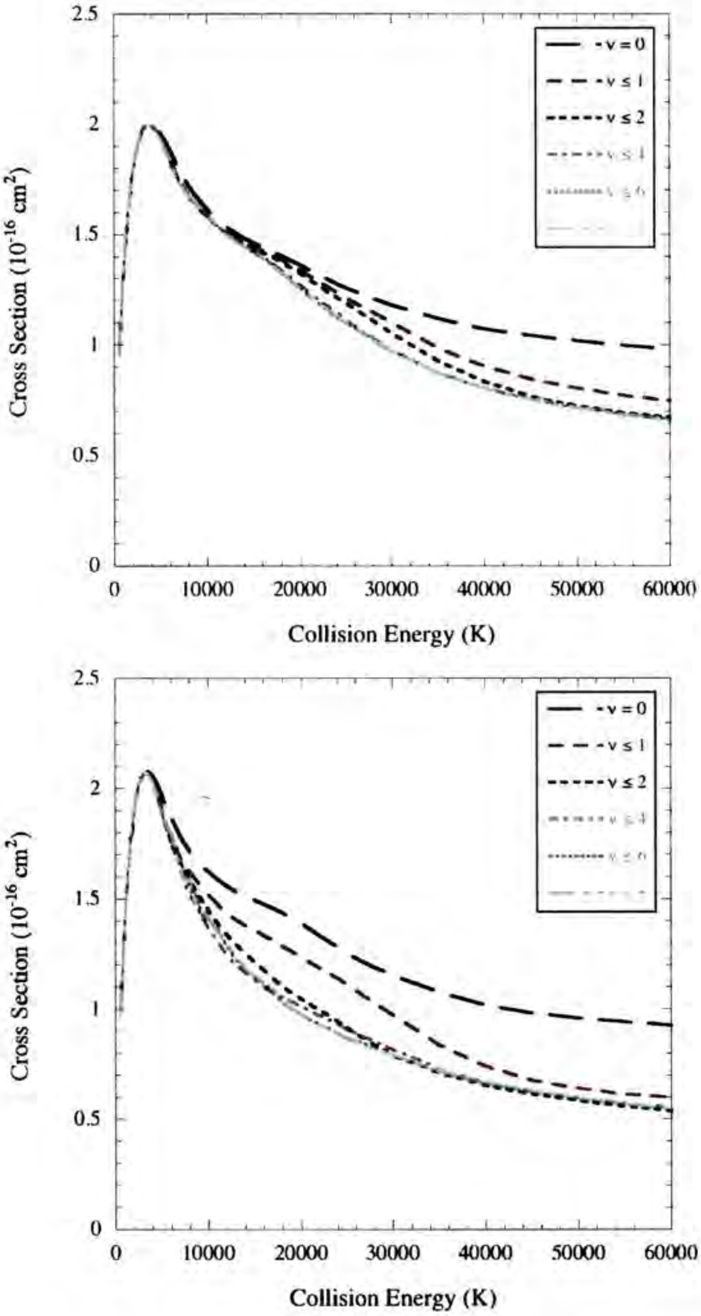

Figure 6.3: Cross section for the $\nu = 0,\ j = 1 \rightarrow \nu' = 0,\ j' = 0$ transition, calculated using SHO (top) and ENCO (bottom) vibrational eigenfunctions. The results are given as a function of basis set size, with rotational states $j = 0, 1, 2, \cdots, 6$ being included in each vibrational manifold, up to the specified value of the vibrational quantum number, ν.

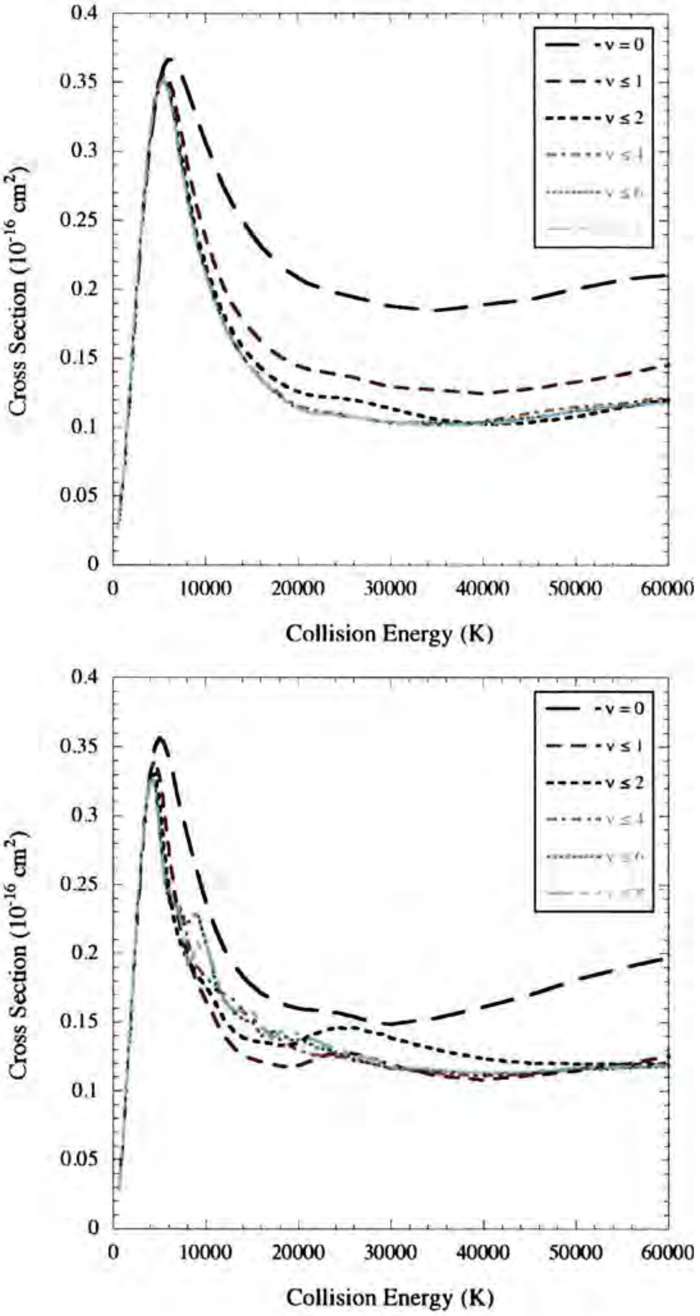

Figure 6.4: Cross section for the $\nu = 0,\ j = 2 \rightarrow \nu' = 0,\ j' = 0$ transition, calculated using SHO (top) and ENCO (bottom) vibrational eigenfunctions. The results are given as a function of basis set size, with rotational states $j = 0, 1, 2, \cdots, 6$ being included in each vibrational manifold, up to the specified value of the vibrational quantum number, ν.

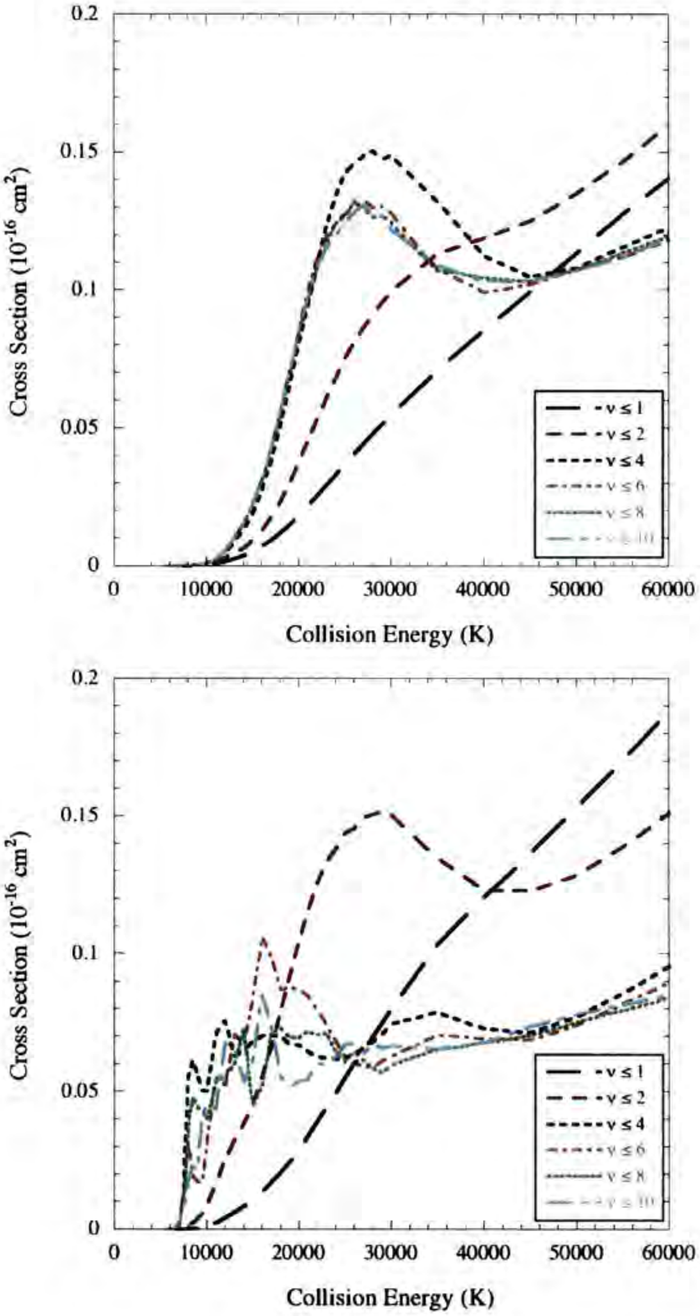

Figure 6.5: Cross section for the $\nu = 1,\ j = 1 \rightarrow \nu' = 0,\ j' = 0$ transition, calculated using SHO (top) and ENCO (bottom) vibrational eigenfunctions. The results are given as a function of basis set size, with rotational states $j = 0, 1, 2, \cdots, 6$ being included in each vibrational manifold, up to the specified value of the vibrational quantum number, ν.

tions in HD is considered in Figures 6.5–6.6. In both Figures the rate of convergence is faster for the SHO model than for the ENCO model. For high collision energies there is reasonable convergence for both models and both transitions. However, for collision energies ranging from threshold up to 40000 K there are convergence problems in both transitions when using the ENCO model.

The basis set for H+HD calculations contains both even and odd j rovibrational energy levels. Therefore, the size of the basis set increases more rapidly as a function of ν than the basis set for $H+H_2$ calculations. To achieve convergence for rovibrationally inelastic transitions a large basis set was needed. In the case of HD, we included the lowest 120 of the total of 399 bound rovibrational energy levels (i.e. the basis set contains all rovibrational energy levels up to and including $\nu = 5$, $j = 11$ for HD). They are listed in Appendix C.

6.3 Cross Sections

With a 120 level basis set size there will be data produced for 14400 transitions. Only a representative subset of results are presented within this thesis. However, a large number of other transitions have been analysed to ensure that the trends found, for the results presented here, hold for most of the available transitions.

De–excitation cross sections are presented within this thesis. The principle of detailed balance (see equation (2.90)) may be used to obtain the equivalent excitation cross sections. The complete set of cross sections, as a function of barycentric collision energy, is available from http://ccp7.dur.ac.uk.

Cross sections for H+HD were calculated for 160 barycentric collision energies ranging from 150 K to 60000 K. When selecting specific collision energies, care was taken to choose values sufficiently close to threshold energies. The chosen collision energy grid is believed to give reasonable coverage for low-energy and high-energy structure in the cross sections.

Calculations were performed using the interaction potentials of Mielke *et al.* [39] and Boothroyd *et al.* [38]. Cross sections were obtained for SHO, Morse

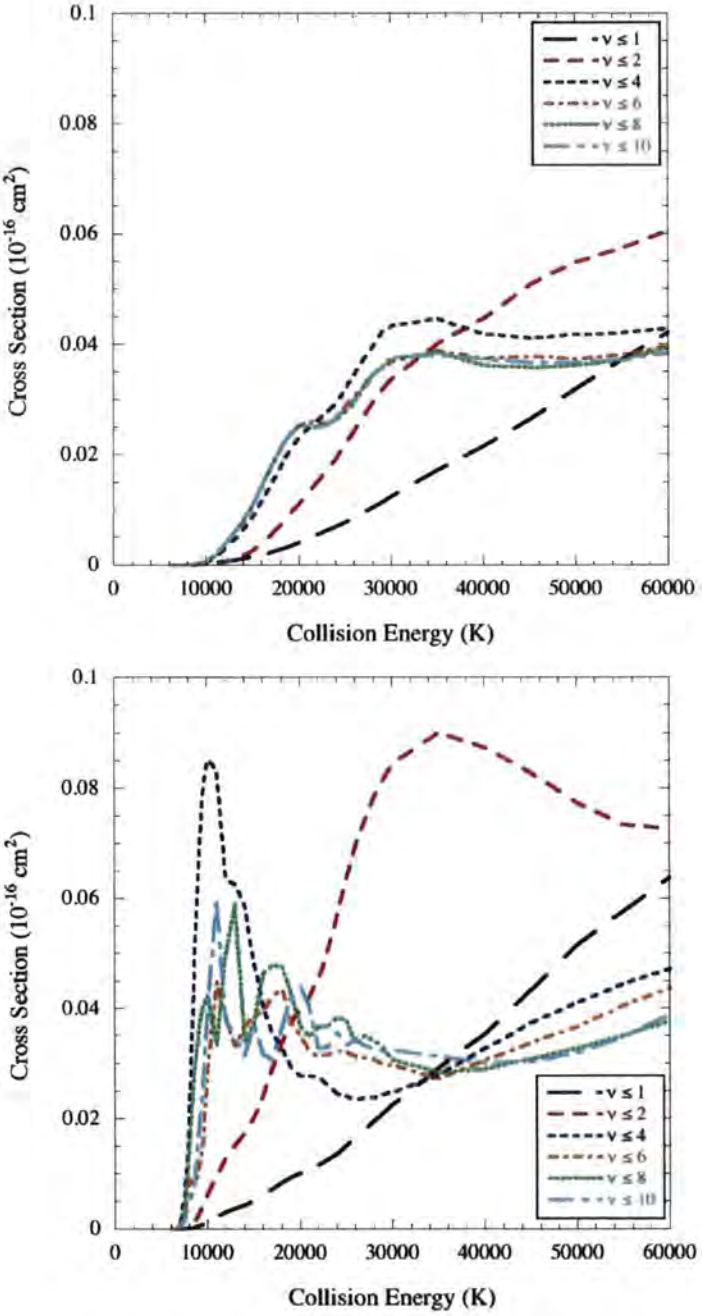

Figure 6.6: Cross section for the $\nu = 1,\ j = 2 \rightarrow \nu' = 0,\ j' = 0$ transition, calculated using SHO (top) and ENCO (bottom) vibrational eigenfunctions. The results are given as a function of basis set size, with rotational states $j = 0, 1, 2, \cdots, 6$ being included in each vibrational manifold, up to the specified value of the vibrational quantum number, ν.

oscillator, and ENCO[2] vibrational representations of the HD molecule. The greatest discrepancies were between the SHO and ENCO calculations; the Morse oscillator results were closer to the ENCO results.

Comparison of cross sections between different representations of the vibrational motion of the molecule for HD

In the cross sections for $H+H_2$ there were considerable discrepancies found between cross sections obtained using the SHO and ENCO models, particularly for rovibrationally inelastic transitions. The cross sections obtained for H+HD exhibit similar discrepancies.

In Figures 6.7 and 6.8 the first pure rotational transitions in HD, which are $\nu = 0,\ j = 1 \rightarrow \nu' = 0,\ j' = 0$ and $\nu = 0,\ j = 2 \rightarrow \nu' = 0,\ j' = 0$ respectively, are shown for the SHO and ENCO models using the interaction potential of Mielke *et al.* [39]. At low energies, near threshold, and energies increasing from threshold, there is good agreement between the SHO and ENCO vibrational representations. At higher energies discrepancies emerge between the two models, with considerably more structure present for the ENCO case. For both transitions, the cross sections for the ENCO model decrease at a faster rate from their respective maximum values. The cross section for the $\nu = 0,\ j = 2 \rightarrow \nu' = 0,\ j' = 0$ transition is comparable, in magnitude, to that obtained for the same transition in H_2 (see Figure 5.4) but is considerably smaller than the cross section obtained for the $\nu = 0,\ j = 1 \rightarrow \nu' = 0,\ j' = 0$ transition.

Figures 6.9 and 6.10 show cross sections corresponding to the rovibrationally inelastic transitions $\nu = 1,\ j = 1 \rightarrow \nu' = 0,\ j' = 0$ and $\nu = 1,\ j = 2 \rightarrow \nu' = 0,\ j' = 0$, respectively. There are considerable differences between cross sections, obtained for the SHO and ENCO models, for energies near, and increasing, from threshold. The cross sections obtained using the ENCO model contain considerably more structure for energies up to 25000–30000 K. At high collision energies the cross sections continue to increase for both vibrational models, although discrepancies remain between the two. The

---

[2] ENCO refers to the exact oscillator rovibrational eigenfunctions with the centrifugal term neglected, see section 4.1.

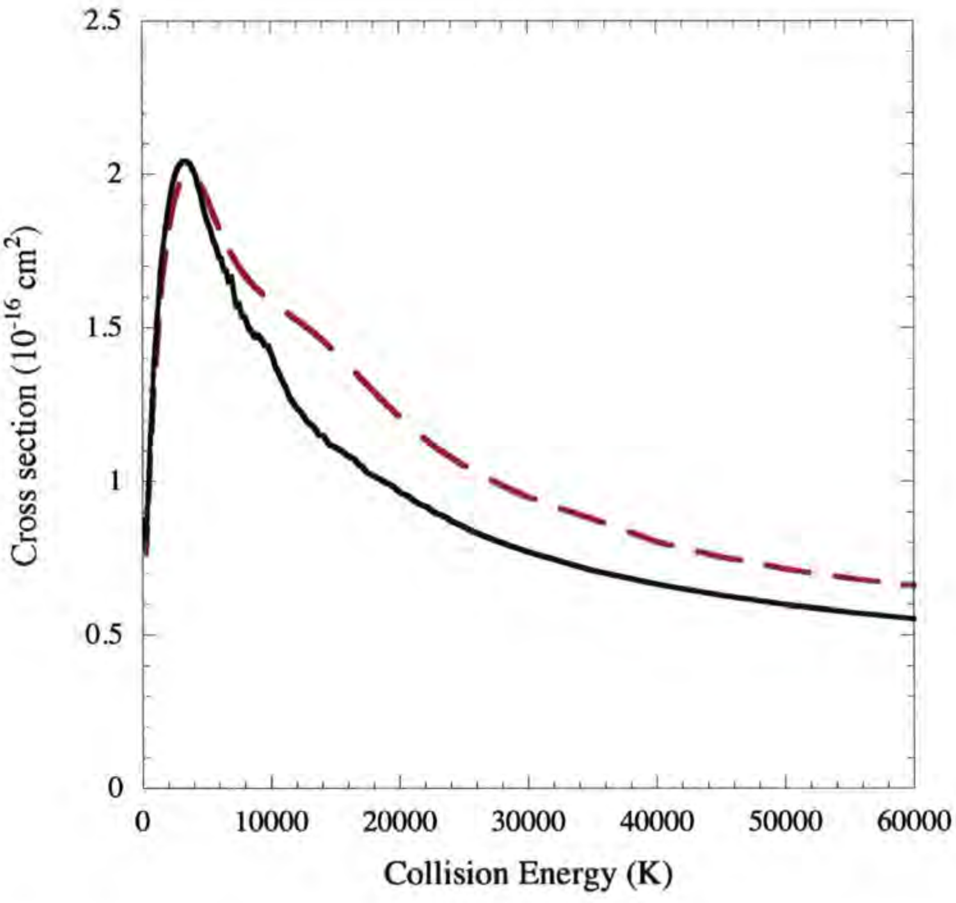

Figure 6.7: A comparison of converged results obtained for the $\nu = 0,\ j = 1 \rightarrow \nu' = 0,\ j' = 0$ transition using the SHO (broken curve) and ENCO (full curve) functions. The interaction potential of Mielke *et al.* [39] was used in these calculations and a basis set comprising all states of HD up to and including $\nu = 5, j = 11$.

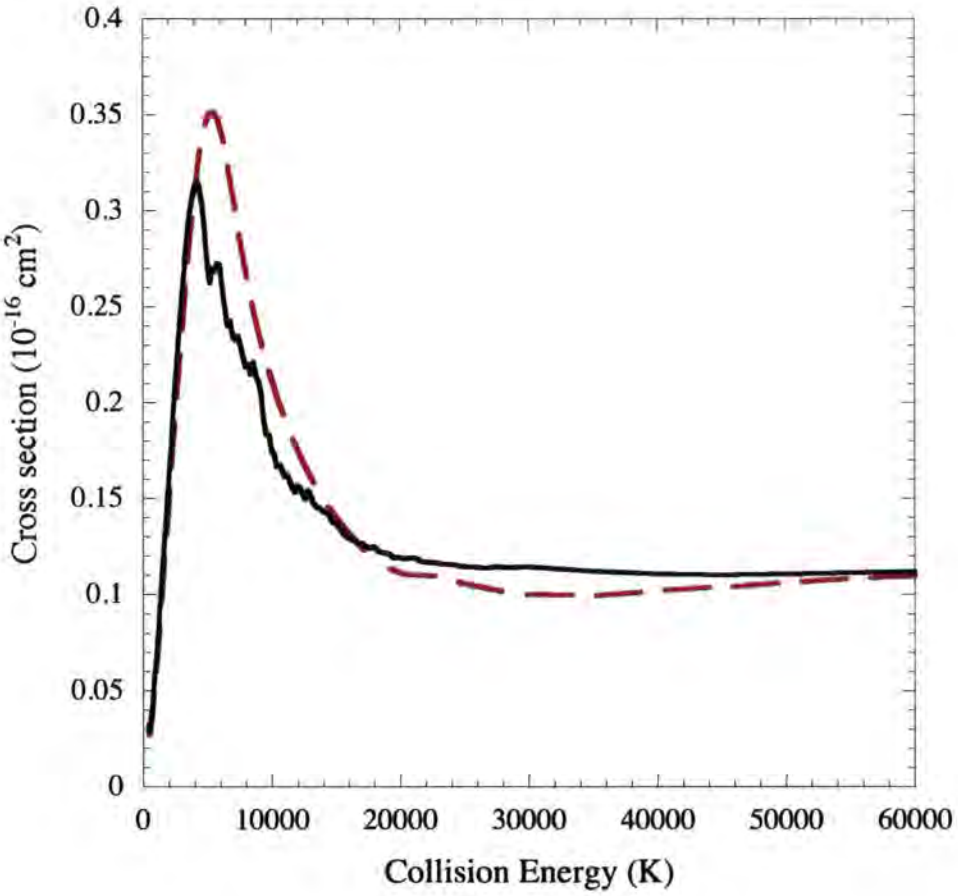

Figure 6.8: A comparison of converged results obtained for the $\nu = 0,\ j = 2 \rightarrow \nu' = 0,\ j' = 0$ transition using the SHO (broken curve) and ENCO (full curve) functions. The interaction potential of Mielke *et al.* [39] was used in these calculations and a basis set comprising all states of HD up to and including $\nu = 5, j = 11$.

increase in cross sections, at the highest energies, could hint at a possible divergence problem. Further calculations, at higher energies, would need to be performed to see if the cross section decreases in magnitude. The $\Delta j = 1$ cross section is, again, several factors larger than the $\Delta j = 2$ case. The magnitude of the $\nu = 1,\ j = 2 \rightarrow \nu' = 0,\ j' = 0$ cross section is comparable to the corresponding cross section in H+H_2 .

Cross sections for the $\nu = 3,\ j = 7 \rightarrow \nu' = 3,\ j' = 5$ transition are shown in Figure 6.11. In this case there are substantial differences in the cross sections, obtained for the SHO and ENCO models, at energies near and increasing from threshold.

In Figure 6.12 a $\Delta j = 3$ transition is shown. In comparison to the $\Delta j = 2$ transitions shown in Figures 6.8 and 6.11 the overall magnitude of the cross section is smaller. This is anticipated as the the magnitude of the cross sections typically reduce with increasing Δj. The cross section for $\nu = 1,\ j = 3 \rightarrow \nu' = 1,\ j' = 0$ shows good agreement between the vibrational models at energies near threshold. This may be due to the low vibrational quantum number, $\nu = 1$, present in the initial and final states.

Figure 6.13 shows cross sections for the $\nu = 4,\ j = 2 \rightarrow \nu' = 2,\ j' = 0$ transition. There are considerable discrepancies between the ENCO and SHO models at low energies and near threshold. At high energies the cross section for the ENCO model continues to increase. However, the corresponding cross section for the SHO case begins to decrease. If calculations for the ENCO model are performed at higher collision energies we may expect its cross section to decrease too.

In Figure 6.14 the rovibrationally inelastic cross section for the $\nu = 4,\ j = 6 \rightarrow \nu' = 1,\ j' = 3$ transition is plotted. The cross section obtained using the ENCO model is larger for all energies than that obtained for the SHO model. The largest discrepancies occur at low energies. In this rovibrational transition the cross section for both models is decreasing at high energies.

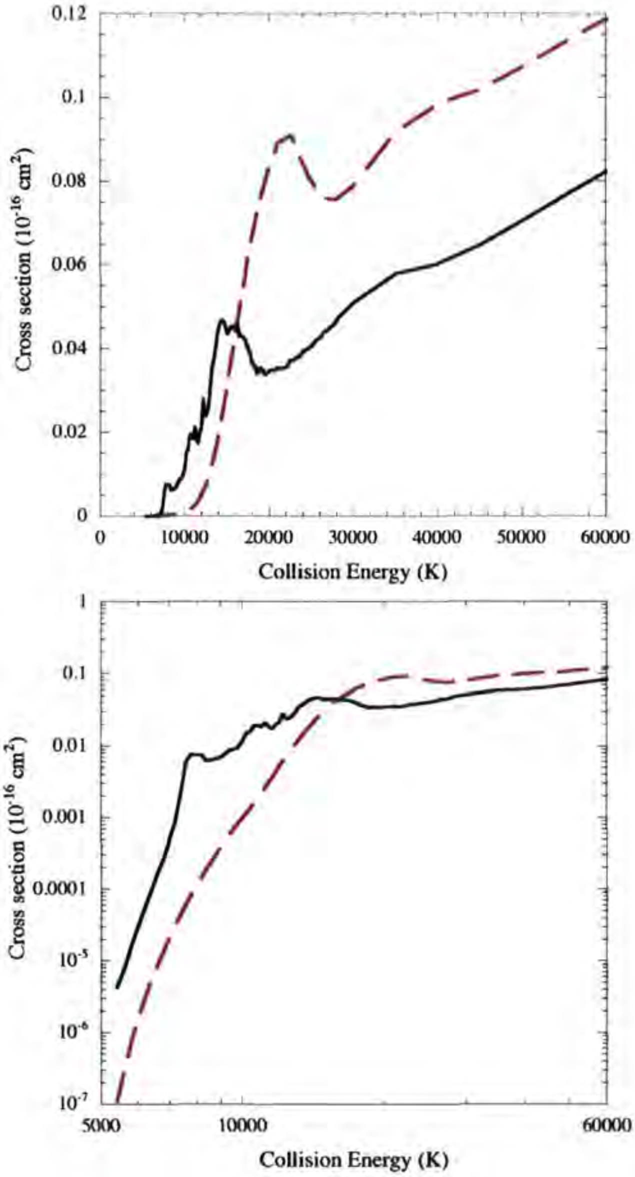

Figure 6.9: A comparison of results obtained for the $\nu = 1,\ j = 1 \rightarrow \nu' = 0,\ j' = 0$ transition using the SHO (broken curve) and ENCO (full curve) functions. The interaction potential of Mielke *et al.* [39] was used in these calculations and a basis set comprising all states of HD up to and including $\nu = 5, j = 11$.

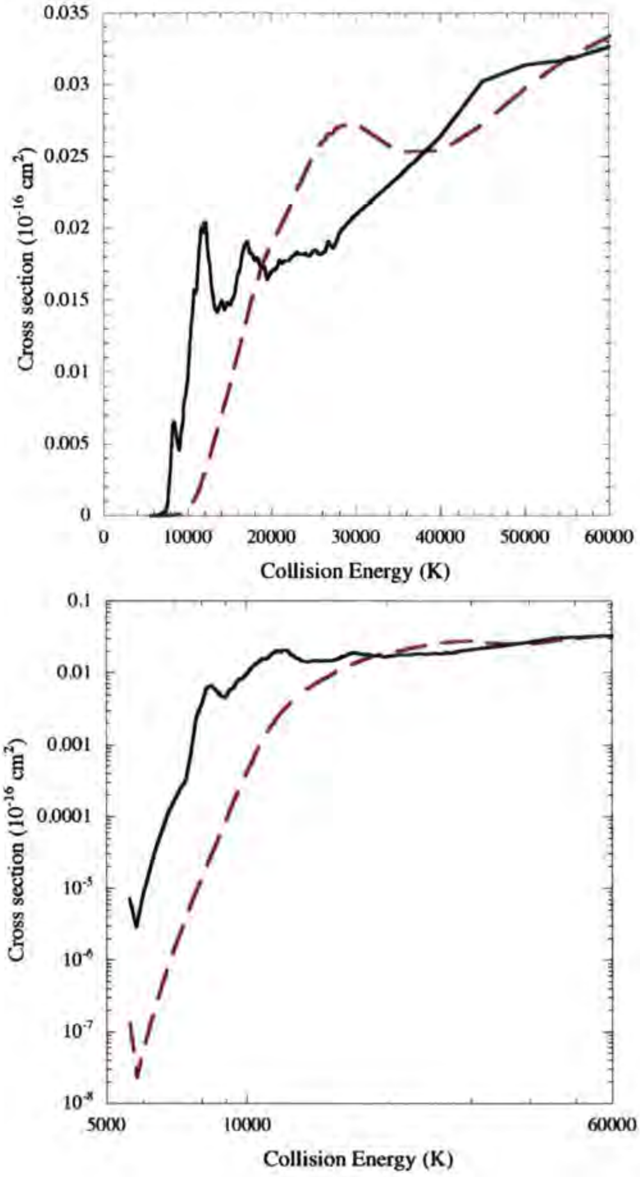

Figure 6.10: A comparison of results obtained for the $\nu = 1,\ j = 2 \rightarrow \nu' = 0,\ j' = 0$ transition using the SHO (broken curve) and ENCO (full curve) functions. The interaction potential of Mielke *et al.* [39] was used in these calculations and a basis set comprising all states of HD up to and including $\nu = 5, j = 11$.

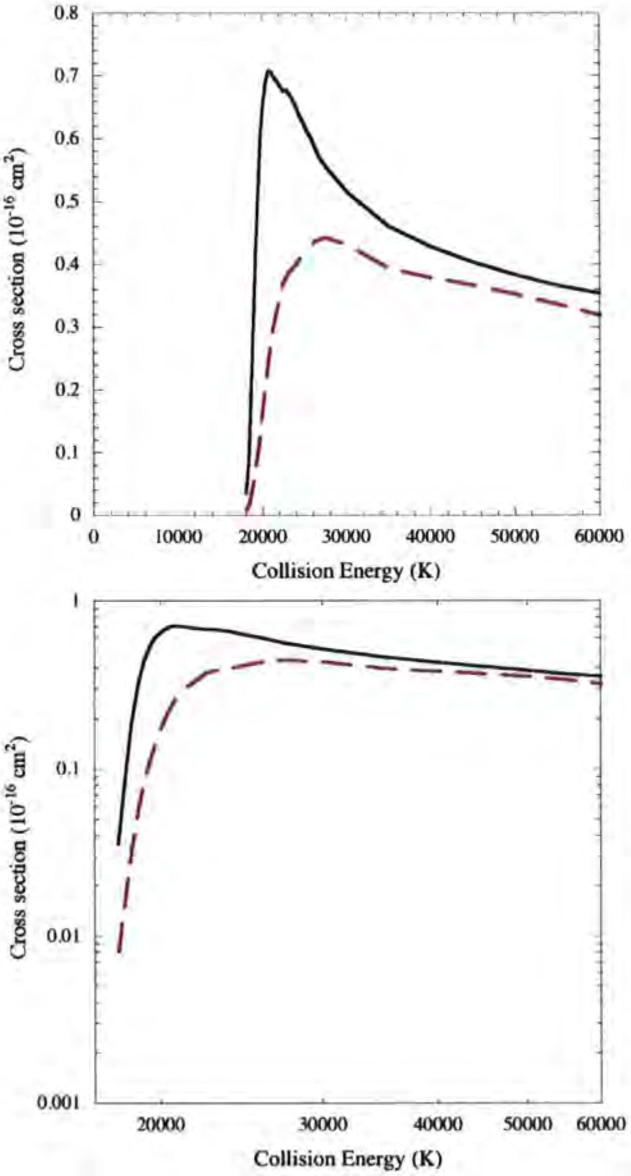

Figure 6.11: A comparison of results obtained for the $\nu = 3,\ j = 7 \rightarrow \nu' = 3,\ j' = 5$ transition using the SHO (broken curve) and ENCO (full curve) functions. The interaction potential of Mielke *et al.* [39] was used in these calculations and a basis set comprising all states of HD up to and including $\nu = 5, j = 11$.

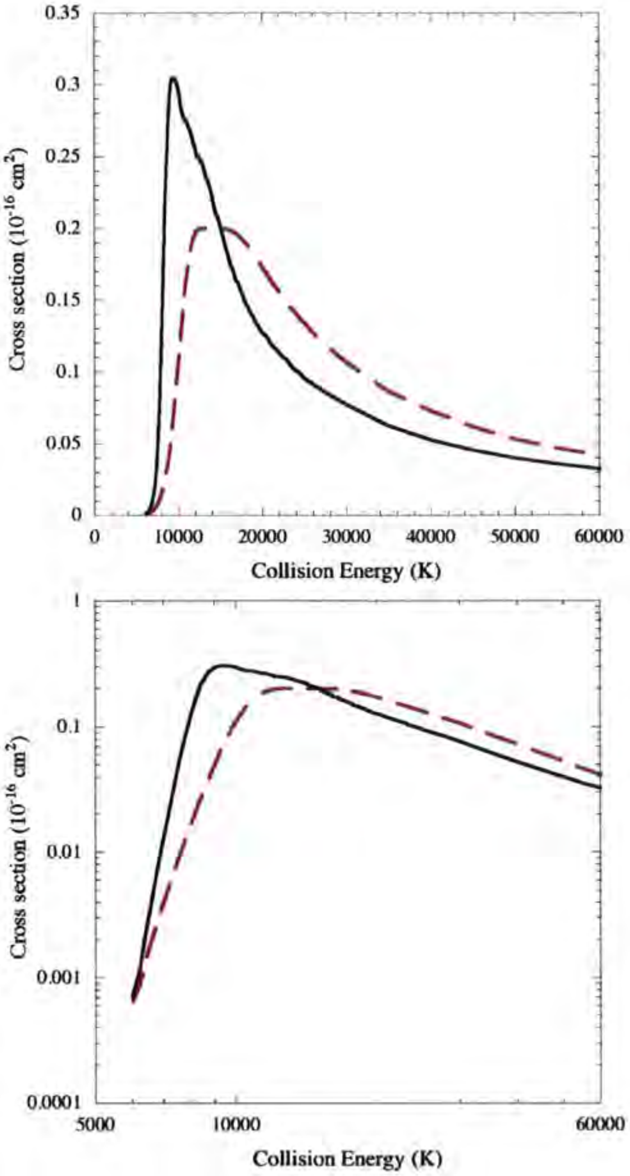

Figure 6.12: A comparison of results obtained for the $\nu = 1,\ j = 3 \rightarrow \nu' = 1,\ j' = 0$ transition using the SHO (broken curve) and ENCO (full curve) functions. The interaction potential of Mielke *et al.* [39] was used in these calculations and a basis set comprising all states of HD up to and including $\nu = 5, j = 11$.

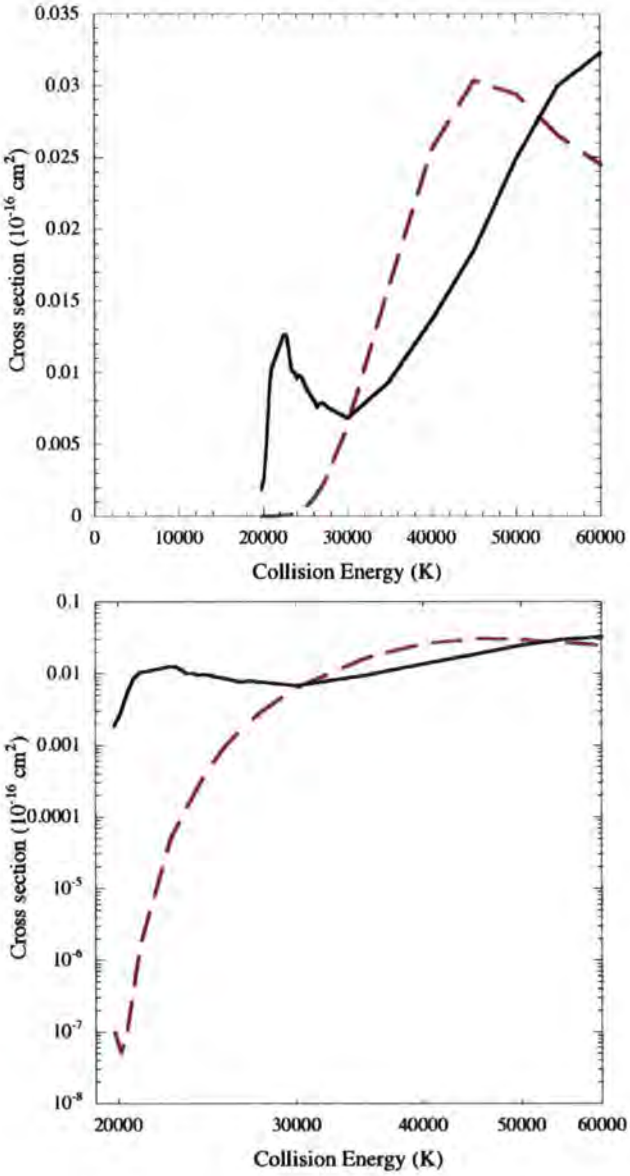

Figure 6.13: A comparison of results obtained for the $\nu = 4,\ j = 2 \rightarrow \nu' = 2,\ j' = 0$ transition using the SHO (broken curve) and ENCO (full curve) functions. The interaction potential of Mielke *et al.* [39] was used in these calculations and a basis set comprising all states of HD up to and including $\nu = 5, j = 11$.

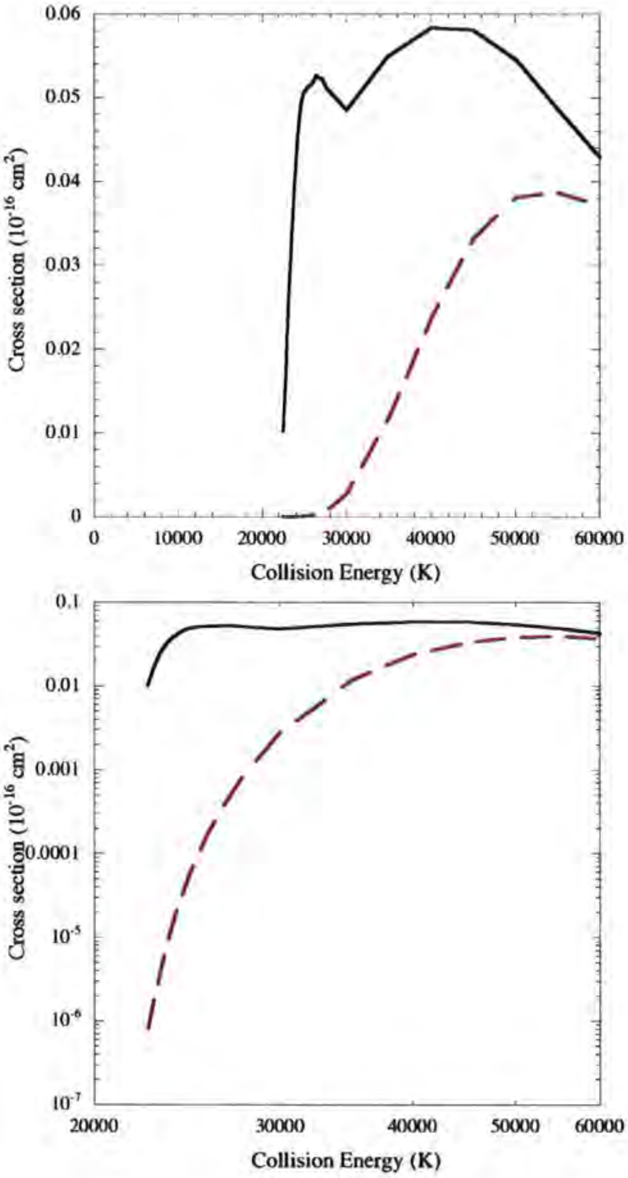

Figure 6.14: A comparison of results obtained for the $\nu = 4,\ j = 6 \rightarrow \nu' = 1,\ j' = 3$ transition using the SHO (broken curve) and ENCO (full curve) functions. The interaction potential of Mielke *et al.* [39] was used in these calculations and a basis set comprising all states of HD up to and including $\nu = 5, j = 11$.

Comparison of cross sections between different representations of the interaction potential for H+HD

The cross sections for H+HD are now compared using the interaction potentials of Boothroyd *et al.* [38] and Mielke *et al.* [39]. The cross sections examined here, are the same as those transitions examined when investigating the vibrational representations of the molecule, HD. For these calculations the ENCO model is used.

The pure rotationally inelastic transitions are considered first. In Figure 6.15 cross sections are compared for the $\nu = 0,\ j = 1 \rightarrow \nu' = 0,\ j' = 0$ transition. There is good agreement between the cross sections for each potential.

Figures 6.16 and 6.17 show cross sections for $\Delta j = 2$ transitions. Again, cross sections obtained using the two potentials are are in good agreement with each other. Small discrepancies did occur between the cross sections at higher energies.

The cross section corresponding to the $\nu = 1,\ j = 3 \rightarrow \nu' = 1,\ j' = 0$ transition is shown in Figure 6.18. Large discrepancies between cross sections obtained using each potential occur near threshold. The cross sections for the potential of Boothroyd *et al.* [38] peak at a larger value.

For the pure rotationally inelastic transitions, in H+HD, there is reasonable agreement between cross sections obtained using each interaction potential. In the cases where there are significant discrepancies, the cross sections obtained from Boothroyd *et al.* [38] typically gives the larger values.

Larger discrepancies were found between cross sections obtained from each interaction potential, for rovibrationally inelastic transitions. Figure 6.19 shows cross sections for the $\nu = 1,\ j = 1 \rightarrow \nu' = 0,\ j' = 0$ transition. At low and high collision energies there is reasonable agreement between cross sections obtained from each potential. The cross sections continue to increase at higher energies for both potentials.

In Figure 6.20 cross sections for the $\nu = 1,\ j = 2 \rightarrow \nu' = 0,\ j' = 0$ transition are shown whilst those for the $\nu = 4,\ j = 2 \rightarrow \nu' = 2,\ j' = 0$ transition are shown in Figure 6.21. For both transitions there is excellent agreement between cross sections obtained from each potential at low collision energies.

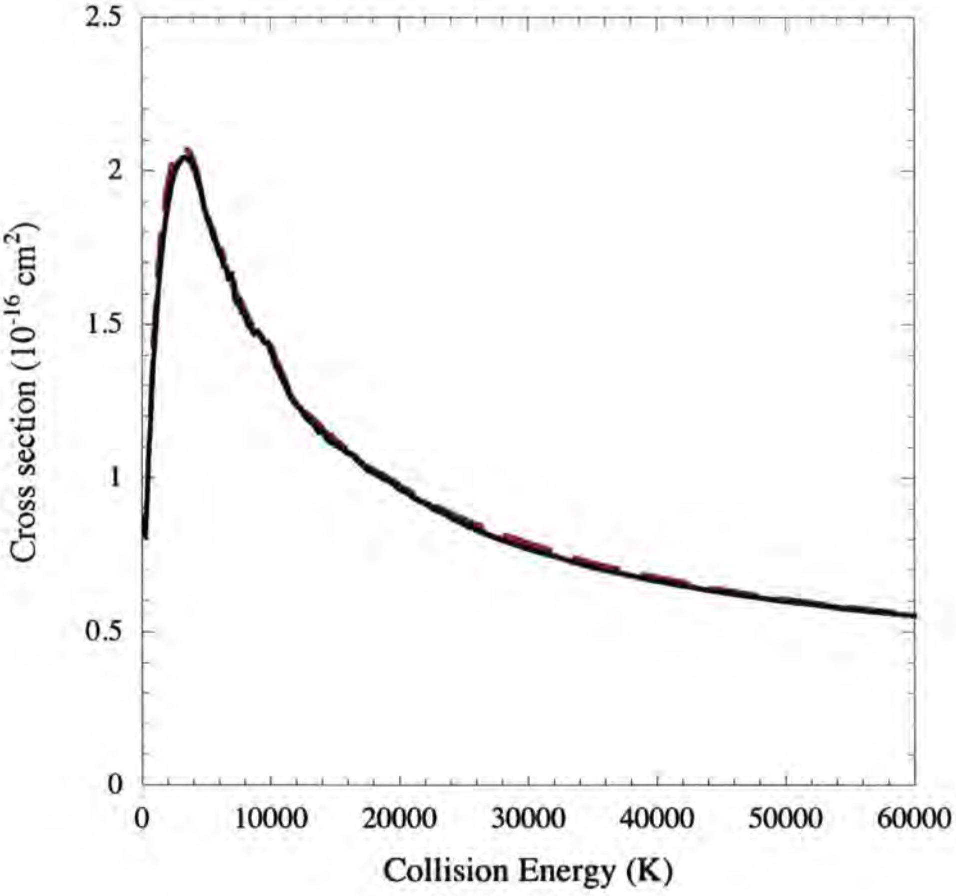

Figure 6.15: A comparison of converged results obtained for the $\nu = 0,\ j = 1 \rightarrow \nu' = 0,\ j' = 0$ transition using the potentials of Boothroyd *et al.* [38] (broken curve) and Mielke *et al.* [39] (full curve). The ENCO vibrational functions were employed in these calculations and a basis set comprising all states of HD up to and including $\nu = 5, j = 11$.

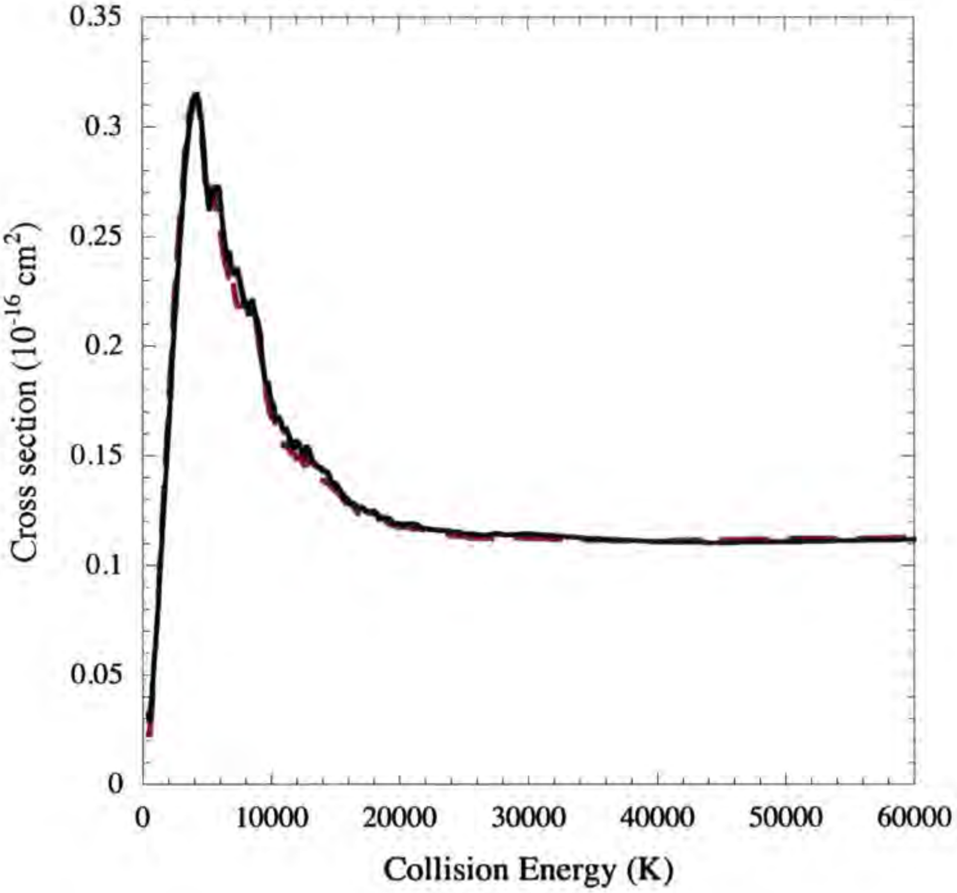

Figure 6.16: A comparison of converged results obtained for the $\nu = 0,\ j = 2 \to \nu' = 0,\ j' = 0$ transition using the potentials of Boothroyd *et al.* [38] (broken curve) and Mielke *et al.* [39] (full curve). The ENCO vibrational functions were employed in these calculations and a basis set comprising all states of HD up to and including $\nu = 5, j = 11$.

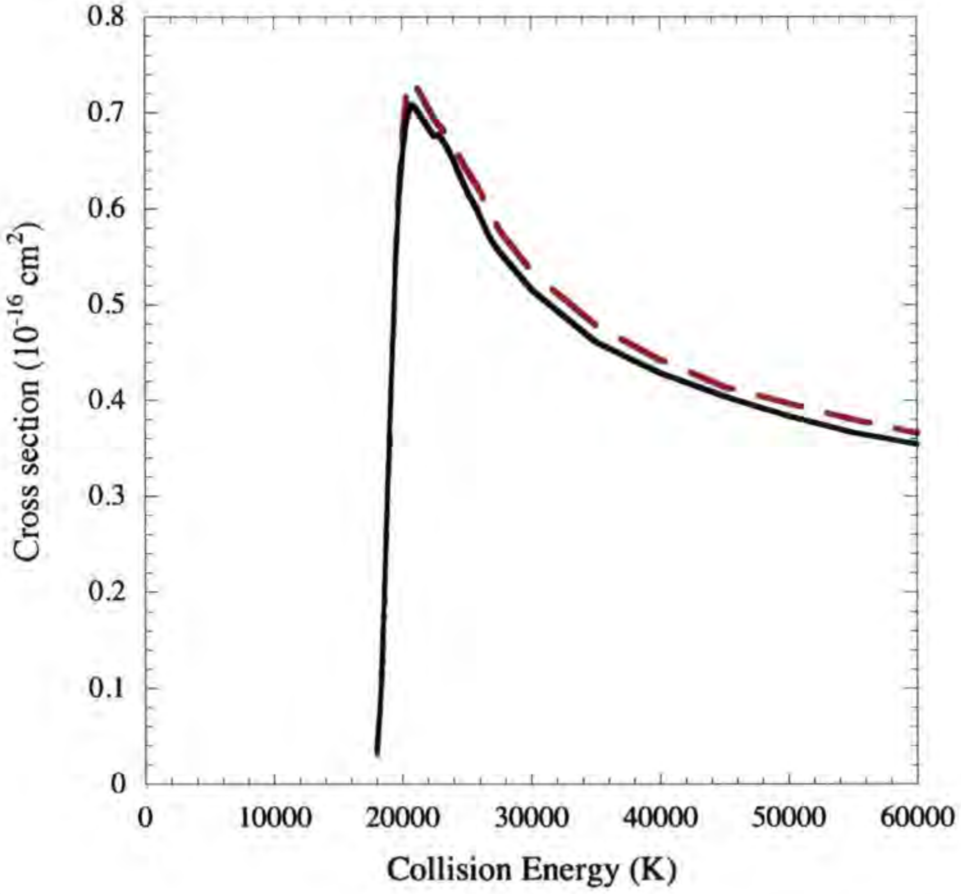

Figure 6.17: A comparison of results obtained for the $\nu = 3,\ j = 7 \rightarrow \nu' = 3,\ j' = 5$ transition using the potentials of Boothroyd *et al.* [38] (broken curve) and Mielke *et al.* [39] (full curve). The ENCO vibrational functions were employed in these calculations and a basis set comprising all states of HD up to and including $\nu = 5, j = 11$.

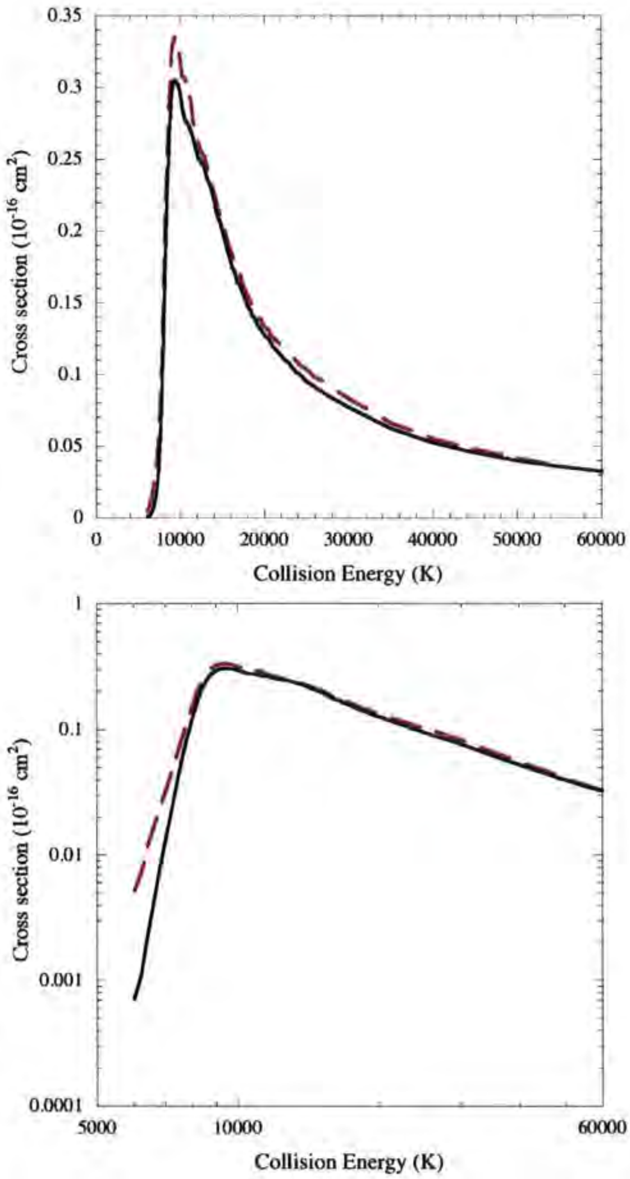

Figure 6.18: A comparison of results obtained for the $\nu = 1,\ j = 3 \rightarrow \nu' = 1,\ j' = 0$ transition using the potentials of Boothroyd *et al.* [38] (broken curve) and Mielke *et al.* [39] (full curve). The ENCO vibrational functions were employed in these calculations and a basis set comprising all states of HD up to and including $\nu = 5, j = 11$.

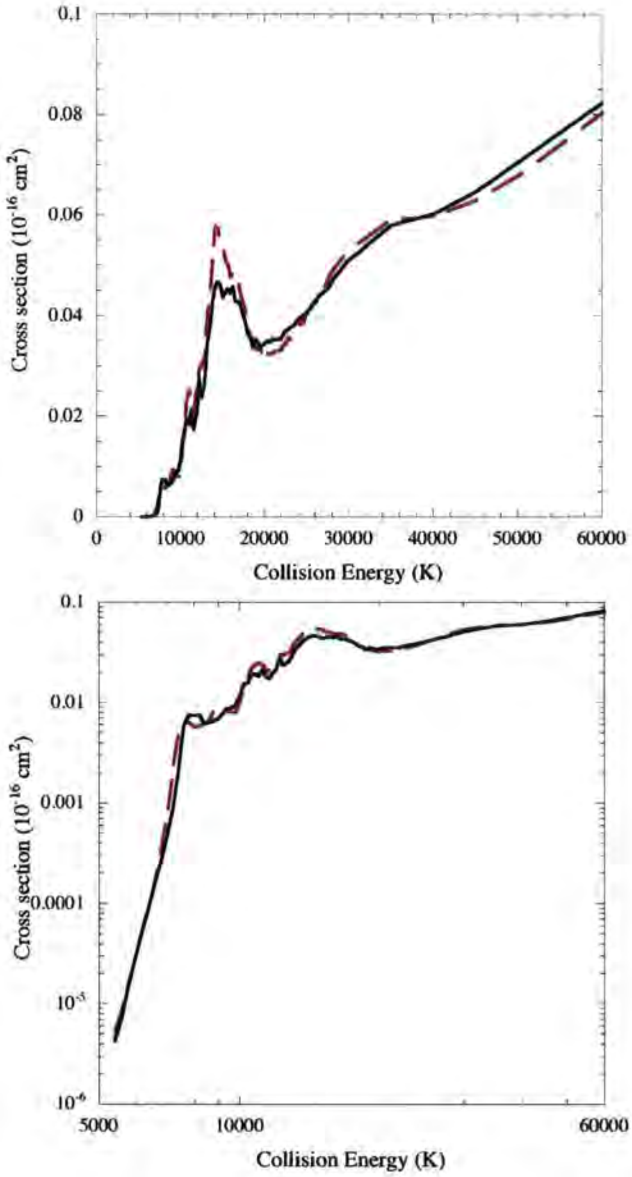

Figure 6.19: A comparison of results obtained for the $\nu = 1,\ j = 1 \rightarrow \nu' = 0,\ j' = 0$ transition using the potentials of Boothroyd *et al.* [38] (broken curve) and Mielke *et al.* [39] (full curve). The ENCO vibrational functions were employed in these calculations and a basis set comprising all states of HD up to and including $\nu = 5, j = 11$.

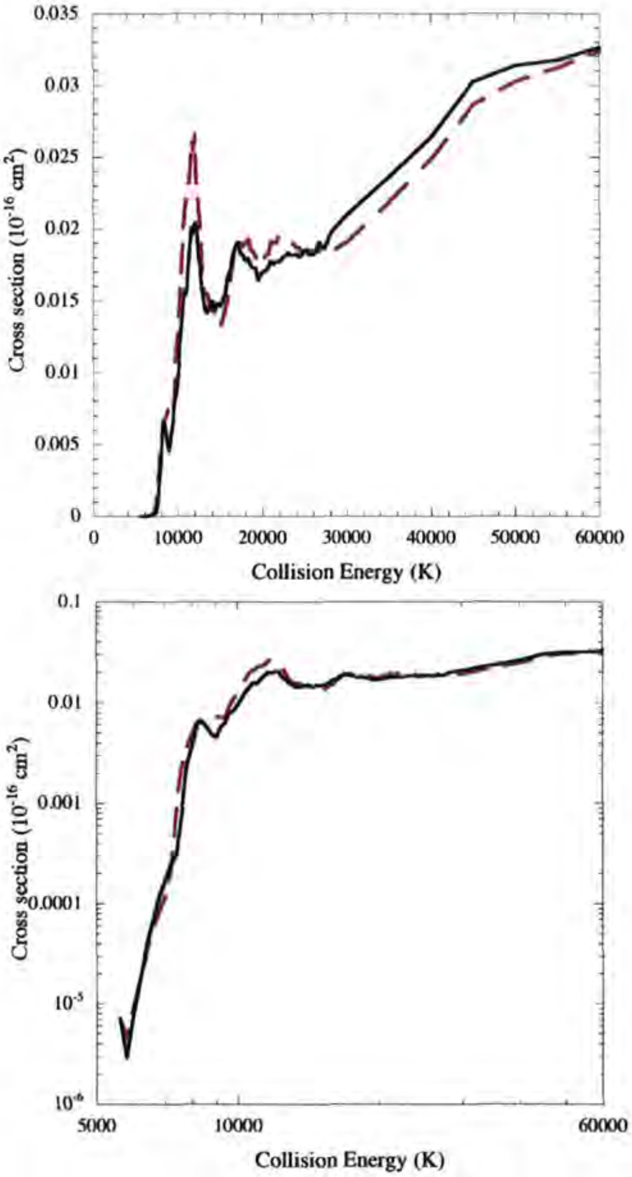

Figure 6.20: A comparison of results obtained for the $\nu = 1,\ j = 2 \rightarrow \nu' = 0,\ j' = 0$ transition using the potentials of Boothroyd *et al.* [38] (broken curve) and Mielke *et al.* [39] (full curve). The ENCO vibrational functions were employed in these calculations and a basis set comprising all states of HD up to and including $\nu = 5, j = 11$.

Discrepancies emerge at higher energies; the cross sections for the potential of Mielke *et al.* [39] are larger for the highest energies, although those for Boothroyd *et al.* [38] tend to be larger at lower energies. These cross sections continue to increase at the highest collision energies.

Figure 6.22 shows the cross sections for the $\nu = 4,\ j = 6 \rightarrow \nu' = 1,\ j' = 3$ transition. There is good agreement between cross sections obtained from each potential for low and high collision energies. The cross sections obtained using the potential of Boothroyd *et al.* [38] are larger than those for Mielke *et al.* [39] for collision energies of 25000–50000 K.

6.3.1 Summary of cross sections for H+HD

- Cross sections have been presented for rovibrationally inelastic transitions in H+HD using the quantum mechanical coupled–channels method.

- The convergence of the cross sections with respect to the extent of the basis of rovibrational states was investigated carefully. Convergence was found to be slow, with couplings to states with vibrational quantum number $\nu \geq 6$ being significant. As for the case of H+H_2 (see section 5.3.4), this may be due to reactive scattering states being neglected from the basis set.

- Considerable differences were found between cross sections calculated for different vibrational representations of the molecule. The SHO model of the vibrational motion was found to be unsatisfactory particularly with regard to the predicted rate of increase from threshold of cross sections for vibrationally inelastic transitions.

- Cross sections obtained using the ENCO and model displayed considerably more structure than those obtained using the SHO model.

- There was reasonable agreement between cross sections calculated using the potential of Mielke *et al.* [39] and Boothroyd *et al.* [38] for most collision energies.

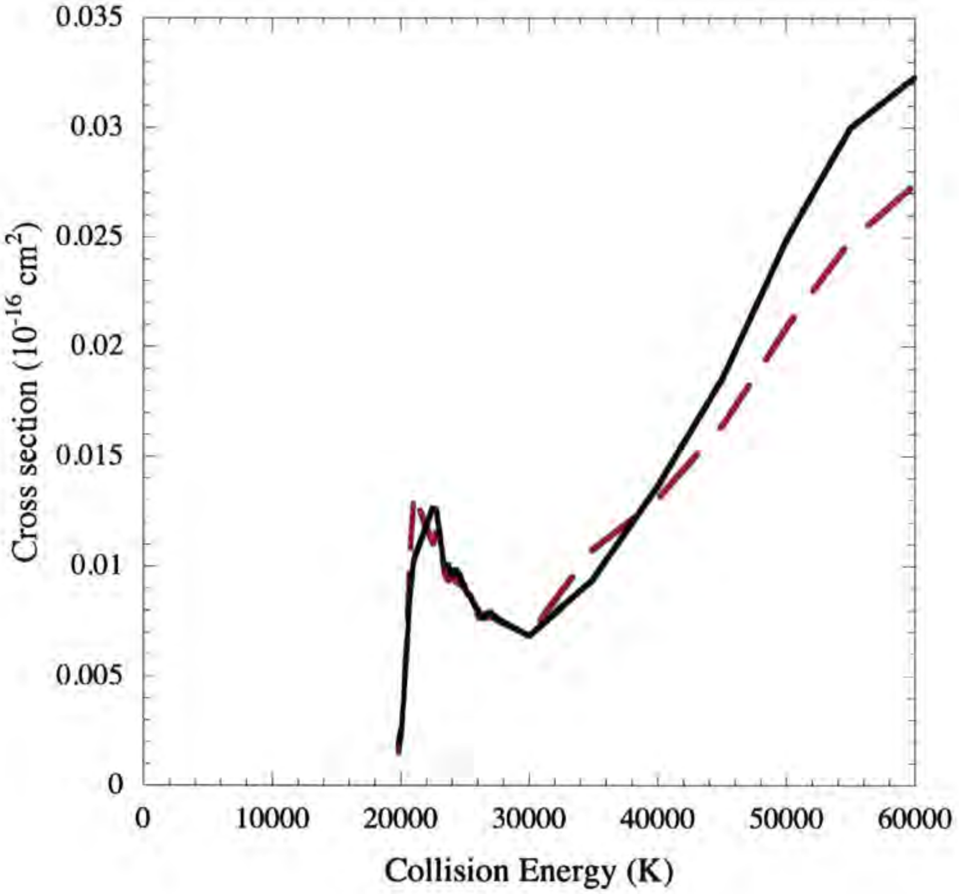

Figure 6.21: A comparison of results obtained for the $\nu = 4,\ j = 2 \rightarrow \nu' = 2,\ j' = 0$ transition using the potentials of Boothroyd *et al.* [38] (broken curve) and Mielke *et al.* [39] (full curve). The ENCO vibrational functions were employed in these calculations and a basis set comprising all states of HD up to and including $\nu = 5, j = 11$.

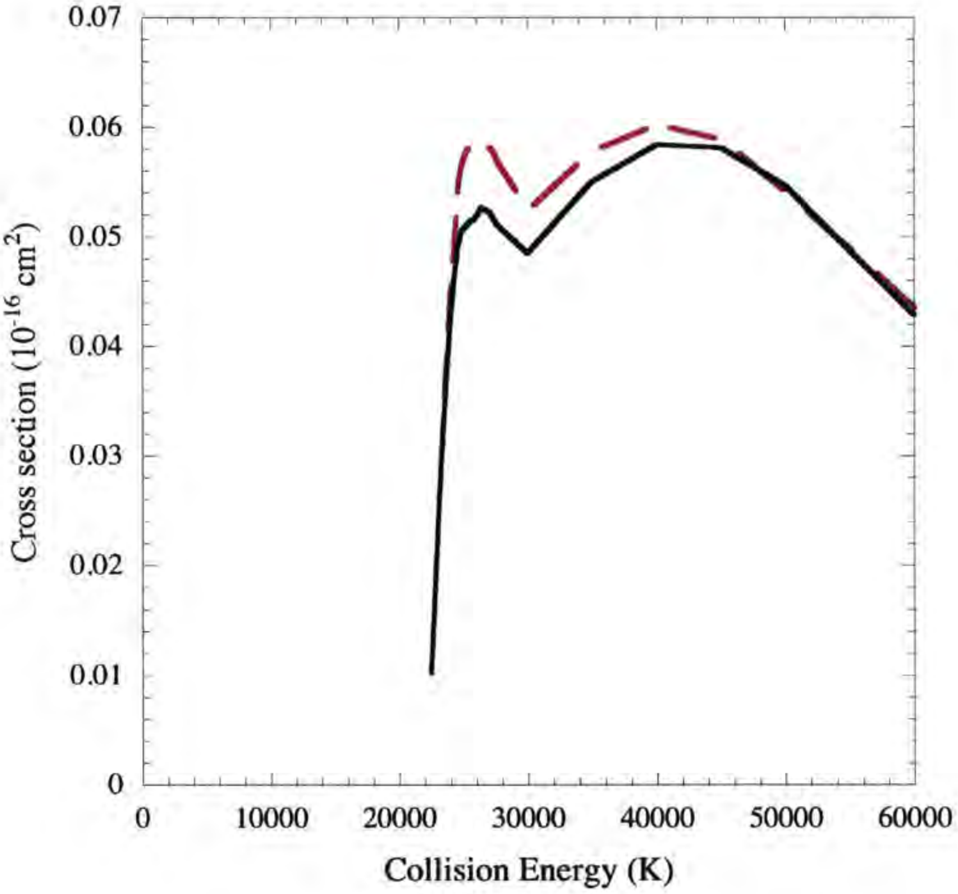

Figure 6.22: A comparison of results obtained for the $\nu = 4,\ j = 6 \rightarrow \nu' = 1,\ j' = 3$ transition using the potentials of Boothroyd *et al.* [38] (broken curve) and Mielke *et al.* [39] (full curve). The ENCO vibrational functions were employed in these calculations and a basis set comprising all states of HD up to and including $\nu = 5, j = 11$.

- At high collision energies cross sections obtained for several rovibrationally inelastic transitions continued to increase. Future calculations at higher collision energies may be required to ensure there is no problem of divergence in the cross sections.

6.4 Rate Coefficients

In order to obtain rate coefficients as functions of the kinetic temperature, T, the cross sections are integrated over a Maxwellian velocity distribution (see equation (2.90)). When calculating the rate coefficients care was taken to ensure the grid of collision energies was adapted to the opening of new thresholds, and other effects, which cause rapid variation in the cross sections as a function of barycentric collision energy. However due to the increased structure observed when the ENCO representation is used it can become difficult to incorporate every feature for all transitions.

The rate coefficients were computed numerically on a grid of temperatures extending from 0 K to 6000 K at every 100 K. Only a subset of the rate coefficients are presented in this thesis. A complete collection of rate coefficients can be found at http://ccp7.dur.ac.uk.

Comparison of rate coefficients between different representations of the vibrational motion of the molecule

Rate coefficients for pure rotationally inelastic transitions calculated using the SHO and ENCO models are considered first.

Figure 6.23a shows a comparison of the rate coefficients for the $\nu = 0,\ j = 1 \rightarrow \nu' = 0,\ j' = 0$ transition. There is reasonable agreement between the vibrational models at low temperatures. At higher temperatures the rate coefficient for the SHO model is moderately larger.

In Figure 6.23b rate coefficients for the $\nu = 0,\ j = 2 \rightarrow \nu' = 0,\ j' = 0$ transition are shown. There is good agreement between the SHO and ENCO models at low temperatures. At higher temperatures there are small discrepancies.

Rate coefficients are shown for the $\nu = 3,\ j = 7 \rightarrow \nu' = 3,\ j' = 5$ transition, using the ENCO and SHO models, are shown in Figure 6.23c. There are considerable discrepancies between the two vibrational models at low temperatures. At higher temperatures the size of the discrepancy reduces. The rate coefficient for the ENCO model is larger over the entire temperature range calculations were performed for.

Rate coefficients for a $\Delta j = 3$ transition are shown in Figure 6.23d. There is reasonable agreement between the vibrational models at the lowest temperatures. Discrepancies begin to emerge as the temperature is increased. The magnitude of the rate coefficient for the ENCO model is greater for all considered temperatures.

The rotationally inelastic transitions considered above show that as the size of Δj increases, the magnitude of the rate coefficient reduces. This trend is observable in their corresponding cross sections and relates to the convergence in the expansion of the interaction potential (see equation 5.1).

The rovibrationally inelastic cross sections calculated for H+HD exhibited large discrepancies, between which vibrational model is used, near threshold and for most of the collision energy range. Therefore, large discrepancies are expected in the rate coefficients too.

In Figure 6.24a and Figure 6.24b, rate coefficients are shown for transitions with $\Delta\nu = 1$. There are large discrepancies, between the vibrational models, at low temperatures where the ENCO model gives a larger magnitude for the rate coefficient in both transitions. The discrepancies are larger in Figure 6.24b although the magnitude of the rate coefficient is smaller as it is a $\Delta j = 2$ transition. The rate coefficient in Figure 6.24a corresponds to a $\Delta j = 1$ transition.

Figure 6.24c shows rate coefficients calculated for the $\nu = 4,\ j = 2 \rightarrow \nu' = 2,\ j' = 0$ transition. There are very large discrepancies, between the SHO and ENCO models, at low temperatures. The rate coefficient for the ENCO model remains larger over the entire range of calculated temperatures. However, the size of the discrepancy reduces dramatically as the temperature increases (with near agreement at $T = 6000$ K).

The rate coefficients for the $\nu = 4,\ j = 6 \rightarrow \nu' = 1,\ j' = 3$ transition

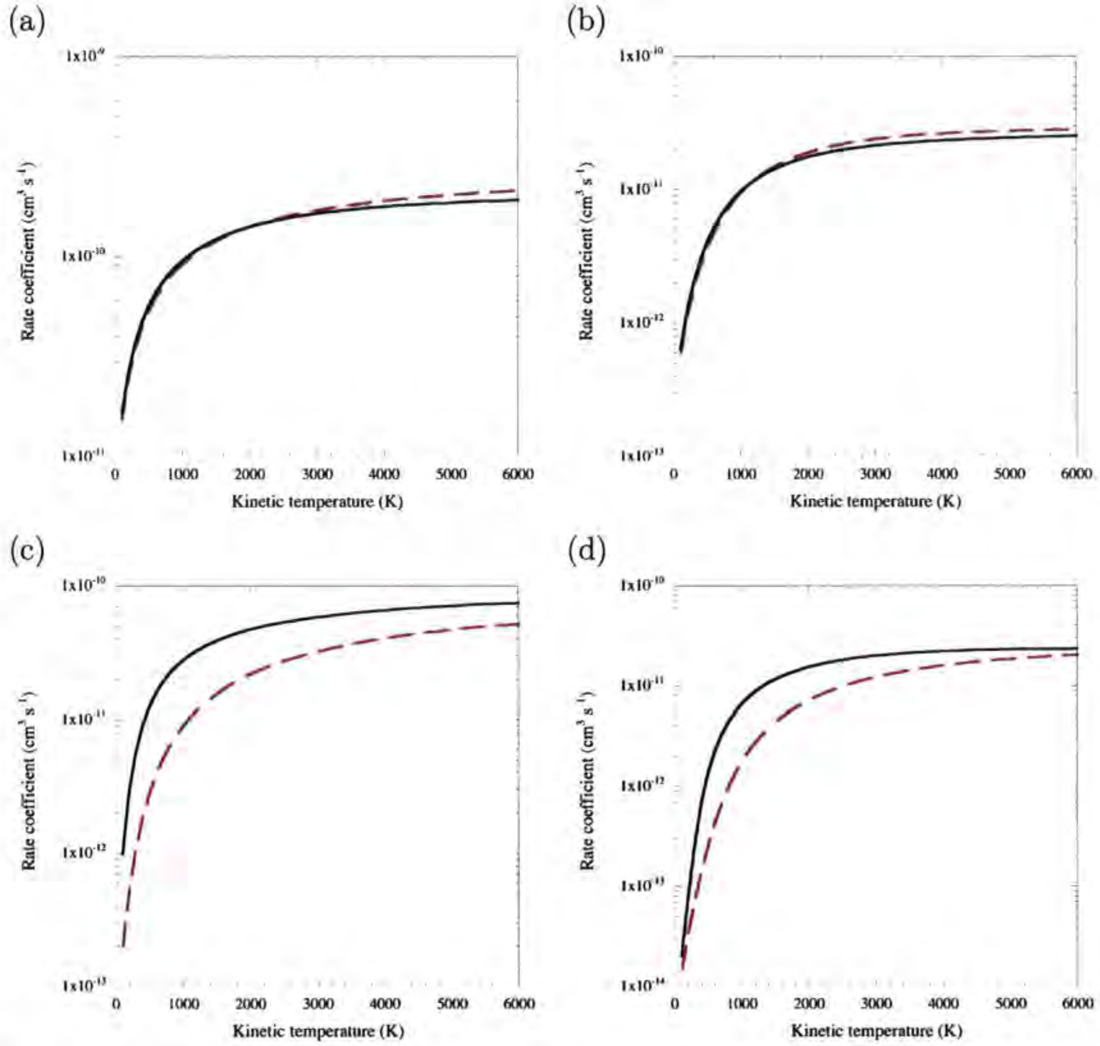

Figure 6.23: A comparison of rate coefficients, as a function of kinetic temperature T, obtained for the for the (a) $\nu = 0,\ j = 1 \rightarrow \nu' = 0,\ j' = 0$, (b) $\nu = 0,\ j = 2 \rightarrow \nu' = 0,\ j' = 0$, (c) $\nu = 3,\ j = 7 \rightarrow \nu' = 3,\ j' = 5$, (d) $\nu = 1,\ j = 3 \rightarrow \nu' = 1,\ j' = 0$ transitions using the SHO and ENCO models, H+HD. The interaction potential of Mielke *et al.* [39] was used in these calculations.

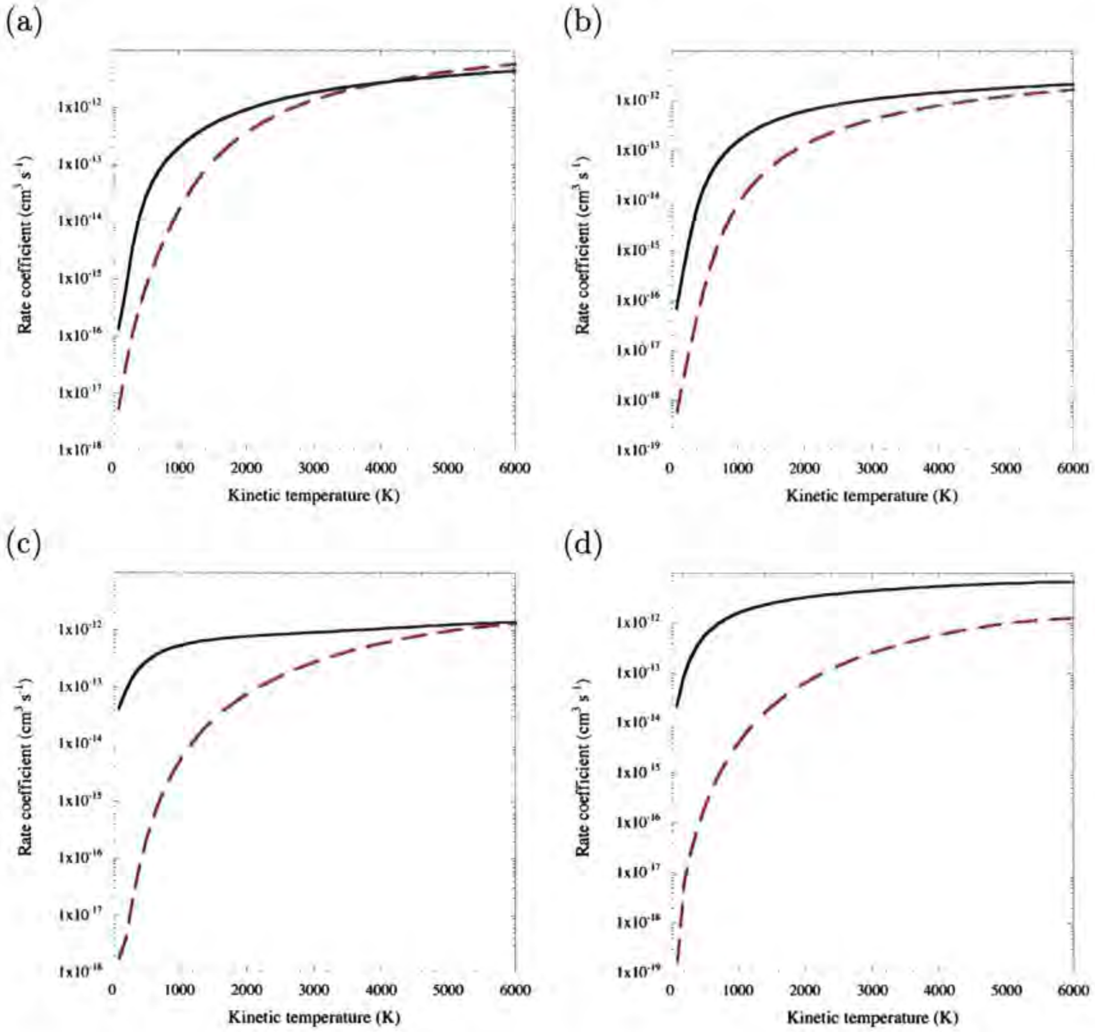

Figure 6.24: A comparison of rate coefficients, as a function of kinetic temperature T, obtained for the for the (a) $\nu = 1,\ j = 1 \rightarrow \nu' = 0,\ j' = 0$, (b) $\nu = 1,\ j = 2 \rightarrow \nu' = 0,\ j' = 0$, (c) $\nu = 4,\ j = 2 \rightarrow \nu' = 2,\ j' = 0$, (d) $\nu = 4,\ j = 6 \rightarrow \nu' = 1,\ j' = 3$ transitions using the SHO and ENCO models, H+HD. The interaction potential of Mielke *et al.* [39] was used in these calculations.

are shown in Figure 6.24d. There are large discrepancies between the two vibrational models at all calculated temperatures. The ENCO model rate coefficients are larger, although the magnitude of the discrepancy decreases as the temperature increases. At low temperatures the ENCO model produces a rate coefficient approximately 5 orders of magnitude greater than that of the SHO model.

The rate coefficients calculated for rovibrationally inelastic transitions, in H+HD, have larger discrepancies between the ENCO and SHO models than those found in rotationally inelastic cross sections.

Comparison of rate coefficients between different representations of the interaction potential

Rate coefficients were calculated for transitions using the interaction potentials of Mielke *et al.* [39] and Boothroyd *et al.* [38].

Figures 6.25a, 6.25b, and 6.25c show rate coefficients for pure rotationally inelastic transitions in HD. There is good agreement between rate coefficients obtained for both potentials for each transition. This is expected as there was good agreement between the corresponding cross sections for each transition. The rate coefficients for transitions corresponding to $\Delta j = 2$ are substantially smaller than those for $\Delta j = 1$, as expected.

In Figure 6.25d the rate coefficients for the $\nu = 1,\ j = 3 \rightarrow \nu' = 1,\ j' = 0$ transition are shown. The rate coefficient obtained using the potential of Boothroyd *et al.* [38] is approximately an order of magnitude larger than that obtained using the potential of Mielke *et al.* [39]. As the temperature increases the size of the discrepancy rapidly reduces.

Figures 6.26a, 6.26b, 6.26c, and 6.26d show rate coefficients, calculated using the interaction potentials of Boothroyd *et al.* [38] and Mielke *et al.* [39], for rovibrationally inelastic transitions in HD. There is reasonably good agreement between the two potentials for each of the transitions shown. Any discrepancies that are present are small in magnitude.

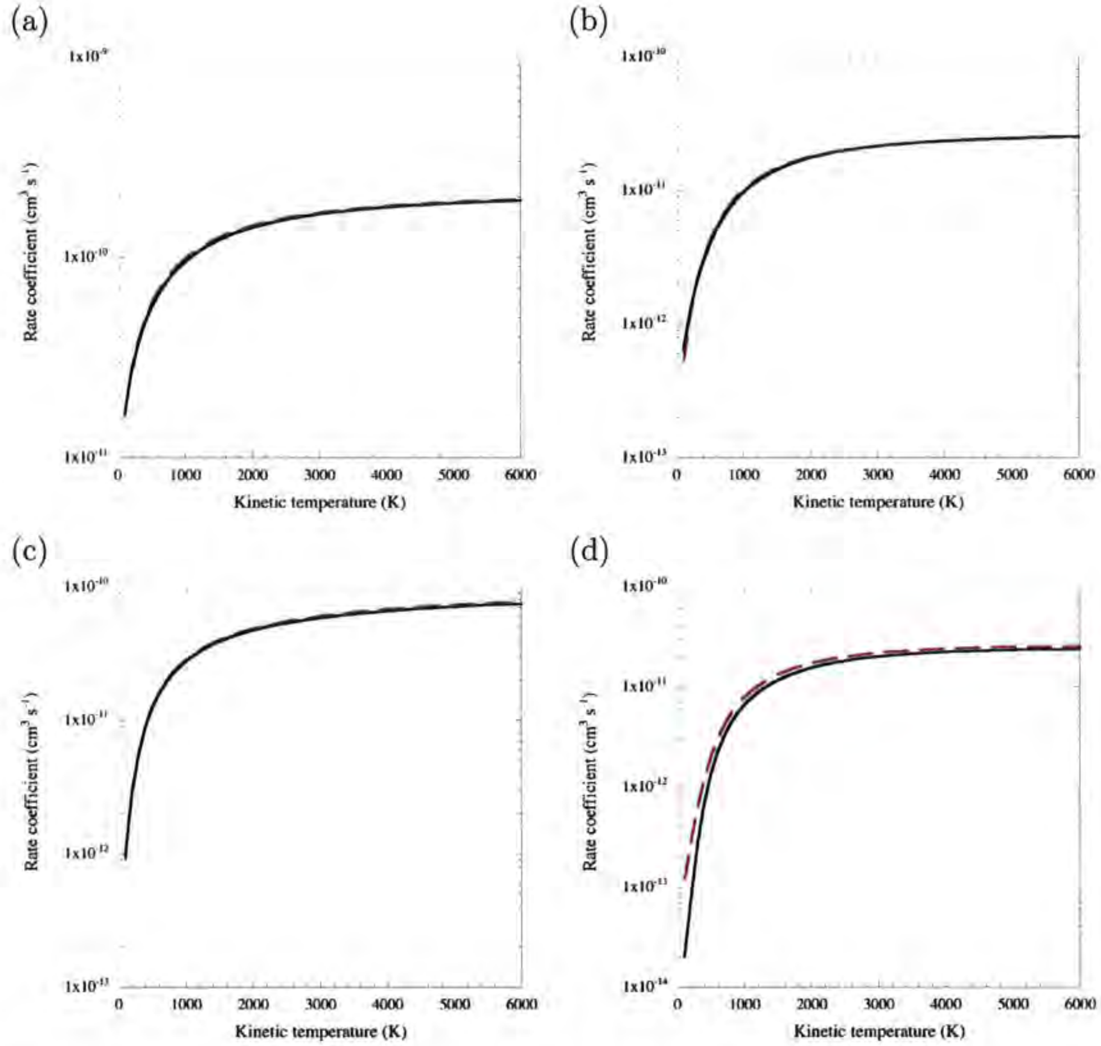

Figure 6.25: A comparison of rate coefficients, as a function of kinetic temperature T, obtained for the for the (a) $\nu = 0,\ j = 1 \rightarrow \nu' = 0,\ j' = 0$, (b) $\nu = 0,\ j = 2 \rightarrow \nu' = 0,\ j' = 0$, (c) $\nu = 3,\ j = 7 \rightarrow \nu' = 3,\ j' = 5$, (d) $\nu = 1,\ j = 3 \rightarrow \nu' = 1,\ j' = 0$ transitions, for H+HD, using the potentials of Boothroyd *et al.* [38] (broken curve) and Mielke *et al.* [39] (full curve). The ENCO vibrational functions were employed in these calculations.

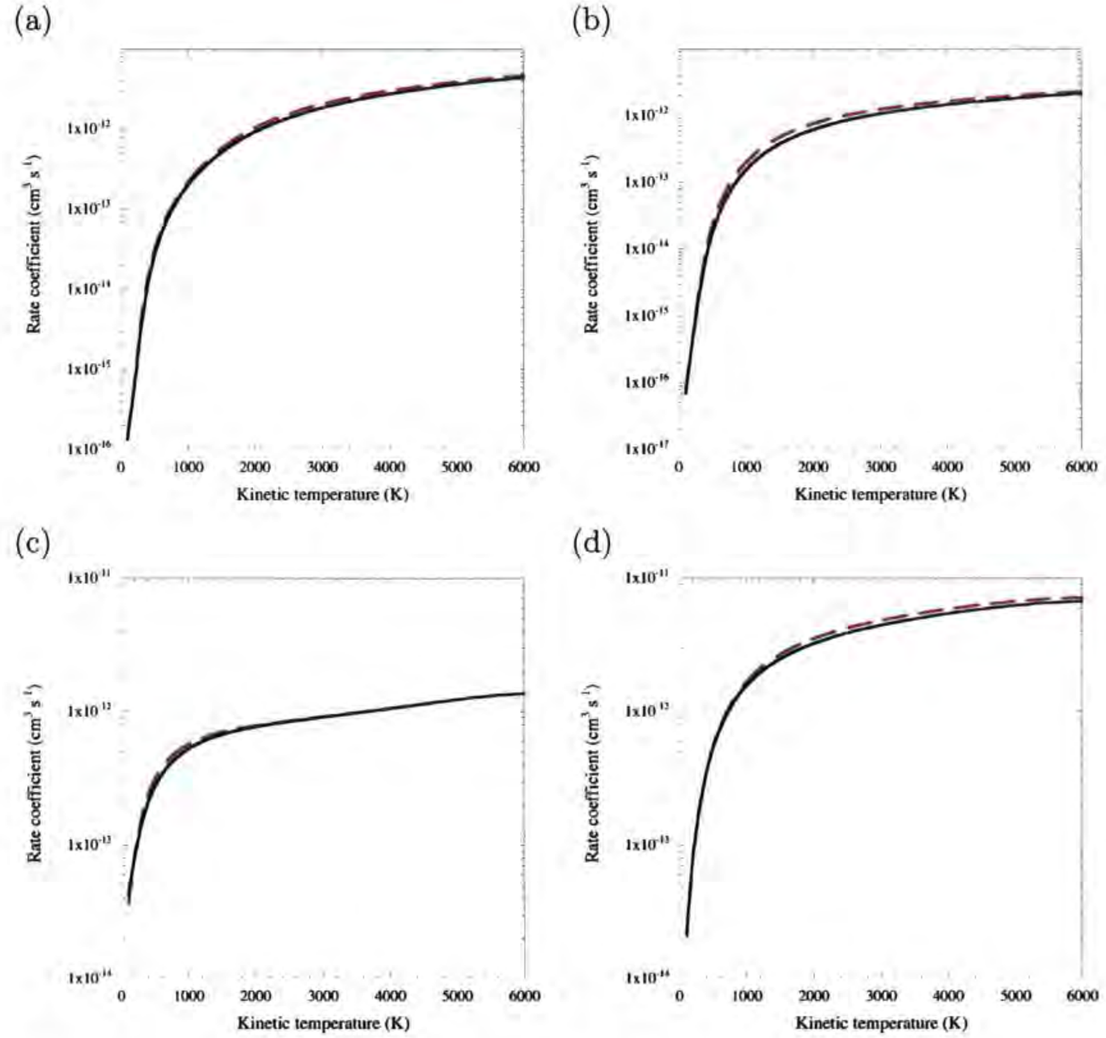

Figure 6.26: A comparison of rate coefficients, as a function of kinetic temperature T, obtained for the for the (a) $\nu = 1,\ j = 1 \rightarrow \nu' = 0,\ j' = 0$, (b) $\nu = 1,\ j = 2 \rightarrow \nu' = 0,\ j' = 0$, (c) $\nu = 4,\ j = 2 \rightarrow \nu' = 2,\ j' = 0$, (d) $\nu = 4,\ j = 6 \rightarrow \nu' = 1,\ j' = 3$ transitions, for H+HD, using the potentials of Boothroyd *et al.* [38] (broken curve) and Mielke *et al.* [39] (full curve). The ENCO vibrational functions were employed in these calculations.

6.4.1 Summary of rate coefficients for H+HD

- Thermally averaged rate coefficients have been presented for rovibrationally inelastic transitions in H+HD.
- Rate coefficients calculated using the ENCO model were considerably larger than those obtained using the SHO model for low temperatures.
- The rate coefficients obtained using the ENCO were model were, typically, larger than those of the SHO model for all temperatures.
- The rate coefficients calculated for the potentials of Mielke *et al.* [39] and Boothroyd *et al.* [38] were in reasonable agreement. Some discrepancies were found at low temperatures.

Chapter 7

Applications

In this chapter several applications of the cross sections and rate coefficients are presented. The rate coefficients are most commonly used in astrophysical areas of study which are beyond the scope of this thesis. Hence, only a brief details of the astrophysical applications are given. This discussion in this chapter is more concerned with any significant changes produced as a result of using the newly calculated rate coefficients.

Results from this chapter have been presented in [54].

7.1 Vibrational relaxation rate coefficients

The vibrational relaxation rate, $k_{\nu\ \mathrm{rel.}}(\nu, j)$ is obtained by summing over collisional transition rates, $\langle\sigma v\rangle_{\nu j \to \nu' j'}$, to all levels (ν', j') with $\nu' < \nu$.

Allers *et al.* ([59], table 6) listed determinations of the vibrational relaxation rates, for H_2 , for the level $(\nu, j) = (1, 3)$ to all lower rotational levels of the $\nu = 0$, and similarly for $(\nu, j) = (2, 3)$ to $\nu = 0$ and $\nu = 1$, at $T = 1000$ K, along with their own estimates, based on observations of the Orion bar Photon-Dominated Region (PDR). Their tabulated values are reproduced in Table 7.1.

The calculations presented in this thesis, so far, have been for non–reactive scattering. Therefore, for comparison with the tabulated values presented in Allers *et al.* [59], an estimate of the reactive scattering rate was made using the prescription of Le Bourlot *et al.* [62]. In this method the non–reactive scattering rate, $\langle\sigma v\rangle^{\text{non-react.}}_{\nu j\to\nu' j'}$, is related to the reactive scattering rate, $\langle\sigma v\rangle^{\text{react.}}_{\nu j\to\nu' j'}$, using the following relations

$$\langle\sigma v\rangle^{\text{react.}}_{\nu j\to\nu' j'} = \langle\sigma v\rangle^{\text{non-react.}}_{\nu j\to\nu' j'} \times \exp\left(-\max\left\{0, \left[\frac{3900-(E_{\nu j}-E_{\nu' j'})}{T}\right]\right\}\right) \tag{7.1}$$

for when ($|j-j'|$ even),

$$\langle\sigma v\rangle^{\text{react.}}_{\nu j\to\nu' j'} = \frac{1}{2}\left[\langle\sigma v\rangle^{\text{non-react.}}_{\nu j\to\nu' j'-1} + \langle\sigma v\rangle^{\text{non-react.}}_{\nu j\to\nu' j'+1}\right]$$
$$\times \exp\left(-\max\left\{0, \left[\frac{3900-(E_{\nu j}-E_{\nu' j'})}{T}\right]\right\}\right) \tag{7.2}$$

for when ($|j-j'|$ odd and j even), and

$$\langle\sigma v\rangle^{\text{react.}}_{\nu j\to\nu' j'} = \frac{1}{6}\left[\langle\sigma v\rangle^{\text{non-react.}}_{\nu j\to\nu' j'-1} + \langle\sigma v\rangle^{\text{non-react.}}_{\nu j\to\nu' j'+1}\right]$$
$$\times \exp\left(-\max\left\{0, \left[\frac{3900-(E_{\nu j}-E_{\nu' j'})}{T}\right]\right\}\right) \tag{7.3}$$

for when ($|j-j'|$ odd and j odd). In the above relations $E_{\nu j}$ and T are given in units of kelvin.

The vibrational relaxation rate coefficients, determined from the rate coefficients in this thesis, are compared with those of Allers *et al.* [59] in Table 7.1. For the ENCO model, the estimated reactive scattering contribution was 54% of the total for $(\nu, j) = (1, 3)$ and 57% for $(\nu, j) = (2, 3)$ at $T = 1000$ K.

Flower and Roueff [18] have observed that the quasi–classical trajectory calculations of Garcia and Laganà [63], and Mandy and Martin [61] show that the reactive and non–reactive contributions to the rate coefficient for vibrational relaxation $\nu = 1 \to \nu = 0$ at $T = 300$ K of H_2 by H are related by $\langle\sigma v\rangle^{\text{react.}} \approx 2\langle\sigma v\rangle^{\text{non-react.}}$. This relationship, which probably relates to the larger number of final rotational states accessible in reactive scattering, where j may change by both even and odd integers, is consistent with the present estimate of the contribution of the reactive scattering channels to the total vibrational relaxation rate coefficient of H_2 . Nonetheless, the contribution of the reactive scattering channels remains a significant source of uncertainty, which can be removed only by quantum mechanical calculations that allow for proton exchange.

For the case of HD, the contribution of the reactive scattering may be expected to be smaller, by a factor of 2, as only one proton is available for exchange. For the work in this thesis[1], no correction has been applied for reactive scattering in H+HD.

The large variations in Table 7.1 are due to several factors:

- Differences in the calculation of $H+H_2$ interaction potential.
- Differences in the representation of the vibrational eigenfunctions (i.e. SHO, Morse, ENCO, 'exact oscillator' etc.).
- Differences in the treatment of the collision problem (i.e. Basis set size, quantum mechanical or semi-classical methods, etc.).

The results obtained in this thesis are in good agreement with the empirical estimates of Allers *et al.* [59]. There are large discrepancies with the earlier study of Le Bourlot *et al.* [62] which are largely due to the improved representation of the rovibrational eigenfunctions, rather than changes in the $H+H_2$ interaction potential, for which we have adopted the results of the calculations of Mielke *et al.* [39], whereas Le Bourlot *et al.* [62] used the potential calculated by Boothroyd *et al.* [38].

The agreement with Allers *et al.* [59] is encouraging. However, without the availability of accurate experimental data it is difficult to comment on the accuracy of the present work or that of Allers *et al.* [59]. There is little experimental data available for comparison with due mainly to the difficulty in performing such experiments.

7.2 Astrophysical models

It was shown, in Chapters 5 and 6, that there can be considerable differences in the magnitude of the rate coefficient depending on which vibrational representation is used, and in some cases on which interaction potential was

---

[1] Cooling by HD is significant for the application in Section 7.2.2 where pure rotational excitation in the $\nu = 0$ vibrational state at temperatures $T \lesssim 1000$ K, is dominant.

used. The magnitude of the differences was often dependent on the temperature given. However even with significant differences in the rate coefficients it does not follow automatically that the consequences in astrophysical simulations will be as significant. Even when the dominant excitation mechanism is collisions with H atoms, the populations of the rovibrational levels of H_2 depend on the relative importance of radiative (electric quadrupole) and collisional de-excitation. If the density is sufficiently high, collisional de-excitation dominates and the relative populations tend to a Boltzmann distribution. The values of the collisional rate coefficients are then irrelevant, except in so far as they determine the 'critical density', at which the Boltzmann distribution begins to be approached. At densities much less than the critical density, collisional excitation is followed by radiative decay, and so collisional excitation rates determine the line intensities. However, the spontaneous transition probabilities of H_2 are small, because electric dipole transitions are not allowed. Consequently, the critical density tends to be low, and regimes of even lower density may only have limited significance, in the context of the model.

For HD there is an electric dipole present, however the relative abundance ratio of HD to H_2 is typically $n_{\mathrm{HD}}/n_{\mathrm{H}_2} = 10^{-5}$.

The calculations of Le Bourlot *et al.* [62], which used the SHO model and the potential of Boothroyd *et al.* [38], have been used in previous astrophysical modelling. They were used as a benchmark for some of the present calculations, which used the 'exact oscillator' model with the potential of Mielke *et al.* [39], when used in astrophysical modelling. For the astrophysical examples presented in this thesis the rate coefficients were fit to the following function of temperature, T:

$$\langle \sigma v \rangle (T) = a + \frac{b}{t} + \frac{c}{t^2} \tag{7.4}$$

where $t = 10^{-3}T + \delta$ and $\delta = 1.0$ ensures the rate coefficients remain well behaved at low T.

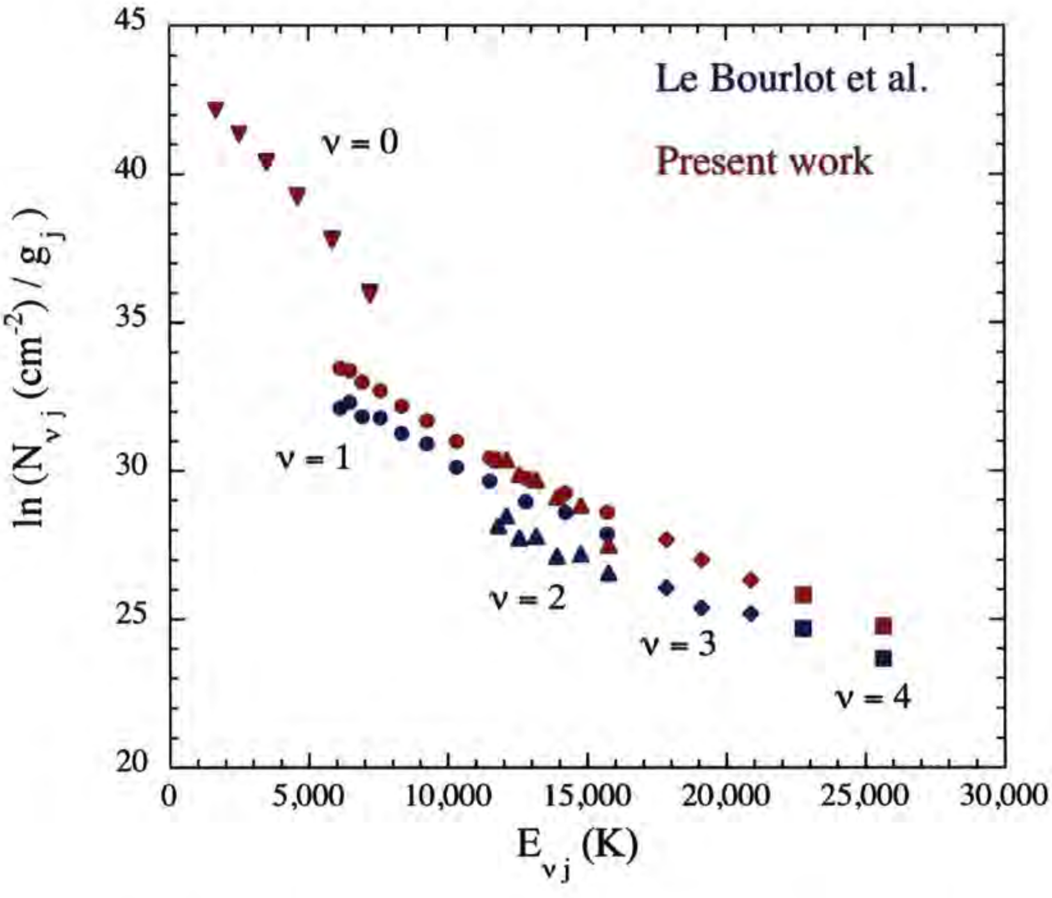

Figure 7.1: The excitation diagram computed for a C-type shock model, using the H+H_2 rate coefficients of Le Bourlot *et al.* [62] (in blue) and the present values (obtained using the 'exact oscillator' model and interaction potential of Mielke *et al.* [39]) (in red). Results are plotted for rotational levels in vibrational manifolds $0 \leq \nu \leq 4$. For $\nu = 0$, the blue and the red symbols overlap. The data for this figure was kindly provided by Antoine Gusdorf.

7.2.1 C–type shock waves in molecular clouds

In this application the H+H_2 rate coefficients are used. The rate coefficients for the rovibrational excitation of H_2 by H may be expected to play a significant role in C–type shock waves, propagating in a molecular gas [21]. Shock wave heating leads to partial dissociation of H_2 , enriching the gas in atomic H. Rotational and particularly rovibrational excitation of H_2 takes place, under conditions in which the excited vibrational levels are depopulated principally by spontaneous radiative decay to lower vibrational levels, rather than collisionally. Under these circumstances, the relative populations of the vibrational manifolds do not approach a Boltzmann distribution.

In Figure 7.1, the 'excitation diagram' of H_2 for a C–type shock model[2] is plotted with the following parameters: shock speed $v_s = 30$ km s^{-1}; pre–shock gas density $n_H = 10^4$ cm^{-3}; and pre–shock magnetic field strength, transverse to the direction of the (one–dimensional) flow, $B = 100$ μG. The initial chemical composition of the gas was calculated assuming that a steady state prevailed.

If the populations of the rovibrational levels conformed to a Boltzmann distribution at a given kinetic temperature, T, the data points in Figure 7.1 would fall on a single straight line, whose gradient is proportional to T^{-1}; in practice, this is not the case. However, within each vibrational manifold, the rotational levels fall approximately on straight lines corresponding to temperatures which tend to increase with the vibrational quantum number, ν. Differences are apparent, for $\nu > 0$, between the results obtained using the present H+H_2 rate coefficients and those of Le Bourlot *et al.* [62].

The results plotted in Figure 7.1 are readily understandable in the light of the previous discussion. For the populations of the levels of the $\nu = 0$ manifold, only the vibrationally elastic (and rotationally inelastic) rate coefficients are important, for which the 'old' and the 'new' values do not differ substantially at the temperatures relevant to the formation of the corresponding emission lines. On the other hand, for vibrationally excited levels, the new rate coefficients yield larger populations and column densities. Nonetheless, the changes are not as large as might have been anticipated from a glance

---

[2] The C–type shock models were run by Antoine Gusdorf.

at Table 7.1. The gas which is heated in the shock wave undergoes compression also, leading to an approximate thermalisation of the populations of the rotational levels within a given vibrational manifold. Furthermore, to the larger rates of rovibrational excitation corresponds a higher rate of cooling by H_2 . Because H_2 is a major coolant, the kinetic temperature falls, thereby reducing (exponentially) the rates of rovibrational excitation. In other words, there is a feedback loop which maintains the rate of cooling by H_2 at an approximately constant value.

7.2.2 Gravitational collapse of an inhomogeneity in the primordial gas

It is believed that the initial gravitational collapse of inhomogeneities in the primordial gas was made possible through radiative cooling by the trace amounts of molecular hydrogen which were produced in the post recombination era (Palla *et al.* [64]). The cooling by HD can be comparable to that by H_2 , owing to:

1. chemical fractionation, which enhances the deuterium content of molecular hydrogen.
2. the lower rotational constant of HD, which makes its rotational levels more energetically accessible.
3. the fact that HD has a permanent electric dipole moment, and hence transitions between adjacent rotational states can occur.

A model of gravitational collapse of a spherical condensation of the primordial gas was run[3], starting from the conditions of the primordial gas at a redshift $z \approx 40$ and attaining $z \approx 10$ asymptotically. A comparison of the thermal profiles obtained with the present and the previous values of the rate coefficients for the excitation of H_2 (Le Bourlot *et al.* [62]) and HD (Flower *et al.* [65]) by H is shown in Figure 7.2, through to a density $n_H \equiv n(H) + 2n(H_2) + n(HD) + n(H^+) = 10^{12}$ cm^{-3}.

---

[3] The gravitational collapse models were run by Professor David Flower.

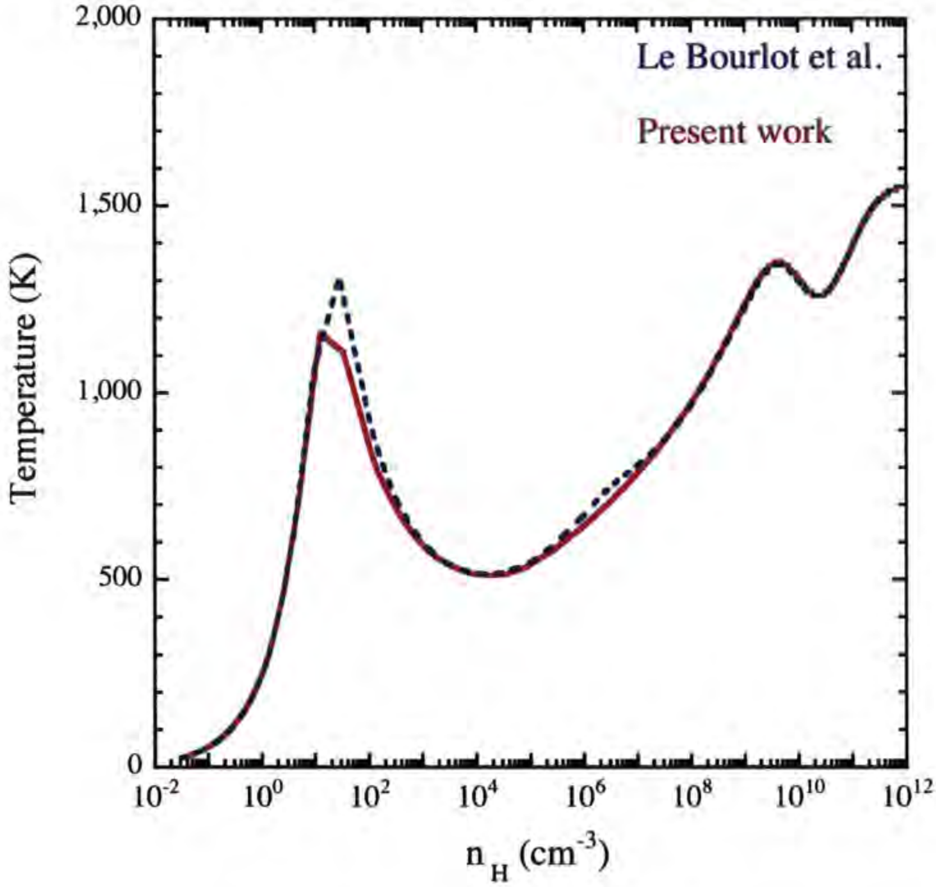

Figure 7.2: The temperature profile of a gravitationally collapsing spherical condensation of the primordial gas. The full curve was calculated with the present H+H_2 and H+HD rate coefficients (obtained using the 'exact oscillator' model and interaction potential of Mielke *et al.* [39]), the broken curve using the earlier data of Le Bourlot *et al.* [62] and Flower *et al.* [65]. The data for this figure was kindly provided by Professor David Flower.

In the initial phase of the collapse, the kinetic temperature, T, increases adiabatically: the density is so low that the rate of cooling by H_2 and HD is negligible. Approaching $n_H = 10$ cm^{-3}, collisional cooling assumes significance, and its rate increases quadratically with the density, n_H. As a consequence, T decreases, reaching a minimum for $n_H \approx 10^4$ cm^{-3}. The increases in the rate coefficients for rovibrationally inelastic scattering of H on both H_2 and HD (see Sections 5 and 6) lead to lower temperatures; but the progressive thermalisation of first the rotational levels and then, at higher densities, the vibrational levels (cf. Flower and Harris [66]) mitigates the effects on T. Furthermore, as the temperature does not exceed $T \approx 1000$ K over the range of density in Figure 7.2, the contribution of cooling due to vibrationally inelastic scattering is limited, as the $\nu = 1$ vibrational threshold is approximately 6000 K.

Reference	$k_{\nu\ \mathrm{rel.}}(\nu, j) = (1, 3)$	$k_{\nu\ \mathrm{rel.}}(\nu, j) = (2, 3)$
Sternberg and Dalgarno [60]	5.5(-10)	7.5(-10)
Mandy and Martin [61]	6.3(-12)	3.6(-11)
Le Bourlot *et al.* [62]	6.3(-13)	9.2(-13)
Allers *et al.* [59]	5.4(-11)	7.9(-11)
Present work: SHO, Mielke *et al.*	6.9(-13)	9.1(-13)
Present work: ENCO, Mielke *et al.*	1.6(-11)	1.5(-10)
Present work: 'Exact', Mielke *et al.*	2.1(-11)	1.4(-10)

Table 7.1: Values of the vibrational relaxation rates of the the specified upper rovibrational level, (ν, j), of H_2 , in units of cm^3 s^{-1}. The numerical values were evaluated for $T = 1000$ K by summing the the rate coefficients from the initial level, (ν, j), to all lower levels with $\nu' < \nu$. Numbers in parentheses are powers of 10.

Part IV

Conclusions and Future Work

Chapter 8

Concluding remarks

In this chapter the conclusions drawn from the scattering calculations and their application are summarised.

8.1 Scattering calculations

Cross sections, as a function of barycentric collision energy, and rate coefficients, as a function of kinetic temperature, were calculated for $H+H_2$ and H+HD using the quantum mechanical coupled–channels method. The calculations were performed for different vibrational representations of the molecule, and for the interaction potentials of Boothroyd *et al.* [38] and Mielke *et al.* [39]. The conclusions are summarised in the following subsections.

8.1.1 Convergence and basis set

The convergence of the cross sections with respect to the extent of the basis of rovibrational states was investigated carefully. Convergence was found to be slow, with couplings to states with vibrational quantum number $\nu = 6$ being significant for transitions between $\nu = 1$ and $\nu = 0$, for example. The slow convergence relates to the fact that H can undergo reactive scattering with H_2 and HD at collision energies exceeding a few thousand kelvin. The increase in the magnitudes of the potential coupling coefficients, $y_\lambda(\nu j, \nu' j' | R)$

($\nu \neq \nu'$), which control vibrationally inelastic scattering, with increasing ν, ν' (see figures 5.4 and 6.2, for example), reflects this fact.

8.1.2 Vibrating oscillator model

The SHO model of the vibrational motion was found to be unsatisfactory, particularly with regard to the predicted rate of increase from threshold of cross sections for vibrationally inelastic transitions. Cross sections obtained using the ENCO or 'exact oscillator' models were considerably larger in magnitude near threshold than those obtained using the SHO model. The cross sections calculated for the 'exact oscillator' and ENCO models contained significantly more structure than those of the SHO model.

The rate coefficients are determined directly from the cross sections. Thus discrepancies between the vibrational representations are expected in the rate coefficients too. Rate coefficients calculated using the 'exact oscillator' and ENCO models were considerably larger than those obtained using the SHO model, at low temperatures. The 'exact oscillator' and ENCO models tended to produce rate coefficients which were larger over the entire temperature range, than those obtained using the SHO model.

8.1.3 Interaction potentials

Overall, for $H+H_2$ and H+HD, there was reasonable agreement between cross sections calculated using the potential of Mielke *et al.* [39] and Boothroyd *et al.* [38] for most collision energies. Cross sections for some rovibrationally inelastic transitions in $H+ H_2$ exhibit significant differences in magnitude, notably in the near–threshold energy region, between the two interaction potentials.

The rate coefficients calculated for the potentials of Mielke *et al.* [39] and Boothroyd *et al.* [38] were in reasonable agreement. Some discrepancies were found at low temperatures.

8.2 Applications

8.2.1 Vibrational relaxation coefficient

The cross sections for rovibrational excitation of H_2 and HD are much larger near threshold when the numerically 'exact oscillator' eigenfunctions are employed compared with calculations based on the SHO approximation to the eigenfunctions. As a result, the rate coefficients for vibrational relaxation of the levels $(\nu, j) = (1, 3)$ and $(2, 3)$ are in much better agreement with estimates by Allers *et al.* [59], based on the observations of the Orion bar PDR.

8.2.2 Astrophysical models

The calculated rate coefficients, for the exact 'oscillator' representation, were incorporated into illustrative astrophysical models – of a C-type shock wave propagating in an interstellar molecular cloud and of the gravitational collapse of a condensation of the primordial gas. The conclusions may be summarised as follows:

1. There are significant consequences for the H_2 excitation diagram (Figure 7.1) predicted by an illustrative C–type shock model of speed $v_s = 30$ km s^{-1}, propagating into molecular gas of density $n_H = 10^4$ cm^{-3}; the new rate coefficients give rise to larger values of the column densities of the vibrationally excited levels. However, the increases in the column densities are much smaller than might be anticipated on the basis of a comparison of the new and the old rate coefficients, owing to the existence of a feedback loop, which maintains an approximately constant rate of cooling by H_2 .
2. In the model of the gravitational collapse of a condensation of the primordial gas, there is little modification of the thermal profile when the new rate coefficents are introduced. In this case, pure rotational excitation within the vibrational ground state, $\nu = 0$, is more important to the thermal balance than vibrational excitation, and the changes in

the rate coefficients for pure rotational excitation are less pronounced. Furthermore, the populations of rotational levels within a given vibrational manifold thermalize at lower gas densities, n_{H}, than do the relative populations of levels belonging to different vibrational states.

Chapter 9

Future work

It is believed that the scattering calculations presented in this thesis offer significant improvement over previous work performed on the H+H_2 and H+HD systems. However, there still remain several areas where the calculations could be modified to offer further improvement. In this chapter possible improvements to the scattering calculations and astrophysical applications are considered.

9.1 Scattering calculations

For each system considered, in this case H+H_2 and H+HD, there are several possible areas of improvement; such as the basis set size and the vibrational representation of the molecule. One area that is not open to immediate improvement is that of the interaction potential. The interaction potential of Mielke *et al.* [39] should be the most reliable, according to the precision quoted for the calculations, but future interaction potentials may offer even higher precision. In this case calculations would need to be repeated particularly for low collision energies. With an improved interaction potential, and the modifications suggested below, even higher accuracy cross sections and rate coefficients could be determined. Future experiments, and high–precision astrophysical observations, will allow further comparison between theoretical and experimental data which may enable further uncertainties in the calculation process to be reduced.

9.1.1 H+H_2

The H+H_2 scattering calculations were performed for a 54 level basis set using the SHO, ENCO, and ‘exact oscillator’ vibrational representations. The ‘exact oscillator’ model is the most accurate vibrational model to use, but it is also the most computationally demanding. The run–time, memory requirements, and input–file size grow rapidly as the basis set size increases. An increased basis set size offers higher accuracy in the convergence rate, and also opens higher (ν, j) transitions. The maximum number of rovibrational energy levels in the electronic ground state of para–H_2 and ortho–H_2 are 163 levels and 155 levels, respectively. Calculations with a complete basis set for H+para–H_2 and H+ortho–H_2 using the ‘exact oscillator’ are close to being feasible. This is the next stage for scattering calculations of this system and it is possible that it may be completed in the near future.

9.1.2 H+HD

The H+HD scattering calculations were performed for a 120 level basis set using the SHO and ENCO vibrational representations. Due to the large size of the basis set it was computationally impractical to perform calculations using the ‘exact oscillator’. The maximum number of rovibrational energy levels in the electronic ground state of HD is 399 levels. Therefore, to perform calculations using a full basis set is computationally impractical. There are two routes of progress for future work on H+HD. One way is to use the ‘exact oscillator’ model for as large a basis set as computationally feasible ($\sim$ 160 levels). The other way would be to increase the basis set size to as large as computationally feasible ($\sim$ 200 levels) using the ENCO model. It is possible that both routes may be investigated in the future.

9.2 Astrophysical applications

The implications of using the newly calculated rate coefficients, from this thesis, was investigated earlier in Chapter 7. If significant differences are found in future rate coefficient calculations then the astrophysical implications will have to be reinvestigated.

Regarding the newly calculated rate coefficients, the implications in other astrophysical areas will not be immediately apparent until further use is made of them by the astrophysical community. H and H_2 are the most abundant atomic and molecular species, respectively, in the universe and therefore the rate coefficients for $H+H_2$ and H+HD are required for calculations in a wide variety of astrophysical environments.

9.3 Reactive scattering

The calculations presented within this thesis have considered only non-reactive scattering in the $H+H_2$ and H+HD systems (i.e. where the reactive states have been neglected from the basis set). This is reasonable for low collision energies but for higher energies it is an unrealistic approximation.

It was found that the reactive scattering rate coefficients were a significant component of the total vibrational relaxation rate coefficients in Section 7.1. They were determined from approximations previously derived in [62] and therefore could provide only an estimate to the reactive scattering rate. Nevertheless, the contribution of the reactive scattering channels remains a significant source of uncertainty which can be removed only by quantum mechanical calculations which allow for proton exchange. Computer programs exist to solve this type of problem already, an example is ABC [67]. These programs could be modified to incorporate the interaction potential of Mielke *et al.* [39], and a large basis set, such that reactive scattering rates could be produced to complement the non-reactive rates presented within this thesis.

Part V

Appendices

Appendix A

Basis set used for para–H_2

Table A.1: The basis set used in the H+para–H_2 calculation.

Basis set no.	H_2 Level no.	ν	j	Energy (K)
1	1	0	0	0.0000
2	3	0	2	509.85
3	5	0	4	1681.6
4	7	0	6	3474.4
5	9	0	8	5829.7
6	10	1	0	5987.1
7	12	1	2	6471.6
8	15	1	4	7584.6
9	17	0	10	8677.3
10	18	1	6	9286.6
11	21	1	8	11521.8
12	22	2	0	11635.7
13	24	0	12	11940.3
14	25	2	2	12095.2
15	28	2	4	13150.7
16	31	1	10	14221.1
17	32	2	6	14764.1
18	33	0	14	15540.2

continued on next page

Table A.1: *continued*

Basis set no.	H_2 Level no.	ν	j	Energy (K)
19	36	2	8	16880.5
20	37	3	0	16952.8
21	39	1	12	17311.2
22	40	3	2	17387.7
23	44	3	4	18386.5
24	47	0	16	19403.4
25	48	2	10	19434.9
26	49	3	6	19912.2
27	50	1	14	20717.8
28	54	3	8	21911.7
29	55	4	0	21942.7
30	57	4	2	22353.2
31	58	2	12	22355.3
32	62	4	4	23295.6
33	63	0	18	23459.8
34	66	3	10	24322.6
35	67	1	16	24368.4
36	68	4	6	24734.0
37	70	2	14	25570.5
38	74	5	0	26606.7
39	75	4	8	26617.0
40	77	5	2	26992.8
41	78	3	12	27074.1
42	81	0	20	27644.5
43	83	5	4	27878.7
44	84	1	18	28194.8
45	87	4	10	28883.7
46	88	2	16	29009.3
47	89	5	6	29229.5
48	92	3	14	30097.8
49	96	6	0	30943.2

continued on next page

Table A.1: *continued*

Basis set no.	H_2 Level no.	ν	j	Energy (K)
50	97	5	8	30995.5
51	99	6	2	31304.6
52	100	4	12	31466.5
53	103	0	22	31900.3
54	105	6	4	32133.2

Appendix B

Basis set used for ortho–H_2

Table B.1: The basis set used in the H+ortho–H_2 calculation.

Basis set no.	H_2 Level no.	ν	j	Energy (K)
1	2	0	1	170.50
2	4	0	3	1015.2
3	6	0	5	2503.8
4	8	0	7	4586.3
5	11	1	1	6149.2
6	13	1	3	6951.5
7	14	0	9	7196.9
8	16	1	5	8365.2
9	19	0	11	10261.7
10	20	1	7	10341.5
11	23	2	1	11789.5
12	26	2	3	12550.5
13	27	1	9	12817.5
14	29	0	13	13703.1
15	30	2	5	13890.7
16	34	1	11	15722.2
17	35	2	7	15763.3
18	38	3	1	17098.3

continued on next page

Table B.1: *continued*

Basis set no.	H_2 Level no.	ν	j	Energy (K)
19	41	0	15	17443.9
20	42	3	3	17818.6
21	43	2	9	18107.4
22	45	1	13	18979.7
23	46	3	5	19086.4
24	51	2	11	20853.8
25	52	3	7	20856.5
26	53	0	17	21411.6
27	56	4	1	22080.0
28	59	1	15	22517.1
29	60	4	3	22759.8
30	61	3	9	23069.9
31	64	2	13	23930.7
32	65	4	5	23955.8
33	69	0	19	25539.6
34	71	4	7	25623.8
35	72	3	11	25659.8
36	73	1	17	26263.6
37	76	5	1	26735.9
38	79	2	15	27266.2
39	80	5	3	27375.2
40	82	4	9	27706.7
41	85	5	5	28498.9
42	86	3	13	28556.6
43	90	0	21	29766.6
44	91	5	7	30064.3
45	93	4	11	30139.9
46	94	1	19	30154.6
47	95	2	17	30792.3
48	98	6	1	31064.1
49	101	6	3	31662.3

continued on next page

Table B.1: *continued*

Basis set no.	H_2 Level no.	ν	j	Energy (K)
50	102	3	15	31690.2
51	104	5	9	32015.7
52	108	6	5	32712.7
53	109	4	13	32855.1
54	113	0	23	34037.5

Appendix C

Basis set used for HD

Table C.1: The basis set used in the H+HD calculation.

Basis set no.	HD Level no.	ν	j	Energy (K)
1	1	0	0	0.0000
2	2	0	1	128.38
3	3	0	2	384.24
4	4	0	3	765.86
5	5	0	4	1270.6
6	6	0	5	1895.2
7	7	0	6	2635.7
8	8	0	7	3487.4
9	9	0	8	4445.1
10	10	1	0	5226.5
11	11	1	1	5349.3
12	12	0	9	5503.2
13	13	1	2	5594.1
14	14	1	3	5959.2
15	15	1	4	6442.1
16	16	0	10	6656.0
17	17	1	5	7039.5
18	18	1	6	7747.5
19	19	0	11	7897.3

continued on next page

Table C.1: *continued*

Basis set no.	HD Level no.	ν	j	Energy (K)
20	20	1	7	8561.7
21	21	0	12	9220.7
22	22	1	8	9477.1
23	23	2	0	10197.7
24	24	2	1	10315.1
25	25	1	9	10488.3
26	26	2	2	10549.0
27	27	0	13	10620.0
28	28	2	3	10897.9
29	29	2	4	11359.2
30	30	1	10	11589.6
31	31	2	5	11929.9
32	32	0	14	12088.7
33	33	2	6	12606.2
34	34	1	11	12775.0
35	35	2	7	13383.7
36	36	0	15	13620.6
37	37	1	12	14038.5
38	38	2	8	14257.5
39	39	3	0	14918.7
40	40	3	1	15030.7
41	41	0	16	15209.4
42	42	2	9	15222.5
43	43	3	2	15254.0
44	44	1	13	15373.9
45	45	3	3	15586.9
46	46	3	4	16027.0
47	47	2	10	16273.2
48	48	3	5	16571.4
49	49	1	14	16775.2
50	50	0	17	16849.1

continued on next page

Table C.1: *continued*

Basis set no.	HD Level no.	ν	j	Energy (K)
51	51	3	6	17216.4
52	52	2	11	17403.8
53	53	3	7	17957.6
54	54	1	15	18236.0
55	55	0	18	18533.8
56	56	2	12	18608.3
57	57	3	8	18790.5
58	58	4	0	19392.7
59	59	4	1	19499.5
60	60	3	9	19709.9
61	61	4	2	19712.2
62	62	1	16	19750.6
63	63	2	13	19880.9
64	64	4	3	20029.2
65	65	0	19	20257.8
66	66	4	4	20448.4
67	67	3	10	20710.5
68	68	4	5	20966.8
69	69	2	14	21215.6
70	70	1	17	21312.9
71	71	4	6	21580.6
72	72	3	11	21786.7
73	73	0	20	22015.7
74	74	4	7	22286.0
75	75	2	15	22606.4
76	76	1	18	22917.3
77	77	3	12	22932.9
78	78	4	8	23078.2
79	79	5	0	23622.0
80	80	5	1	23723.5
81	81	0	21	23802.0

continued on next page

Table C.1: *continued*

Basis set no.	HD Level no.	ν	j	Energy (K)
82	82	5	2	23925.6
83	83	4	9	23952.3
84	84	2	16	24047.5
85	85	3	13	24143.1
86	86	5	3	24226.9
87	87	1	19	24558.2
88	88	5	4	24625.1
89	89	4	10	24903.2
90	90	5	5	25117.4
91	91	3	14	25411.7
92	92	2	17	25533.2
93	93	0	22	25611.9
94	94	5	6	25700.3
95	95	4	11	25925.4
96	96	1	20	26230.4
97	97	5	7	26369.7
98	98	3	15	26732.8
99	99	4	12	27013.3
100	100	2	18	27057.9
101	101	5	8	27121.2
102	102	0	23	27440.6
103	103	6	0	27606.9
104	104	6	1	27703.0
105	105	6	2	27894.5
106	106	1	21	27928.6
107	107	5	9	27950.1
108	108	3	16	28100.8
109	109	4	13	28161.3
110	110	6	3	28180.0
111	111	6	4	28557.2
112	112	2	19	28616.2

continued on next page

Table C.1: *continued*

Basis set no.	HD Level no.	ν	j	Energy (K)
113	113	5	10	28851.1
114	114	6	5	29023.3
115	115	0	24	29283.4
116	116	4	14	29363.7
117	117	3	17	29510.0
118	118	6	6	29574.9
119	119	1	22	29647.9
120	120	5	11	29819.1

Bibliography

[1] Ed. G.W.F. Drake 2006 *Atomic, Molecular & Optical Physics Handbook* (Springer-Verlag)

[2] Murrell J N and Bosanac S D 1989 *Introduction to the Theory of Atomic and Molecular Collisions* (John Wiley & Sons)

[3] Tielens A G G M 2005 *The Physics and Chemistry of the Interstellar Medium* (Cambridge: Cambridge University Press)

[4] Lequeux J 2005 *The Interstellar Medium* (Springer)

[5] Carruthers G R 1971 *ApJ* **166** 349

[6] Spitzer L, Drake J F, Jenkins E B, Morton D C, Rogerson J B and York D G 1973 *ApJ* **181** L116

[7] Shull J M, Tumlinson J, Jenkins E B *et al.* 2000 *ApJ* **538** L73

[8] The *Infrared Space Observatory* (ISO) special issue 1996 *A&AS* **315**(2)

[9] Stancil P C, Lepp S and Dalgarno A 1998 *ApJ* **509** 1

[10] Allison A C and Dalgarno A 1967 *Proc. Phys. Soc. London* **90** 609

[11] Eastes W and Secrest D 1972 *J. Chem. Phys.* **56** 640

[12] Green S and Truhlar D G 1979 *ApJ* **231** L101

[13] Sun Y and Dalgarno A 1994 *ApJ* **427** 1053

[14] Flower D R and Wroe R A 1996 *J. Phys. B: At. Mol. Opt. Phys.* **29** L851

[15] Flower D R 1997 *J. Phys. B: At. Mol. Opt. Phys.* **30** 3009

[16] Forrey R C, Balakrishnan N, Dalgarno A and Lepp S 1997 *ApJ* **489** 1000

[17] Flower D R 1997 *MNRAS* **288** 627

[18] Flower D R and Roueff E 1998 *J. Phys. B: At. Mol. Opt. Phys.* **31** L955

[19] Roueff E and Flower D R 1999 *MNRAS* **305** 353

[20] Roueff E and Flower D R 1999 *MNRAS* **309** 833

[21] Flower D R 2007 *Molecular Collisions in the Interstellar Medium, Second Edition* (Cambridge: Cambridge University Press)

[22] Child M S 1974 *Molecular Collision Theory* (Academic Press)

[23] Arthurs A M and Dalgarno A 1960 *Proc. Roy. Soc. London* **A256** 540

[24] Percival I C and Seaton M J 1957 *Proc. Cambridge Phil. Soc.* **53** 654

[25] Pack R T 1974 *J. Chem. Phys.* **60**, 633

[26] Abramowitz M and Stegun I A 1965 *Handbook of Mathematical Functions* (Dover Publications, New York)

[27] Rose M E 1957 *Elementary Theory of Angular Momentum* (John Wiley & Sons, New York)

[28] Brink D M and Satchler G R 1968 *Angular Momentum* (Clarendon Press, Oxford)

[29] Edmonds A R 1960 *Angular Momentum in Quantum Mechanics* (Princeton University Press, Princeton N.J.)

[30] Messiah A 1969 *Quantum Mechanics, vol. 2* (North Holland Publishing, Amsterdam)

[31] Launay J -M 1976 *J. Phys. B: Atomic & Molecular Physics* **9**, 1823

[32] Danby G 1983 *J. Phys. B: Atomic & Molecular Physics* **16**, 3393

[33] Lester A J 1971 *Methods in Computational Physics* **10** 211

[34] Kaplan I G 2006 *Intermolecular Interactions: Physical Picture, Computational Methods and Model Potentials* (John Wiley & Sons)

[35] Liu B 1973 *J. Chem. Phys.* **58** 1925

[36] Varandas A J C, Brown F B, Mead C A, Truhlar D G, 1987 *J. Chem. Phys.* **86** 6258

[37] Boothroyd A I, Keogh W K, Martin P G and Peterson M R 1991 *J. Chem. Phys.* **95** 4343

[38] Boothroyd A I, Keogh W K, Martin P G and Peterson M R 1996 *J. Chem. Phys.* **104** 7139

[39] Mielke S L, Garrett B C and Peterson K A 2002 *J. Chem. Phys.* **116** 4142

[40] Lepp S, Buch V and Dalgarno A 1995 ApJS **98** 345

[41] Schiff L I 1968 *Quantum Mechanics* (McGraw–Hill Book Company, Singapore)

[42] Flügge S 1974 *Practical Quantum Mechanics* (Springer–Verlag)

[43] Le Roy R J 2007 *LEVEL 8.0: A Computer Program for Solving the Radial Schrödinger Equation for Bound and Quasibound Levels* University of Waterloo Chemical Physics Research Report CP-663; see http://leroy.uwaterloo.ca/programs/

[44] Marston C C and Balint-Kurti G G 1989 *J. Chem. Phys.* **91** 3571

[45] Press W H, Teukolsky S A, Vetterling W T and Flannery B P 1992 *Numerical Recipes in FORTRAN, Second Edition* (Cambridge University Press)

[46] Flower D R, Bourhis G and Launay J-M 2000 *Computer Physics Communications* **131** 187

[47] Hutson J M and Green S 1994 *Collaborative Computational Project 6* Daresbury Laboratory : UK Science and Engineering Research Council

[48] Manolopoulos D E and Alexander M H 1992 *J. Chem. Phys.* **97**, 2527

[49] Launay J -M 1977 *J. Phys. B: Atomic & Molecular Physics* **10**, 3665

[50] Johnson B R 1973 *J. Comput. Phys.* **13** 445

[51] de Vogelaere R 1955 *J. Res. Nat. Bur. Stand.* **54** 119

[52] Wrathmall S A and Flower D R 2006 *J. Phys. B: At. Mol. Opt. Phys.* **39** L249

[53] Wrathmall S A and Flower D R 2007 *J. Phys. B: At. Mol. Opt. Phys.* **40** 3221

[54] Wrathmall S A, Gusdorf A and Flower D R 2007 *MNRAS* Accepted for publication.

[55] Dabrowski I 1984 *Can. J. Phys.* **62** 1639

[56] Chao S D, Harich S A, Dai D X, Wang C C, Yang X and Skodje R T 2002 *J. Chem. Phys.* **117** 8341

[57] Dabrowski I and Herzberg G 1976 *Can. J. Phys.* **54** 525

[58] Abgrall H, Roueff E and Viala Y 1982 *A&AS*, **50** 505

[59] Allers K N, Jaffe D T, Lacy J H, Draine B T and Richter M J 2005 *ApJ* **630** 368

[60] Sternberg A and Dalgarno A 1989 *ApJ* **338** 197

[61] Mandy M E and Martin P G 1993 *ApJS* **86** 199

[62] Le Bourlot J, Pineau des Forêts G and Flower D R 1999 *MNRAS* **305** 802

[63] Garcia E and Laganà A 1986 *Chem. Phys. Lett.* **123** 365

[64] Palla F, Salpeter E E and Stahler S W 1983 *ApJ* **271** 632

[65] Flower D R, Le Bourlot J, Pineau des Forêts G and Roueff E 2000 *MNRAS* **314** 753

[66] Flower D R and Harris G J 2007 *MNRAS* **377** 705

[67] Skouteris D, Castillo J F and Manolopoulos D E 2000 *Computer Physics Communications* **133** 128